Structural and Magnetization Studies on Selected Multiferroic Oxides

By

PRALAY PAUL

PHYS01201604026

Technical Physics Division
Bhabha Atomic Research Centre, Mumbai - 400085

A thesis submitted to the

Board of Studies in Physical Sciences

In partial fulfillment of requirements
for the Degree of

DOCTOR OF PHILOSOPHY
of
HOMI BHABHA NATIONAL INSTITUTE

January, 2021

Homi Bhabha National Institute

Evaluation Report of Ph.D. Viva-Voce
Board of Studies in Physical Sciences

A. General Details

1. **Name of the Constituent Institution: BHABHA ATOMIC RESEARCH CENTRE, MUMBAI**

2. **Name of the Student:** **PRALAY PAUL**
3. **Enrolment Number:** **PHYS01201604026**
4. **Date of Enrolment in HBNI:** **JANUARY 01, 2016**
5. **Date of Submission of Thesis:** **JANUARY 27, 2021**
6. **Title of the Thesis:** **Structural and Magnetization Studies on Selected Multiferroic Oxides**

7. **Number of Doctoral Committee Meetings held with respective dates:**

Review Period	Date	Review Period	Date
1. 2017 - 2018	November 13, 2018	2. 2018 - 2019	December 12, 2019
3. 2019 - 2020	November 01, 2020		

8. **Name and Affiliation of the Examiner 1: Prof. Dilip Pal, Professor, Department of Physics, Indian Institute of Technology, Guwahati, India**

   Recommendations of the Examiner 1 (Thesis Evaluation) (i) accepted, (ii) accepted after revisions, or (iii) rejected: Accepted

9. **Name and Affiliation of the Examiner 2: Prof. Kartik Ghosh, Distinguished Professor, Physics, Astronomy and Materials Science Department, Missouri State University, Springfield, USA**

   Recommendations of the Examiner 2 (Thesis Evaluation) (i) accepted, (ii) accepted after revisions, or (iii) rejected: Accepted

B. Recommendations of the Viva-Voce Board

1. **Date of Viva Voce Examination:** **May 15, 2021 (Online mode, through Google Meet)**
2. **Name and affiliation of external examiner: Prof. Dilip Pal, Professor, Department of Physics, Indian Institute of Technology, Guwahati, India**
3. **Whether there were other experts / faculty / students present? Please, enclose a soft copy of attendance sheet indicating participation in person / over video as per proforma given below at (5)**
4. **Recommendations for the award of the Ph.D. degree: Recommended / ~~Not Recommended~~**

This thesis investigates structural, magnetic, and magneto-electronic properties of some important multiferroic oxides viz. $GdFeO_3$, $YMnO_3$, and $BiFeO_3$ and the influence of substitution at their cationic sites. A small ferromagnetic moment observed in $GdFeO_3$ was corroborated by a computational study using the VASP package. In $YMnO_3$, Ga substitution was shown to stabilize Mn valence and a correlation between magnetization and XPS results has been established. Also, Gd and La co-substitution in $BiFeO_3$ results in the reduction of leakage current and magneto-electric coupling at room temperature. The work described in the thesis is of high standard and several of its results have been published in peer reviewed international journals Therefore, we recommend this thesis for the award of a Ph.D. degree in Physics of HBNI.

5. **Names & Signatures of Viva Voce Board members (Doctoral Committee & External Examiner):**

Sr No	Composition	Name	Signature with date
1.	**Chairman**	**Prof. Amitabh Das**	18.5.21
2.	**Convener** (Guide)	**Prof. T. V. Chandrasekhar Rao**	15/5/21
3.	**External Examiner**	**Prof. Dilip Pal**	Dilip Pal 15/5/21
4.	**Member**	**Prof. (Ms.) D. Bhattacharya**	15.5.21
5.	**Member**	**Prof. A. K. Debnath**	21.05.2021
6.	**Member (External)**	**Prof. K. G. Suresh**	15.5.21

Others present during the viva-voce through online.

7.	**Dr. Dinesh V. Udupa, BARC, HBNI**	8.	**Dr. A. K. Rajarajan, BARC**	9.	**Dr. C. L. Prajapat, BARC**
10.	**Dr. A. Dwivedi, BARC**	11.	**Mrs. Deeksha Gupta, HBNI**	12.	**Ms. Amrita Datta, SINP**
13.	**Mr. Dipankar Pal, BARC**	14.	**Ms. Madhu Ghanathe, HBNI**	15.	**Mr. Rahul Kaiwart, BARC**
16.	**Mr. Raman Gandhi, BARC**	17.	**Mr. K. Sandeep Rao, BARC**	18.	**Mr. Sourabh Wajhal, BARC**
19.	**Dr. Ahmad Basha, Ex-HBNI**				

21/5/2021

Dean-Academic, CI

डॉ. दिनेश वी. उडुपा / Dinesh V. Udupa
डीन-शैक्षणिक / Dean - Academic
भौतिक एवं गणितीय विज्ञान / Physical & Mathematical Science
होमी भाभा राष्ट्रीय संस्थान / Homi Bhabha National Institute
अणुशक्ती नगर / Anushakti Nagar
मुंबई / Mumbai - 400 094.

(Convener, Viva-Voce Board)

Structural and Magnetization Studies on Selected Multiferroic Oxides

By

PRALAY PAUL

PHYS01201604026

Technical Physics Division
Bhabha Atomic Research Centre, Mumbai - 400085

A thesis submitted to the

Board of Studies in Physical Sciences

In partial fulfillment of requirements
for the Degree of

DOCTOR OF PHILOSOPHY
of
HOMI BHABHA NATIONAL INSTITUTE

January, 2021

STATEMENT BY AUTHOR

This dissertation has been submitted in partial fulfillment of requirements for an advanced degree at Homi Bhabha National Institute (HBNI) and is deposited in the Library to be made available to borrowers under the rules of HBNI.

Brief quotations from this dissertation are allowable without special permission, provided that accurate acknowledgement of source is made. Requests for permission for extended quotation from or reproduction of this manuscript in whole or in part may be granted by the Competent Authority of HBNI when in his or her judgment the proposed use of the material is in the interests of scholarship. In all other instances, however, permission must be obtained from the author.

Pralay Paul

(PRALAY PAUL)

Name & Signature of the student

DECLARATION

I, hereby declare that the investigations presented in the thesis have been carried out by me. The work is original and has not been submitted earlier as a whole or in part for a degree / diploma at this or any other Institution / University.

Pralay Paul

(PRALAY PAUL)

Name & Signature of the student

List of Publications arising from the thesis

Journal

---

1. “Valence fluctuation and magnetic frustration in Ga substituted $YMnO_3$”, **Pralay Paul**, A.K. Rajarajan, A.K. Debnath, Rekha Rao and T.V. Chandrasekhar Rao, J. Magn. Magn. Mater. 503 (2020) 166617 (1 – 6).

2. "Ground State Spin Structure of $GdFeO_3$: A Computational and Experimental study", **Pralay Paul**, P.S. Ghosh, A.K. Rajarajan, P. D. Babu and T.V. Chandrasekhar Rao, J. Magn. Magn. Mater. 518 (2021) 167407 (1 - 7).

Conferences

---

1. “Structural and magnetic properties of $YMn_{1-x}Ga_xO_3$”, **Pralay Paul**, A.K. Rajarajan, C. L. Prajapat, A.K. Debnath and T.V. Chandrasekhar Rao, AIP Conference Proceedings 2265 (2020) 030505 (1 - 4).

2. “Low temperature magnetic properties of $GdFeO_3$”, **Pralay Paul**, C. L. Prajapat, A. K. Rajarajan, and T. V. Chandrasekhar Rao, AIP Conference Proceedings, 1942 (2018) 130029 (1 - 3).

3. “Theoretical and experimental study of multiferroic $BiFeO_3$”, **Pralay Paul**, Tuhin Kumar Maji, Krishna Kanhaiya Tiwari, Balaji Mandal, A. K. Rajarajan, Ranu Bhatt, Debjani Karmakar, and T. V. C. Rao, AIP Conference Proceedings, 1832 (2017) 130058 (1 - 3).

Others

---

1. “Magnetic and transport properties of inverse Heusler compound Cr_2CoAl” Amrita Datta, Mantu Modak, **Pralay Paul**, Manju Mishra Patidar, T. V. Chandrasekhar Rao, V Ganesan, Sangam Banerjee, J. Magn. Magn. Mater. 521 (2021) 167522 (1 - 8).

Communicated

1. "Plausible Multiferroic and Magneto-electric Behaviour of Polycrystalline $Bi_{0.85}Gd_{0.05}La_{0.1}FeO_3$ at Room Temperature", **Pralay Paul**, A.K. Rajarajan, S. Kuila, A.K. Debnath, B.P Mandal and T.V. Chandrasekhar Rao. (under review).

1. “Metamagnetic Transition in polycrystalline $GdFeO_3$”, **Pralay Paul**, A. K. Rajarajan, P. D. Babau and T. V. Chandrasekhar Rao. (under review).

Presentation in national and international conferences

1. **Pralay Paul**, et al., Theoretical and Experimental study of Multiferroic BiFeO3, 61st DAE – Solid State Physics Symposium, 26th – 30th December 2016, KIIT University, Bhubaneswar, Odisha, India.

2. **Pralay Paul,** et al., Low Temperature Magnetic Properties of GdFeO3, 62ndDAE – Solid State Physics Symposium, 26th – 30th December 2017, DAE Convention Centre, Anushaktinagar, Mumbai, India.

3. **Pralay Paul,** et al., Plausible Room Temperature Ferromagnetism in Bi0.9-xGdxLa0.1FeO3, International Conference on Magnetic Materials and Applications (ICMAGMA - 2018), 9th – 13th December, 2018, NISER-Bhubaneswar, Jatni, Odisha, India.

4. **Pralay Paul,** et al., On Magnetic Transition in GdFeO3, Materials and Technologies for Energy Conversion and Storage (M-TECS - 2018), 26th Sept. – 29th Sept. 2018, Bhabha Atomic Research Centre, Mumbai, India.

5. Pralay Paul, et al., Effect of Ga Doping on Magnetic Properties of h-YMnO3, 63rd DAE – Solid State Physics Symposium, 18th – 22nd December 2018, Guru Jambheshwar University of Science and Technology (GJUS&T), Hisar, Haryana, India.

6. **Pralay Paul,** et al., Structural and Magnetic Properties of YMn1-x GaxO3, 64th DAE – Solid State Physics Symposium, 18th – 22nd December 2019, Indian Institute of Technology Jodhpur, Jodhpur, Rajasthan, India.

7. **Pralay Paul,** et al., A study on valence fluctuation in Ga substituted YMnO3, The International Magnetics Conference (INTERMAG 2020), 4th – 8th May, 2020, Montreal, Canada (Paper was accepted for oral presentation but conference got cancelled on account of COVID-19).

Pralay Paul
(PRALAY PAUL)
Name & Signature of the student

Dedicated to my family and teachers

ACKNOWLEDGEMENT

First and foremost, I express my sincere respect and gratitude to my Ph.D. supervisor Prof. T. V. Chandrasekhar Rao for his guidance, continuous support and encouragement. Perhaps, it would have become very tough to complete my Ph.D. thesis without his valuable suggestions and guidance. He always looks after me as his own child. His morality and kindness inspired me in each moment to grow up in a different way. Thank you, Sir.

I am thankful to all the members of my doctoral committee, Prof. Amitabh Das, Prof. A. K. Debnath, Prof. (Ms.) D. Bhattacharya and Prof. K. G. Suresh for their periodic evaluation of my Ph.D. work, invaluable suggestions and discussions. My sincere thanks to Prof. A. K. Rajarajan for teaching me a lot and helping me to grow up as an independent research scholar. His expert guidance and invaluable suggestions always motivated me to take up new challenges throughout the course of my Ph.D. program.

A special thanks to Dr. C. L. Prajapat for his prompt support during the course of my studies. Also, I would like to thank Dr. B. C. Maji, Mr. Buddhadev Karnar and Pallavi Mam for XRD measurements. I am grateful to all members of the TPD office for their cooperation in paperwork related to my Ph.D. program. Also, I thank all members of BARC who have helped directly/indirectly for this thesis work.

I acknowledge BARC, Department of Atomic Energy, India, for financial support for living in Mumbai and attending national/international conferences during the Ph.D. program.

I am grateful to Mr. Anurup Das for several discussions. Also, I would like to thank my friends at BARC, Dipankar Paul, Rajashree Ramachandran, Rahul Kaiwart, Raman Gandhi, Sukanya De, Vishal Sharma, Pallavi Priyadarshani, Swathi Gandhi, Kruti Halankar, Sandeep K Rao, Madhu Ghanate, M. A. Basha, Perela Ramaswamy, Tapas Das, Chandrakant Golap,

Shitaljit Sharma, Utpal Dutta, and all others for their moral supports. Also, I would like to thank all members of the cricket team of the Chemistry Division, BARC.

Finally, but most importantly, I am extremely grateful to my family members for their constant love and mental supports. More than anyone, I am grateful to my parents without whom I would not have existed.

CONTENTS

Chapter 3: Density Functional Theory Based Computational Study on $GdFeO_3$ Using Vienna Ab-initio Simulation Package (VASP) (41 – 70)

Chapter 4: Structural and Magnetization Studies on Polycrystalline $GdFeO_3$ (71 – 88)

Chapter 5: Study of Magnetic Frustration in Polycrystalline $Y(Mn,Ga)O_3$ (89 – 108)

List of Tables

List of Figures

Figure 7.1 Powder X-ray diffraction pattern of polycrystalline $BiFeO_3$ and $Bi_{0.9-x}Gd_xLa_{0.1}FeO_3$ (x = 0.0, 0.05) recorded at room temperature (λ = 1.5406 Å). Peak indexing is associated with orthorhombic-structure of *R3c* space group.

Figure 7.2 Rietveld-refinement of XRD patterns of polycrystalline $BiFeO_3$ and $Bi_{0.9-x}Gd_xLa_{0.1}FeO_3$ (x = 0.00 and 0.05) compounds recorded at ambient temperature. The arrows indicate (006) and (018) peaks. A visualization of FeO_6 octahedron obtained from refined data is also presented.

Figure 7.3 Schematic view of unit-cell of $BiFeO_3$ drawn using experimental crystallographic information file extracted from Rietveld-refinement.

Figure 7.4 X-ray photoelectron spectroscopy survey spectrum of polycrystalline $Bi_{0.85}Gd_{0.05}La_{0.1}FeO_3$ recorded at room temperature. Insets show the O 1s spectra of $BiFeO_3$ and $Bi_{0.85}Gd_{0.05}La_{0.1}FeO_3$.

Figure 7.5 ZFC and FC magnetization as a function of temperature, M(T) of polycrystalline $BiFeO_3$ measured under a dc field of 100 Oe.

Figure 7.6 ZFC and FC magnetization as a function of temperature, M(T), of polycrystalline $Bi_{0.9}La_{0.1}FeO_3$ measured under dc fields of 100 Oe and 1000 Oe.

Figure 7.7 ZFC and FC magnetization as a function of temperature, M(T), of polycrystalline $Bi_{0.85}Gd_{0.05}La0_{.1}FeO_3$ measured under dc fields of 100 Oe and 500 Oe.

Figure 7.8 Field dependent magnetization M(H) curves of polycrystalline $BiFeO_3$ and $Bi_{0.9-x}Gd_xLa_{0.1}FeO_3$ (x = 0.00 and 0.05) measured at room temperature. Inset shows the magnetified view near zero field.

Chapter 1

Introduction

Oxide materials that contain two or more different cations are termed as complex oxide materials and they stabilize in different crystal structures. One of the most important and widely studied structure is the perovskite structure with chemical formula ABO_3, where ‘A’ and ‘B’ are two different cations belonging to rear earth and transition metal family respectively, with different ionic radii, oxidation states, coordination numbers etc. Because of these diversities, ABO_3 structure shows various interesting properties including ferromagnetism [1 – 3], ferroelectricity [4 – 6], superconductivity, insulating properties [9, 10] etc., which allow them to become suitable for technological applications such as sensors [11, 12], integrated circuits [13, 14], data storage [15, 16] etc. Additionally, the materials that combine various functional properties in a single phase, making them suitable for emergent technology like spintronics, are driving much attention in recent times.

These complex oxides are characterized by four different ferroic order parameters associated with magnetism, electricity, elasticity and toroidicity. The material that exhibits more than one ferroic order parameter is known as a multiferroic material. The multiferroic materials which show simultaneous existence of magnetic and electric ordering became centres of intense activity in solid-state material research. Spontaneous magnetization and polarization in such multiferroic compounds can be used in many emergent technologies. Further, certain class of materials, called magneto-electric (ME) materials, show a coupling between their magnetic and electric properties, i.e. spontaneous magnetization (non-zero magnetic moment in the absence of magnetic field as shown in figure 1.1) can be manipulated by an external electric field and spontaneous polarization (non-zero electric dipole moment in the absence of electric field as shown in figure 1.1) can be controlled by an external magnetic field. This coupling between ferromagnetic and ferroelectric orders provides an extra degree of freedom which can be used to develop new devices with ME materials because the electric field not only induces polarization but also can alter the magnetization and vice-versa.

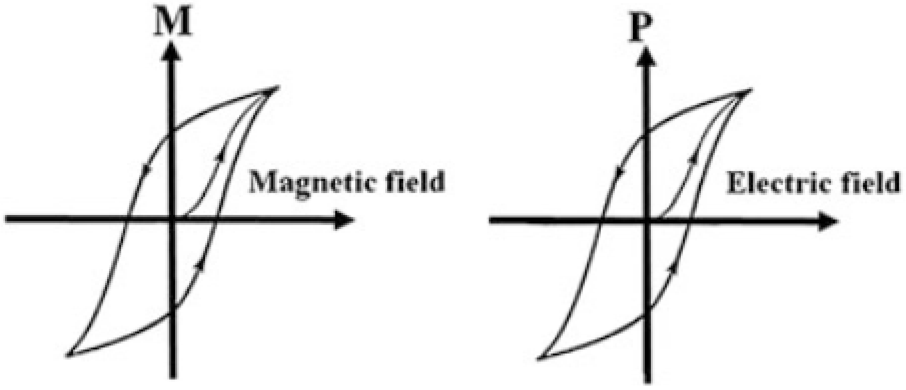

Figure 1.1: Characteristic magnetic and electric hysteresis loops associated with typical ferromagnetic and ferroelectric materials.

1.1 A Historical Background of Multiferroic Materials

It was believed that the origin of magnetic and electric properties is different and can't co-exist in a single-phase material, although Maxwell's electromagnetic equations provided the linkage between electricity and magnetism long time ago. It was Pierre Curie who first proposed in 19th century that ferromagnetism (FM) and ferro-electricity (FE) can co-exist in a single phase. After that, a detailed discussion on possibility of ME coupling was published by Landau and Lifshitzin an edition in 1959 [17]. In 1960, the situation changed when I. E. Dzyaloshinskii concluded based on symmetry analysis that Cr_2O_3 should have linear magneto-electric behaviour [18] and it was verified experimentally by D. Astrov [19] in the next year. Woefully, Cr_2O_3 could not meet to technological application due to paraelectric properties underlying anti-ferromagnetism, although a coupling between electric and magnetic properties has been demonstrated in this compound [20, 21]. Over the next decades, scientists in Europe, predominantly the group of Smolenskii in St. Petersburg (then Leningrad)

[22, 23] and Venevtsev in Moscow [24], tried to combine FM and FE properties in single phase materials. Finally, the investigation on multiferroic materials got a boost in 1994 after a successful observation of FM and FE properties along with ME coupling by H. Schmid in single phase boracites materials [25].

Unfortunately, these materials showed a weak ME coupling at very low temperatures which made technological applications impractical. So, the curiosity of finding a strong ME coupling in multiferroic materials and efforts to unravel rich physics behind these interesting phenomena remained undeterred. Soon after that, several multiferroic materials like $YMnO_3$, $TbMnO_3$, $LuFe_2O_3$ etc. were found [26 - 33] but none of them could lead to practical applications. The renaissance of multiferroic materials took place with the discovery of $BiFeO_3$ pioneered by Smolenskii and Chupis [34]. Although it shows a high polarization and ME coupling above room temperature, it could not give rise to practical application because of its high conductivity due to oxygen vacancies, Fe mixed valency and underlying anti-ferromagnetic (AFM) properties [35, 36]. It took a long time to understand the microscopic origin of ferroelectricity and anti-ferromagnetism in $BiFeO_3$ compound, and also the genesis of a large leakage current. Thus, from the beginning of twentieth century, there is a huge progress in the synthesis and characterization of high transition temperature multiferroic materials with ABO_3 chemical formula due to efforts by many research groups. Among such materials, rare earth based ferrites and manganites such as $BiFeO_3$ [35], $GdFeO_3$ [37], $DyFeO_3$ [10], $YMnO_3$ [38] etc. show multiferroic properties over a wide range of temperature. Many review articles have been written on synthesis of recently developed multiferroic materials, their multiferroic properties, the physics behind ME coupling and the limitations in their utility for practical applications [39 – 41].

1.2 Microscopic Origin of Ferroelectricity and Ferromagnetism

As multiferroic materials exhibit more than two order parameters simultaneously, limiting our discussion to ferroelectricity and ferromagnetism in ABO_3 (A = Rare earth element, B = Transition element) type perovskite structure, it is important to understand the origin of these ferroic properties. In general, the magnetism in ABO_3 perovskite structure is associated with the unpaired electrons present in *d* or *f* orbitals of 'A' and/or 'B' cations. The exchange interaction between these electrons leads to different kinds of magnetic orderings in these compounds. However, in case of ferroelectricity, the situation is entirely different. A displacement of body centred ion from centrosymmetric position in perovskite structure results in spontaneous polarization [42, 43]. In general, the dipole interaction between 'B' cation and the oxygen ion located in the direction of ionic shift of 'B' cation is strong enough to overcome the repulsive interaction between the cations, which gives rise to spontaneous polarization [44, 45]. Hence, ferroelectricity favours an asymmetrically distorted crystal structure, whereas magnetism favours a symmetric or centrosymmetric structure. Thus, the mechanisms associated with ferroelectricity and magnetism are mutually exclusive and consequently very few materials show both phenomena (see figure 1.2) [46].

It follows that for the coexistence of ferroelectricity and magnetism in single phase, the ion that moves off from centrosymmetric position, leading to spontaneous polarization, should be different from the one that gives rise to magnetization. In general, in perovskite ABO_3 structure, multiferroism is achieved by using 'A' cation as the source of ferroelectricity and 'B' cation as the source of magnetism. Another way it could be achieved is by looking for alternative mechanisms of ferroelectricity and magnetism. For example, the interaction between Ti^{4+} and oxygen ions plays an important role for ferroelectricity in $BaTiO_3$, whereas lone pair electrons on Pb and Bi in $PbTiO_3$ and $BiFeO_3$ become important for the same [47 - 49]. Hence, the exploration of multiferroic materials with different kinds of magnetism remains an open area of future research.

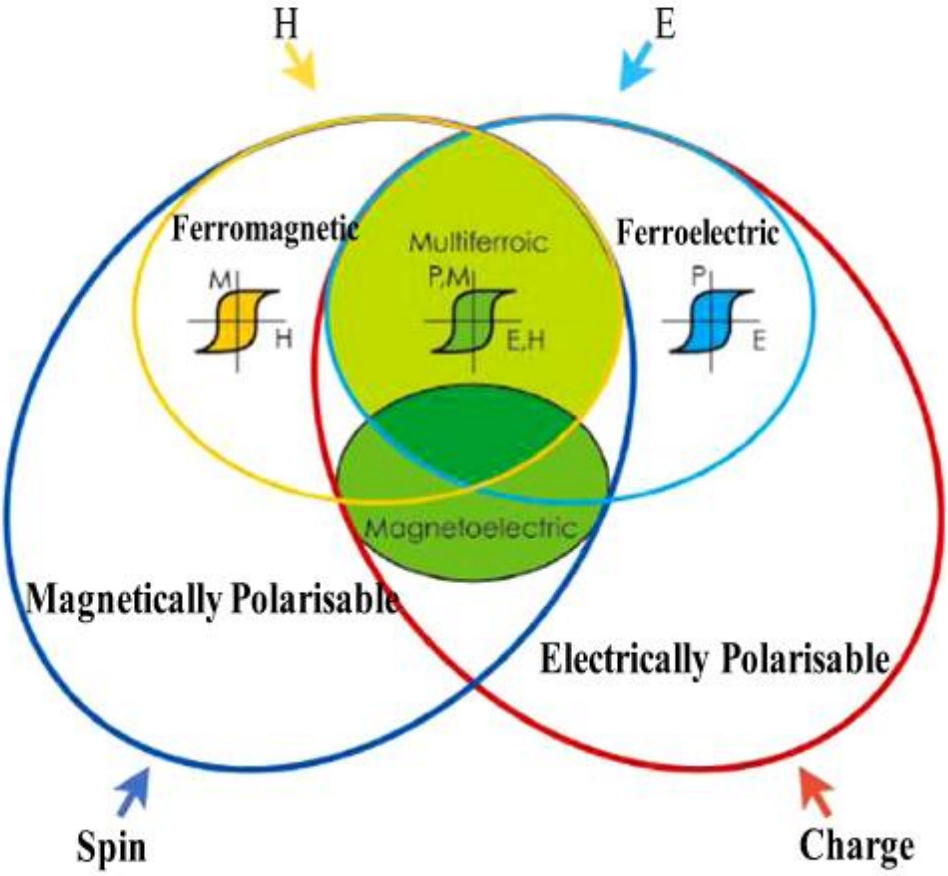

Figure 1.2: Illustration shows materials belonging to various categories e.g. ferromagnetic, ferroelectric, multiferroic and magnetoelectric.

Based on the origin of ferroelectricity and magnetism, the multiferroic materials can be categorized in two classes. The first is type-I, in which ferroelectricity and magnetism have different origins and are independent of each other, but show some level of ME coupling. In general, this class of materials show ferroelectric properties with a large polarization (~ 10 $\mu C.cm^{-2}$ – 100 $\mu C.cm^{-2}$) at sufficiently high temperature (> 800 K), well above magnetic ordering temperature. Second one is type-II multiferroic materials in which spontaneous polarization appears due to magnetic ordering, suggesting the presence of a strong magnetoelectric coupling. However, these compounds show significantly less polarization (~ 10^{-2} $\mu C.cm^{-2}$), that too far below ambient temperature [50, 51].

1.3 Single Phase Multiferroic Materials

From the beginning of nineties (of last century), a significant advancement was observed in the field of multiferroic materials in terms of synthesis of new complex oxide materials which show multiferroic properties at high temperatures [52 - 54]. The hard efforts lead to the finding of new materials including Bi-based ferrites and manganites such as $BiFeO_3$, $BiMnO_3$ etc. Besides, several attempts were made by substituting at Bi and/or Fe/Mn sites with other rear earth and/or transition elements to enhance multiferroic properties. On the other hand, there are several rare-earth based perovskite multiferroic oxides which are under investigation. Here, we introduce different classes of single phase multiferroic materials and discuss their ferroelectric and magnetization studies.

- **Rare -Earth (RE) Manganite ($REMnO_3$) Multiferroics**

Most of the single phase multiferroic materials show ferroelectric properties at a sufficiently high temperature (~ 900 K) and (anti)ferromagnetic properties at quite a low temperature (below 100 K). Because of this large difference between two ordering temperatures, they show a weak magnetoelectric coupling. Rare-earth manganites have a general chemical formula $REMnO_3$ where RE represents rare-earth elements such as Tb, Yb, Y, Bi, La etc. The electronic configuration of Mn^{3+} in these compounds is $t_{2g}^3 e_g^1$ and depending on the nearest neighbour (NN) and next-nearest neighbour (NNN) interaction, these compounds show many novel properties [55]. Besides, depending upon the ionic radii of RE elements, the crystal structure of $REMnO_3$ compounds stabilizes in two different forms: 'hexagonal' in case of larger ionic radius of the rare-earth element involved (La, Pr, Nd, Gd, Tb, Dy etc.), and 'orthorhombic' for smaller ionic radius (Ho, Yb, Lu, Y). The electronic structure and magnetic properties of these compounds have been studied extensively [56 – 60]. These compounds show interesting properties due to Jahn-Teller distortion which is quite dominant in rare-earth manganites. Based on the magnitude of this distortion which in turn changes with the ionic radius of the rare-earth element involved [61], these compounds show magnetic transitions associated with Mn^{3+} moments at different temperatures. For example, the Mn^{3+} moments order antiferromagnetically below ~ 40 K in $HoMnO_3$ [62], whereas transition temperature increases to ~ 141 K for $TbMnO_3$ [63]. The magnetic transition associated with rare-earth ion occurs at lower temperatures [64, 65]. The magnetic structures associated with Mn^{3+} ions in $LaMnO_3$, $NdMnO_3$ and $PrMnO_3$ are similar, called 'C-type' antiferromagnetic configuration (in Bertaut's notation) with a ferromagnetic component in 'a – c' plane and anti-ferromagnetic coupling along 'b' axis, as confirmed from neutron diffraction studies [58, 66 - 68]. However, a sinusoidal magnetic structure of Mn^{3+} ions is reported for $TbMnO_3$ [57, 69].

Most of the compounds in $REMnO_3$ family show ferroelectricity which is not connected to magnetic structure of magnetic ions involved. It has been shown using DFT based computational study in $REMnO_3$ that although the magnetic ion possesses Jahn-Teller active *d* orbitals, its displacement from centrosymmetric position is not favoured [70]. Ferroelectricity in these compounds is connected with rare-earth ions. In some cases, such as $BiMnO_3$, the existence of stereo-chemically active lone pair of $6s^2$ electrons on Bi atom leads to off-center displacement of rare-earth atoms, resulting in spontaneous polarization [71]. In case of $YMnO_3$, the Mn^{3+} ions are arranged in trimeric geometry forming MnO_5 polyhedrons connected to each other by a corner sharing oxygen atoms. This trimer of Mn ions is connected to the unequal distribution of Y atoms which induce spontaneous polarization [72]. The coupling between ferroelectricity and magnetism in $YMnO_3$ originates from the interaction between ferroelectric and magnetic domain walls [73]. A similar phenomenon is observed in isostructural $HoMnO_3$ compound [74]. However, a spiral modulated spin structure of Mn^{3+} ions results in ferroelectric and ferromagnetic behaviour in $TbMnO_3$ [75].

Also, a successful control of polarization by external magnetic field is demonstrated in $TbMnO_3$.

- **Rare -Earth (RE) Ferrite ($REFeO_3$) Multiferroics**

Rare-earth orthoferrites, $REFeO_3$ (RE denotes rear earth elements) attracted a great attention due to their novel magnetic properties. Most of the compounds belonging to this category show a weak ferromagnetism due to Dzyaloshinsky–Moriya (anti-symmetric exchange) interaction [76, 77]. Various interesting properties such as magnetic phase transition (antiferromagnetic transition of Fe (T_{N1})), spin reorientation (T_{SR}), compensation effect (T_{comp}), ordering of RE (T_{N2}) and weak ferromagnetism (canted anti-ferromagnetism) as well as the ferroelectricity in these compounds mainly originate from the competing exchange interaction between RE–RE, Fe–Fe, and RE–Fe [78]. For example, $LaFeO_3$ exhibits an antiferromagnetic transition at ~ 740 K [79], which is the highest in orthoferrite family. In addition, the exchange interaction between AFM and FM layers of Fe^{3+} ions results in a large exchange bias in this compound [80]. Perovskite $GdFeO_3$ exhibits ferromagnetic and ferroelectric ground state. The exchange interaction between Gd and Fe sub-lattices results in multiple magnetic phase transitions along with the appearance of spontaneous polarization below the ordering temperature associated with Gd^{3+} sub-lattice [37]. A mutual controllability of magnetic and electric properties in this compound is also successfully demonstrated. A ferroelectric hysteresis loop is observed in single crystal $DyFeO_3$. The origin of ferroelectricity is explained in terms of exchange striction effect between antiferromagnetic Dy component and spin polarized Fe component [10]. A recent study shows that weak ferromagnetism plays a crucial role in inducing ferroelectricity in this compound [81]. However, in case of $SmFeO_3$, the observation of ferroelectricity at sufficiently higher temperature (below ~ 670 K) is surprising and its origin is still not clearly understood [82, 83]. However, a large structural distortion is observed in case of smaller RE ions which changes the spin exchange interaction strength and results in modified magnetic properties. For example, $YbFeO_3$ shows a ferroelastic ferroelectric property due to Yb $5d_z{}^2$–O $2p_z$ orbital hybridization [84]. In case of $NdFeO_3$, although competitive interactions of Nd and Fe sub-lattices give rise to multiple magnetic phase transitions, the ferroelectric property is missing [85]. The ferroelectric loop observed in $TbMnO_3$ is connected to the structural distortion [86]. Perovskite $BiFeO_3$ is the most potential multiferroic material which shows a largest polarization (~ 100 $\mu C.cm^{-2}$) among all multiferroic materials [87 – 89]. It shows antiferromagnetic and ferroelectric transitions, respectively, below T_N ~ 643 K [88] and T_C ~ 1100 K [89]. The presence of $6s^2$ lone pair of electrons on Bi^{3+} is responsible for the appearance of spontaneous polarization in this compound. The magnetic structure of $BiFeO_3$ consists of helical arrangement of Fe^{3+} moments in antiferromagnetic fashion which results in null magnetization in bulk form [90, 36]. The annulment of magnetization inhabits the first order magnetoelectric coupling in this material. Besides, the large leakage current and complexity in formation of pure phase hinders $BiFeO_3$'s utility for practical application [91, 92].

- **Rare -Earth (RE) Orthochromite ($REFeO_3$) Multiferroics**

Rare-earth orthochromites is yet another class of single phase multiferroic materials belonging to ABO_3 family. The tilting of CrO_6 octahedron plays an important role in the physical properties of $RECrO_3$ compounds, similar to the role of FeO_6 octahedra in $REFeO_3$. The appearance of spontaneous polarization is assumed to be directly connected to magnetic ordering of Cr^{3+} moments and weak ferromagnetism originates from the antisymmetric exchange interaction (DM interaction) between Cr^{3+} - Cr^{3+} moments in these compounds [93]. However, the ferroelectric properties of $RECrO_3$ have not been explored much. Very few candidates in this group which show simultaneous existence of electric and magnetic ordering have been investigated. The appearance of spontaneous polarization in this compound originates from the off-centre displacement of Cr^{3+} ions [94 – 96]. The spin arrangement of Cr^{3+} is G-type antiferromagnetic configuration in $GdCrO_3$, and no ferroelectric property is observed [97]. In case of $ErCrO_3$, an antiferromagnetic ordering with a weak ferromagnetic moment is observed below T_N ~ 135 K [98] due to competitive interaction between Er and Cr magnetic sub-lattices. In case of $YCrO_3$, an AFM ordering below ~ 160 K and FE behaviour below ~ 450 K is observed [99].

1.4 Magnetization Studies on some Single Phase Multiferroic Materials

It is clear from previous discussion that the appearance of spontaneous polarization is connected, somehow or the other, to magnetism in most of the multiferroic materials in ABO_3 family. In this section, we provide detailed magnetization studies of some selected multiferroic materials. Before that, we briefly discuss the fundamentals of magnetism.

● Fundamentals of Magnetism

Magnetization in matter originates from the motion of electrons and nuclei. However, the magnetic moment associated with nuclear motion is thousand times smaller to that associated with electrons and hence, the macroscopic magnetization is due to electronic contribution only. There are two kinds of electronic motion, one is linked to precession of electrons in different orbitals around the nucleus which gives rise to orbital magnetic moment. Another is linked to spinning of the electron around themselves which gives rise to spin magnetic moment. The elementary magnetic moment associated with first orbital motion and the spinning of electron are the same and magnetic moment is expressed using a special symbol μ_B, called *Bohr magneton*, defined as,

$$\mu_B = {}^{eh}/_{4\pi m_e} \qquad (1.1)$$

where e, h, and m_e are the electronic change, Planck's constant and mass of free electron respectively. μ_B is considered as an elementary unit in magnetism. Due to magnetic moment, materials respond to an external magnetic field (H) through internal magnetization (M). The ratio of M to H is called susceptibility (χ), one of the characteristic parameters of a magnetic material. Depending up the sign and magnitude of χ, which in turn depends on the collective behaviour of electrons, the materials can be distinguished as Diamagnetic (DM), Paramagnetic (PM), Ferromagnetic (FM) or Antiferromagnetic (AFM). In case of DM and PM materials, there are no collective magnetic interactions between electrons and hence they do not show any magnetic ordering. However, FM and AFM materials are characterized by magnetic order of electron spins below certain temperature called magnetic transition temperature. The variation of inverse susceptibility against temperature for all types of material is presented in figure 1.3. In general, diamagnetism appears in all materials. It tends to oppose the externally applied magnetic field and hence is repelled by magnetic field. Temperature independence of susceptibility with a negative χ is an important characteristic feature of DM materials. These materials do not have any unpaired electrons.

In case of paramagnetic materials, the presence of unpaired electrons is the origin of magnetization, although there are no mutual interactions between these electrons. In the presence of an external magnetic field, the unpaired electrons show a tendency to orient along the field direction, resulting in net positive magnetization. Temperature dependent magnetization follows Curie-Weiss law in these materials. The χ value varies in the range of 10^{-5} to 10^{-2} with a positive coefficient for a typical paramagnetic material. Like paramagnetic materials, ferromagnetic materials consist of unpaired electrons. Due to the presence of mutual interaction, these unpaired electrons not only show the tendency to orient along the field direction, but also get oriented parallel to each other below some characteristic temperature.

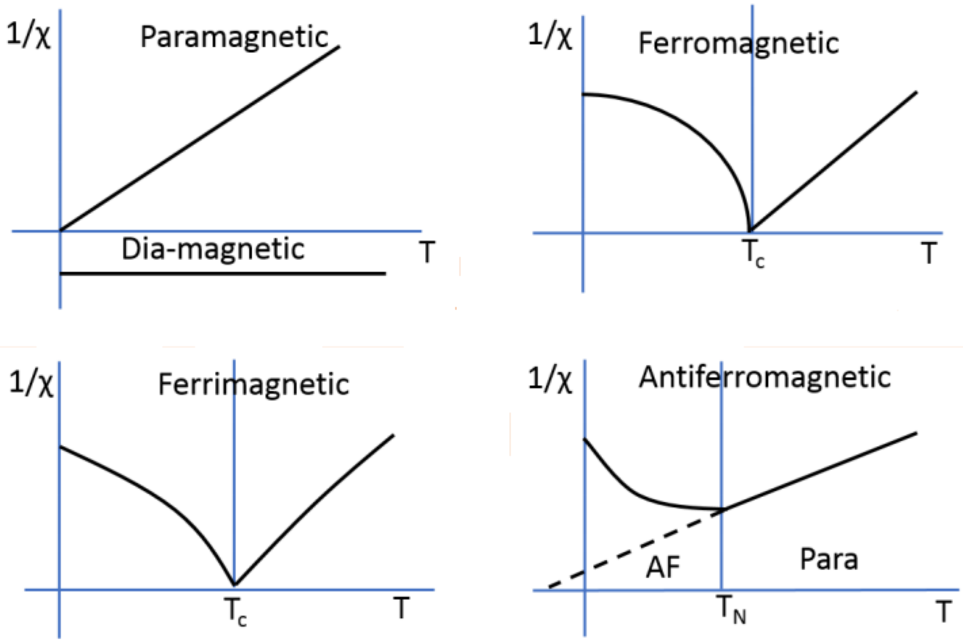

Figure 1.3: Schematic drawing of inverse susceptibility as a function temperature for Paramagnetic, Diamagnetic, Ferromagnetic, Ferrimagnetic and Antiferromagnetic materials.

Every ferromagnetic substance has its characteristic temperature called Curie temperature (T_C) above which it loses its ferromagnetic nature. The mutual interaction between electrons can be expressed by Heisenberg interaction [100] as follows,

$$H = -2J\vec{S}_i.\vec{S}_j \qquad (1.2)$$

where $\vec{S}_i$ and $\vec{S}_j$ are, the spins associated with i^{th} and j^{th} electrons. The parameter J is the exchange interaction constant which is positive and negative for parallel alignment (FM) and antiparallel alignment (AFM) respectively of adjacent spins. A large χ value ($\sim 10^3$) is observed for FM materials. In AFM materials, due to negative exchange interaction, the neighbouring electrons orient antiparallel to each other which cancels out net magnetization. So, AFM materials show a very small χ value.

- **$TbMnO_3$**

The room temperature crystal structure of $TbMnO_3$ is a distorted orthorhombic structure with ‘Pbnm’ space group symmetry [see figure 1.4]. The magnetic structure associated with Mn ions possess a sinusoidal anti-ferromagnetic arrangement below $T_N \sim 42$ K with a wave vector of q = (0, k_s, 1) [50, 55, 101]. In addition to that, it shows two magnetic anomalies at ~ 7 K and ~ 27 K associated with Tb^{3+} - Tb^{3+} and Tb^{3+} - Mn^{3+} interactions as shown in Figure 1.4 [50]. It is concluded from X-ray diffraction studies that the modulated AFM spin arrangement in $TbMnO_3$ is induced by magneto-elastic effect of lattice deformation [102]. However, this modulated spin structure locks in below ~ 27 K [50]. An anomaly in dielectric constant is observed at ~ 27 K which is connected to magnetic structure. It also shows a spontaneous polarization below ~ 27 K which is switchable by external electric as well as magnetic fields [50], as shown in figure 1.4. The origin of ferroelectricty in this compound is the shifting of Mn^{3+} ions from their centrosymmetric position due to crystallographic deformations which is induced by magnetic ordering. This compound belongs to type-II multiferroic category. Although, its spontaneous polarization is very low (8.0×10^{-4} $C.m^{-2}$) compared to well know ferroelectric $BaTiO_3$, it is comparable to that observed in improper ferroelectrics [103]. As the lattice modulation in $TbMnO_3$ is accompanied by a magnetic ordering, it shows a strong magnetoelectric coupling. It is therefore concluded that magnetic order drives spontaneous polarization along with magnetoelectric coupling in this compound. However, these phenomena occur at low temperatures, thus limiting their practical utility.

- **$DyFeO_3$**

Perovskite $DyFeO_3$ is another potentials candidate in multiferroic family which belong to type-II category. The crystal structure of this compound is orthorhombic with ‘Pnma’ space group [104]. It consists of two different magnetic sub-lattices associated with Dy and Fe.

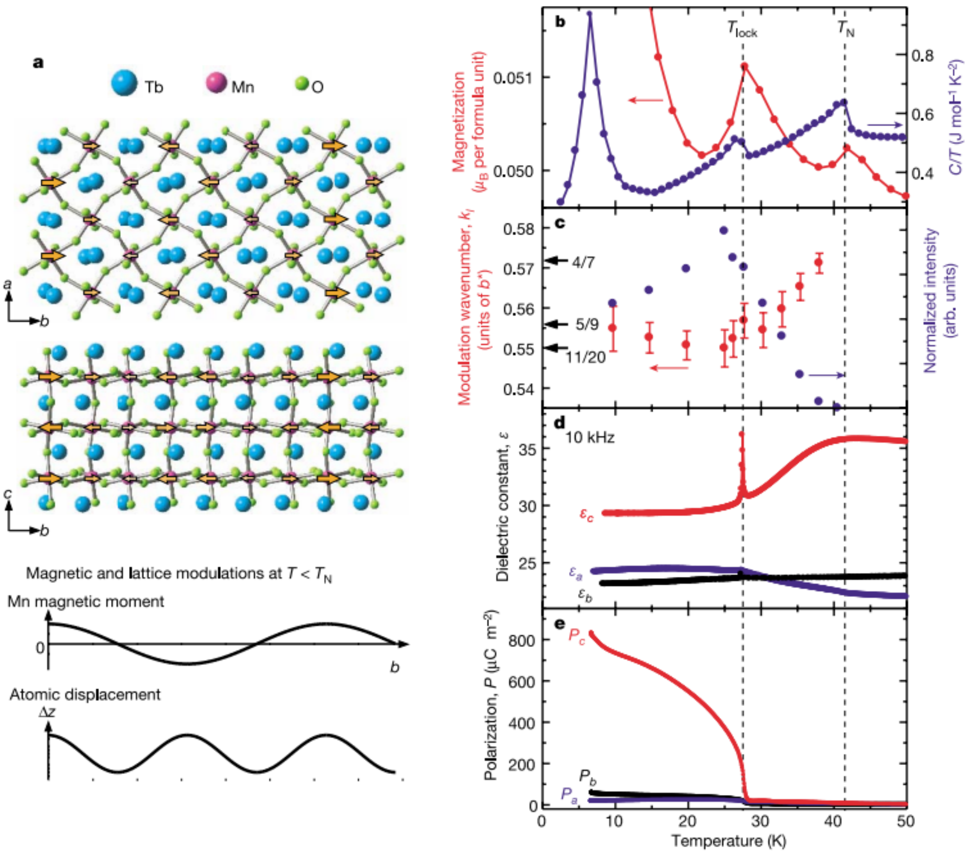

Figure 1.4: (a) Room temperature crystal structure of $TbMnO_3$. Lower part represents spatial variation of Mn moments along ‘b’ axis and displacement (Δz) of Mn ions along ‘c’ axis below their antiferromagnetic transition temperature, (b) Magnetization (M) and specific heat (C) as a function of temperature (T), (c) The modulation wave vector and normalized intensity as a function of temperature obtained from neutron diffraction studies and (d & e) The dielectric constant measured at 10 kHz and polarization, plotted against temperature.

Based on the strength of exchange interaction between Dy – Dy, Dy – Fe and Fe – Fe, it shows three magnetic transitions. An AFM ordering associated with Fe^{3+} ions is observed below T_{N1} ~ 645 K [10], with the magnetic structure (G_x, A_y, F_z) in Betraut’s notation and a weak ferromagnetic (WFM) component along ‘b’ and ‘c’ axes due to DM interaction [10]. With lowering temperature, the compound shows another magnetic transition below ~ 37 K related to spin reorientation of Fe^{3+} moments to (F_x, C_y, G_z) configuration [105] due to Dy^{3+} – Fe^{3+} interaction, along with vanishing of WFM component. However, with application of external field $H > H^{Fe}_{r}$, the spin structure of Fe^{3+} changes to (G_x, A_y, F_z) with the appearance of WFM component. On further cooling, it shows another AFM transition below T_{N2} ~ 4 K which is associated with Dy^{3+} sub-lattice [10]. A large polarization along ‘c’ axis appears below Dy^{3+} ordering temperature, above which polarization vanishes, suggesting that the ordered moment of Dy^{3+} plays crucial role in the observation of spontaneous polarization. A polarization value of ~ 0.15 $\mu C.cm^{-2}$ is observed which is reasonably large for spin driven ferroelectricity and also comparable to those reported in other manganites [106, 107]. A successful change of polarity of polarization with poling electric field is observed in this compound as demonstrated in figure 1.5(b). Also, the temperature at which spontaneous polarization appears decreases with decreasing applied magnetic field suggesting a magneto-electric coupling. It shows a linear magneto-electric (ME) coupling coefficient ~ 2.4×10^{-2} CGS unit which is larger than that observed for well-known ME material Cr_2O_3 [10].

- **$BiMnO_3$**

$BiMnO_3$ is probably a potential multiferroic candidate of the rare-earth manganite family. It undergoes multiple structural phase transitions with decreasing temperature. At temperatures above ~ 770 K, its crystal structure is described by non-polar ‘Pbnm’ space group and it stabilizes in polar monoclinic structure with ‘C2’ space group below that temperature [108]. This origin of ferroelectricity in this compound is due to displacement of Bi ions from centrosymmetric position on account of hybridization between $6s^2$ lone-pair electrons on Bi and oxygen ions [109]. A magnetic transition to ferromagnetic state is observed below T ~ 100 K [108] (see figure 1.6). The ferromagnetic state in this compound is assumed to be connected to the e_g orbital ordering of Mn^{3+} ions. An anomaly in specific heat against temperature is also observed, concomitant with the magnetic transition, as shown in figure 1.6. Also, a significant change in magneto-capacitance is observed in magnetic field dependent-dielectric measurements [108].

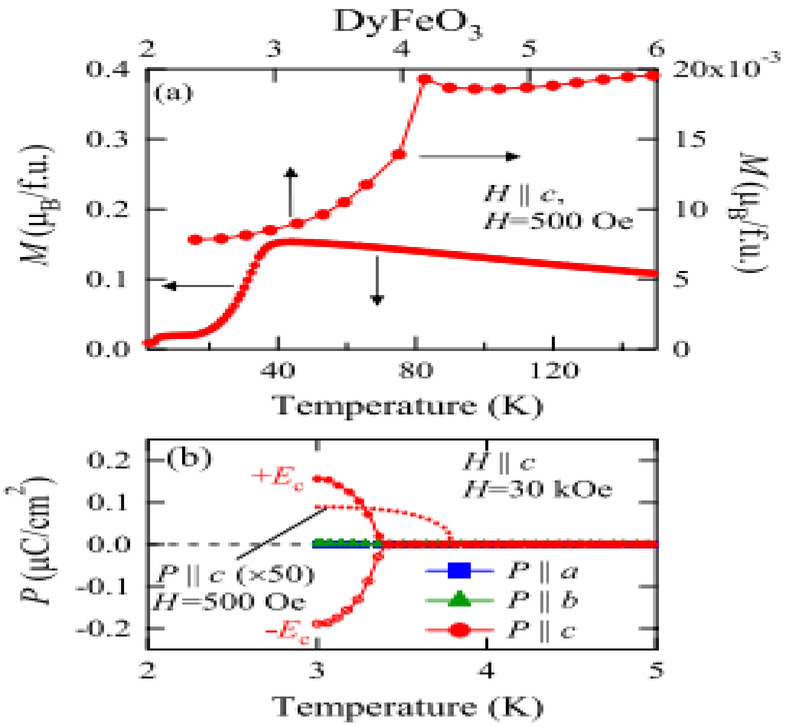

Figure 1.5: (a) Magnetization versus temperature measured with field applied parallel to c-axis for single crystal $DyFeO_3$ in the temperature range 2.4 K – 6.0 K (upper abscissae) and 2.4 K – 140.0 K (lower abscissae). (b) Polarization as a function of temperature along a, b, and c axes under H = 30 kOe applied parallel to c-axis (solid filled lines). Positive and negative polarization corresponds to poling with positive and negative electric field respectively. Dotted line shows polarization (magnified by a factor of 50) against temperature for an applied field of 500 Oe.

A detailed analysis reveals that the large magneto-capacitance behaviour is due to the coupling between polarization and magnetic ordering. Isothermal polarization measurements on polycrystalline $BiMnO_3$ show ferroelectric behaviour over a wide temperature range of 80 K - 400 K [110]. However, a good ferroelectric loop is obtained only below ~ 100 K. Ferroelectricity in this compound originates due to the presence of stereo chemically active $6s^2$ lone pair electrons on Bi^{3+} ions. As the origins of ferromagnetism and ferroelectricity are different, this compound belongs to type-II multiferroic family. Observation of anomaly in specific heat and dielectric measurements below magnetic ordering (~ 100 K), along with a good ferroelectric behaviour in the magnetic ordered state,

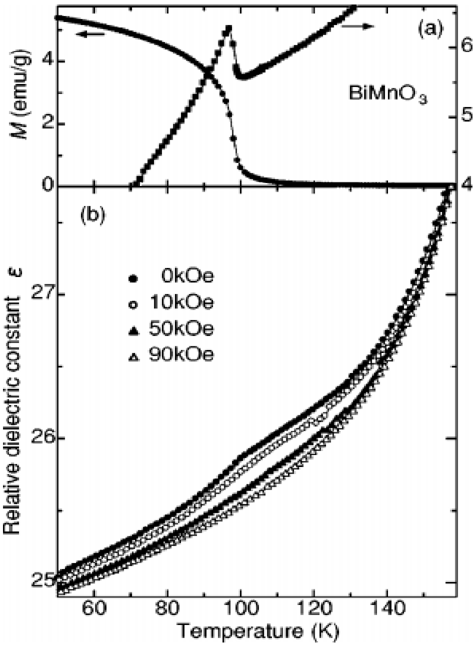

Figure 1.6: (a) Magnetization and specific heat as a function of temperature for $BiMnO_3$ single crystal. (b) Relative dielectric constant against temperature for the same compound.

confirm that $BiMnO_3$ is a good multiferroic magneto-electric material. The above discussion clearly shows that magnetic properties impact other electronic properties directly.

1.5 Motivation and Scope of the Work

To be suitable for technological applications, single-phase multiferroic materials should possesses strong magneto-electric coupling, along with high polarization and magnetization values, with an operating temperature above the ambient. As an example of application of magneto-electric multiferroic materials in Random Access Memory (RAM), one would like to combine ultrafast electrical writing operation of ferroelectric RAM with non-destructive magnetic reading operation of ferromagnetic RAM.

From the above discussion, it is evident that magnetization plays key role in obtaining ferroelectric properties in single-phase multiferroic materials. In this regard, it is crucial to study the magnetic properties of these materials in depth, which motivated us to carry out detailed magnetization studies on some selected multiferroic materials. Besides, due to lack of strong coupling between polarization and magnetization along with ferromagnetism and ferroelectricity at room temperature, these materials do not have application potential. Among all the multiferroic materials, $BiFeO_3$ is the only single phase compound which shows a magnetic and electric ordering along with a mutual coupling between them at room temperature. But, due to weak coupling and a tiny magnetization due to AFM ordering of Fe^{3+} moments, $BiFeO_3$ does not qualify for technological applications. This motivated us to look for a material with enhanced multiferroic properties at room temperature. In general, magnetic properties in $BiFeO_3$ originate from Fe^{3+} ions only, and the spin structure of Fe^{3+} moments forms a cycloidal structure with a periodicity ~ 62 nm in an AFM fashion which cancels macroscopic magnetization. So, it is interesting to modify the spatially modulated cycloidal spin chain to enhance magnetic properties. Doping at Fe site by magnetic or non-magnetic element can overcome the issue because some structural distortion in the crystal structure upon doping can break the cycloidal spin chain and hence enhance the magnetic properties. In this study, we have kept the Fe^{3+} concentration unchanged by substituting at Bi site only. For structural stabilization, we have substituted 10 wt% of La at Bi site. To enhance magnetic properties, we have substituted Gd at Bi site. Polycrystalline samples of all the compounds studied in this thesis work have been synthesized using solid-state reaction route and have studied their structural and electronic properties by employing X-ray diffraction (XRD), X-ray Photoemission spectroscopy (XPS), Raman Spectroscopy, Superconducting QUantum Interference Device (SQUID) based magnetometry, P-E loop tracing and magneto-electric coupling measurements.

1.6 Materials Investigated in this Thesis

The above discussion suggests that the ferroelectric and ME coupling properties in most of the multiferroic materials are sensitive to magnetic properties and detailed magnetization studies of these compounds are desirable. Inspired by those studies, we have studied structural, magnetic and electric properties of various multiferroic materials in the present thesis work, which include two type-I multiferroic materials ($BiFeO_3$ and $YMnO_3$) and one type-II multiferroic material ($GdFeO_3$). In case of $BiFeO_3$, we have studied ferroelectric, magnetic and ME coupling properties of polycrystalline $Bi_{0.9-x}Gd_xLa_{0.1}FeO_3$ (x = 0.0 & 0.05). In addition, we have studied structural and magnetic frustration in polycrystalline $YMn_{1-x}Ga_xO_3$ (x = 0.0, 0.03, 0.06& 33.33) compounds. In case of type-II multiferroic material, we have studied the magnetic properties of polycrystalline $GdFeO_3$. To support experimental results, we have performed Density Functional Theory (DFT) based computational studies on $GdFeO_3$.

1.7 Thesis Organization

The present thesis contains a total of eight chapters. It begins with a brief introduction (chapter 1) of multiferroic materials including a historical background. Then, we discuss various classes of single-phase multiferroic materials along with microscopic origin of multiferroism and magneto-electric coupling in those materials. Then, we discuss the importance of magnetization studies in these compounds followed by the motivations behind the thesis work. At the end of this chapter, we mention the compounds studied in the present thesis. In the next chapter (chapter 2), we discuss the working principles of various experimental techniques that are used to characterize the synthesized compounds. In the subsequent five chapters, we present the experimental observations, results and discussions of the samples studied in this work. In the last chapter (chapter 8), we discuss important conclusions and make suggestions for possible future work.

A brief introduction and working principles of various experimental techniques that have been used for this thesis work are discussed in the following chapter.

Chapter 2

Experimental Techniques

This chapter starts with a brief description of the procedure used in preparing polycrystalline samples that are studied in the present dissertation. Thereafter, we provide a brief introduction to the experimental techniques used, along with working principles of commercial equipment such as X-ray diffractometer, X-ray Photoelectron Spectrometer, VSM, SQUID magnetometer, Polarization - Electric Field (P-E) loop tracer etc.

2.1 Sample Preparation

All the polycrystalline samples studied in this thesis work have been prepared using high purity (99.99 %) oxide powders following conventional solid-state reaction method. The heat treatments, annealing atmospheres etc. associated with preparation procedure of each sample have been detailed in the beginning of respective chapters. In this section, we will discuss the basic principles of solid-state synthesis route and various steps involved therein.

- **Solid-state Reaction Method**

Solid-state reaction method is a well-known and most widely used method for preparation of polycrystalline samples of complex oxides using precursor oxides, nitrates, carbonates, oxalates, hydroxides, alkoxides and other metal salts. This method is relatively inexpensive and requires simple apparatus such as crucibles, furnaces etc. The process involves chemical decomposition of precursor materials upon heating to suitable temperature. The decomposed materials react with each other by inter-diffusion of cations to form new oxide materials and gases. Initially the reaction takes place rapidly because of short diffusion length, but further reaction proceeds slowly. In general, this process involves several annealing steps along with multiple intermediate grindings of the mixed precursors to increase homogeneity and reduced particle size of final product. Extra milling of the precursor oxides makes them more reactive

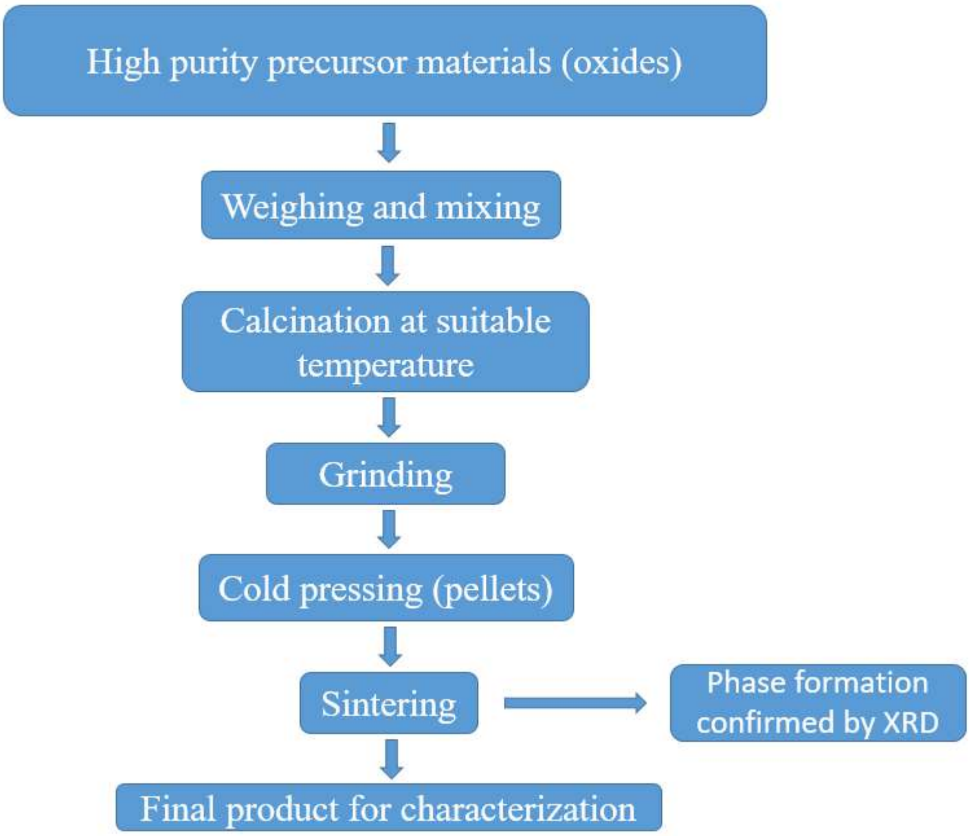

Figure 2.1: Schematic view of steps involved in solid-state reaction method for preparation of polycrystalline samples.

in the subsequent heat treatment. In some cases, some unwanted phases appear due to heating at inappropriate temperature and poor mixing of precursors. The complete steps associated with sample preparation are shown in the schematic view presented in figure 2.1.

2.2 X-ray Diffraction

The powder X-ray diffraction (PXRD) patterns of polycrystalline samples were recorded with an X-ray diffractometer, model: Rigaku Miniflex-600, employing a filtered Cu K_α radiation of average wavelength $\lambda = 1.5418$ Å. The PXRD patterns of each sample were recorded in the 2θ range of 10° - 80°. The experiments were performed with a step size $\Delta 2\theta \sim 0.0167^\circ$, sometimes even smaller $\Delta 2\theta \sim 0.002^\circ$, depending on the requirement.

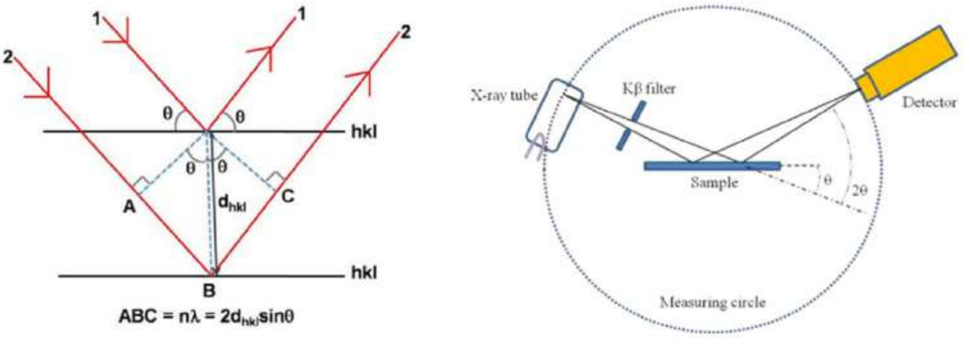

Figure 2.2: Schematic representation of Bragg's law and optics related to XRD experiment.

The X-ray generator was operated at a constant voltage of 40 kV and constant current of 30 mA supplied by a stabilized power supply. These experimental conditions were kept intact during the experiment. The schematic drawing of Bragg's law and optics involved in XRD are shown in figure 2.2. The fine polycrystalline powder of samples was kept on perspex glass substrate for irradiating with X-rays. The substrate has a rectangular crevice on the surface having an area of ~ 15 mm × 20 mm with 0.5 mm depth. Fine powder samples are filled in this rectangular apace and compacted by pressing the surface with a clean flat glass plate. A standard single crystal silicon sample has been used for calibration of the diffractometer for accurate measurement of 2θ position and instrumental broadening.

Phase analysis of studied samples was carried out using Fullprof Suite software [111] by performing Rietveld refinement to obtain accurate structural parameters.

- **Rietveld refinement method**

This method fits the experimental X-ray diffraction (XRD) data to a multivariable structure, profile models and background associated with the samples under investigation. In this method, the user defined parameters e.g. lattice parameters, atomic positions, unit-cell volume etc. are optimized following a least-squares method to minimize the difference between experimentally observed and calculated patterns based on the approximated crystal structure and instrumental broadening. The mathematical equation that governs the intensity calculated in Rietveld refinement at ith position is expressed as [112],

$$Y_{ci} = \left[\sum_{j} S_j \sum_{hkl_j} L_{hkl_j} \left| F_{hkl_j} \right|^2 \phi(2\theta_i - 2\theta_{hkl_j}) P_{hkl_j} A \right] + Y_{bi} \qquad (2.1)$$

where Y_{ci} and Y_{bi} are the calculated intensity and background contribution at point i. The expression for Y_{ci} and Y_{bi} can be written in a polynomial form or can even be constructed manually which needs to be imported explicitly and refined during the Rietveld-analysis. The parameters S_j and L_{hkl_j} are scaling and Lorentz-polarization factors [113] for jth phase. The parameter 'hkl' is the notation for Miller indices associated with Bragg reflection of jth phase. The Lorentz-polarization factor can be represented by the following equation,

$$L_{hkl_j} = \frac{(1 + A\cos^2 2\theta)}{(1 + A)\sin 2\theta} \qquad (2.2)$$

where the parameter$A = \cos^2 2\theta_M$, is the X-ray absorption factor of the sample while X-rays pass through it and θ_M is the Bragg angle of monochromator. The quantity F_{hkl_j} is the structure factor for reflection 'hkl' and can be represented as:

$$F_{k_j} = m_k \left| \sum_{n=1}^{N} f_n e^{-B_n \frac{\sin^2\theta}{\lambda^2}} \left(e^{2\pi i(hx_n + ky_n + lz_n)} \right) \right|^2 \qquad (2.3)$$

where the summation is over all N atoms, m_k is the multiplicity factor of the reflection with hkl Miller indices. $f_n\left(\frac{\theta}{\lambda}\right) = f_n\left({\sin\theta}/{\lambda}\right) + f_n' + if_n''$, and $(x_n, y_n, z_n)$are the coordinates of nth atom. The parameters f_n' and f_n'' are the real and imaginary parts of anomalous scattering factor. f_n is the normal structure factor represented by the following equation,

$$f = f_0 exp^{\left[-B\left(\frac{\sin\theta}{\lambda}\right)^2\right]} \qquad (2.4)$$

The parameter $B = 8\pi^2 U$ is associated with atomic temperature factor known as Debye-Waller factor where, $U = < u^2 >$ is mean squared displacement of atoms with respect to their equilibrium position. The displacement is due to lattice vibrations which increase with increasing temperature. While performing Rietveld-refinement, it is required to fit the peaks with a function called peak fitting function. The peak fitting function can be imported manually or set with the predefined functions in Fullprof suite program. In our cases, we have used Pseudo-Voigt (PV) peak fitting function which is a combination of Gaussian and Lorentzian functions. The mathematical expression of PV function can be represented as following,

$$PV\,(2\theta_i - 2\theta_k) = I_n \left[\eta_k \left\{ \frac{1}{1 + S_{i,k}^2} \right\} + (1 - \eta_k) e^{-S_{i,k}^2 ln2} \right] \qquad (2.5)$$

where $S_{i,j} = \frac{2\theta_i - 2\theta_k}{\omega_k}$. Here the shape of the peaks is accounted for by Caglioti formula,

$$\omega^2 = utan^2\theta + vtan\theta + w \qquad (2.6)$$

whereη_k, u, v and w are the parameters required to be refined during Rietveld refinement to get a good agreement between experimental and fitting patterns. In general, the quantity that is minimized during the refinement analysis is the residual S'_y which is related to observed and calculated intensities in the following way,

$$S'_y = \sum_i (Y_{oi} - Y_{ci})^2 \qquad (2.7)$$

Where y_{oi} and y_{ci} are the observed and calculated intensities at point i.

There are different R factors e.g. Profile value (R_p), Weighted value (R_{wp}), expected value (R_{exp}), Bragg value (R_B) and Goodness of fitting ($\chi = \frac{R_{wp}}{R_{exp}}$)that signify the quality of fitting [112, 114].Various$R$ factors are expressed in the following way,

$$R_p = \frac{\sum_i |Y_{io} - Y_{ic}|}{\sum_i Y_{io}} \qquad (2.8)$$

$$R_{wp} = \left[\frac{\sum_i w_i (Y_{io} - Y_{ic})^2}{\sum_i w_i Y_{io}}\right]^{1/2} \qquad (2.9)$$

$$R_B = \frac{\sum_k |I_{ko} - I_{kc}|}{\sum_k I_{ko}} \qquad (2.10)$$

$$R_{exp} = \left[\frac{E - P}{\sum_i w_i {Y_{io}}^2}\right]^{1/2} \qquad (2.11)$$

$$\chi^2 = \frac{\sum_i w_i (Y_{io} - Y_{ic})^2}{E - P} = \left[\frac{R_{wp}}{R_{exp}}\right]^2 \qquad (2.12)$$

Where E and P are the number of observations and the number of least square parameters that need to be estimated. $w_i = {}^{1}/_{Y_{oi}}$ is weight factor of ith data.

To get the structural parameters that are physically meaningful and correspond to global minima, the new values obtained after first cycle of refinement must be updated in the decomposition formula expressed in equation 2.1. This process must be repeated until satisfactory values of afore mentioned parameters are attained, based on the proposed structural model. The convergence of refinement can be understood in terms of acceptable values of different statistical agreement factors. The values of most of the statistical factors mentioned above depend on the difference or squared difference of experimentally observed (Y_{oi}) and calculated (Y_{ic}) intensities. It is worth mentioning that should PXRD patterns contain high background, it must be subtracted before calculating those statistical residuals. Else, the fitting may lead to unreliable agreement factors.

2.3 X-ray Photoelectron Spectroscopy

XPS is a quantitative spectroscopic technique which is widely used for stoichiometric analysis of bulk as well as thin film samples. It also allows assessing the valence state of constituent elements in the sample. The technique was first developed in the mid-1954s by Kai Siegbahn and his research group at the University of Uppsala, Sweden [115]. It is based on Einstein's Photoelectric Effect (1905) wherein the surface of the material is irradiated by a mono-energetic X-ray beam, typically K_α of Mg or Al source, causing the core electrons to be ejected [116, 117]. The penetration depth of the incoming X-ray beam is 5-10 nm, indicating that this technique provides information from the region close to the surface of the sample. The ejection of electrons from sample surface is governed by the following equation,

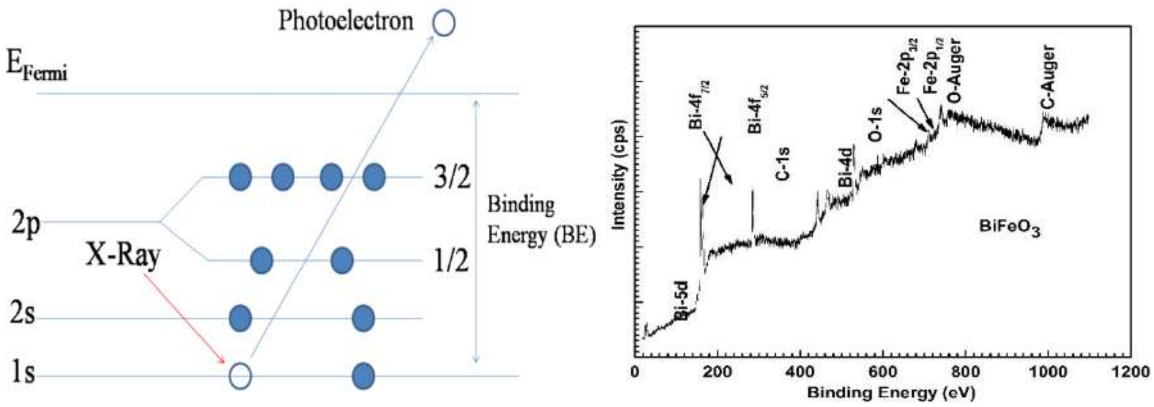

Figure 2.3: Schematic presentation of XPS process (left) and representative XPS spectrum of polycrystalline $BiFeO_3$.

$$E_B = h\nu - \varphi - E_C \qquad (2.13)$$

where E_C is the kinetic energy of the ejected electron (which can be measured by a coaxial cylindrical analyzer), φ is the work function of the spectrometer which can be calibrated with a reference material, hν is the energy of the incoming X-ray and E_B is the binding energy of the atomic orbital from which the electron is ejected. E_B can be extracted accordingly, which depends on the electronic configuration of the atoms and chemical surroundings.

Figure 2.3 shows the schematic representation of XPS process and a representative XPS spectrum of polycrystalline $BiFeO_3$. The peak at a binding energy provides the information of the element present in the sample and area under the peak is related to the relative concentration of the element. Thus, XPS data is useful in obtaining information on chemical states of elements from the variations in peak position and intensity in the XPS spectra. As for each element, there is a characteristic binding energy spectrum associated with a specific atomic orbital. Therefore, each element gives rise to a unique spectrum depending on the kinetic energies and hence binding energies of the ejected photoelectrons [118].

We have carried out X-ray Photoemission Spectroscopy (XPS) measurements using Mg-Kα(1253.6 eV) X-ray source and a DESA-150 electron analyzer (M/s. Staib Instruments, Germany).

2.4 Raman Spectroscopy

Raman scattering spectroscopy is an effective tool to get more insight into the local structure like distortion, disorder and the strain present in the sample. When a monochromatic light is incident on the sample, its interaction with the lattice phonons or molecules can result in reflection, absorption or scattering. Raman measurement is basically based on the analysis of the scattered light. The scattered radiation can be of two types, elastic and inelastic. The phenomenon involving inelastic scattering of light, first predicted by Smekal in 1923 and experimentally observed by C. V. Raman in 1928, is known as "Raman Scattering". In Raman measurements, a shift in change in frequency of scattered beam is measured [119]. When a monochromatic light of frequency ν_i is incident on the sample, the scattered light of frequency $\nu_s$is of two types, i) Rayleigh Scattering, having the frequency same as incident beam (i.e. $\nu_i = \nu_s$) and is stronger, and ii) Raman scattering, having a frequency different from incident frequency. If $\nu_s < \nu_i$, it is called Stokes scattering and if $\nu_s > \nu_i$, it is called anti-Stokes scattering. This change in frequencies is called Raman shift which provides chemical and structural information like bond vibrations of the compound. The fundamental requirement to get a Raman signal is that the vibrational modes or phonons must be spectroscopically Raman active. In order to generate a Raman peak, the incident phonon must change the bond polarizability upon exposure to light. It is important to study bond vibrations in multiferroic materials because they can induce multiferroicity.

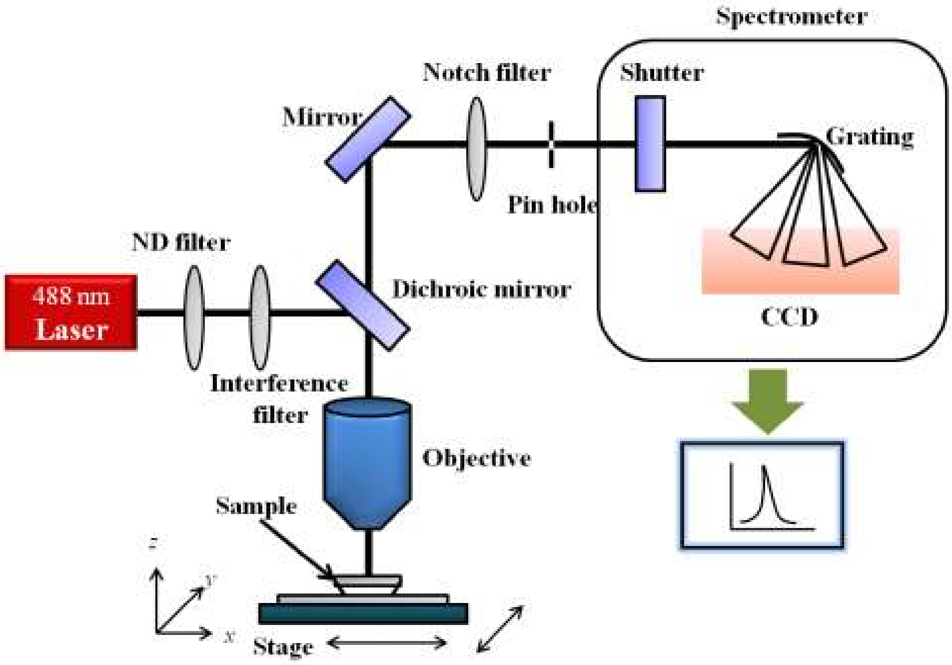

Figure 2.4: Schematic view of involved optics in Raman set-up.

A typical Raman spectrometer consists of the following parts: excitation source (laser), sample illumination and collection system, monochromator and detector as shown in the figure 2.4. As Raman effect is weak, lasers proved to be ideal sources due to their high power, monochromaticity, small diameter and ease to focus. In this thesis work, Raman spectroscopy measurements were carried out in the range 50 – 1000 cm^{-1} using Jobin-Yvon HR-800 Evolution spectrometer with a 532 nm laser and 600 rulings/mm grating, which gives a resolution of 1.5 cm-1 per pixel. ‘Microcal Origin’ software was used for de-convolution of the overlapping modes. The spectra were fitted with Lorentzian and/or Gaussian peak-shape functions to determine the characteristic parameters.

2.5 SQUID Magnetometer and VSM

We have used a Superconducting QUantum Interference Device (SQUID) magnetometer and a Vibrating Sample Magnetometer (VSM-PPMS) for magnetization measurements of our samples. In this section, we provide a brief description of working principles of SQUID magnetometer and VSM.

- **Superconducting Quantum Interference Device (SQUID) Magnetometer**

SQUID magnetometer is a highly sophisticated magnetic measurement system [120] which can detect even a tiny amount of magnetic moment present in the samples. Commercial magnetometers can detect moments as low as 10^{-8} emu. This tiny magnetic moment of a sample is detected by highly sensitive Josephson tunnelling junction which consists of two superconductors separated by an insulating material (superconductor-insulator-superconductor), called a SIS junction, invented by David Josephson in 1962.The working principle of SQUID is based on the tunnelling of super-currents through Josephson junction. Usually, when the Josephson junction is connected to a superconducting circuit, the quantum interference phenomenon take place i.e., the voltage across the Josephson tunnelling junction is a periodic function of the changing magnetic flux inside the circuit (pick-up coil). In the present case, we have used a RF SQUID magnetometer for measurements. A schematic drawing of a RFSQUID magnetometer, including a Josephson junction connected to LC circuit with an alternating current source of radio frequency, is shown in figure 2.5. The working principle of a RF SQUID magnetometer can be briefly described in the following way.

A RF SQUID based magnetometer consists of a single Josephson junction connected to a LC circuit. The behaviour of a RF SQUID can be understood in terms of inductance (L) of Josephson junction placed in a magnetic field. If a superconducting loop of inductance L, containing a single Josephson junction, is placed in a magnetic flux Φ_{ex}, then the total flux (Φ) through the loop is given by,

$$\Phi = \Phi_{ex} - LI \qquad (2.14)$$

where I is the current flowing in the loop.

Now, if δ is the phase difference between the cooper pair wave functions across the junction, the relation between δ and Φ can be written as:

$$\delta = 2\pi n - \frac{2q_e}{\hbar}\Phi \qquad (2.15)$$

where$n$ is an integer. q_e and $\hbar$ are electronic charge and reduced Planck constant respectively. Hence, the tunnelling current in the loop, $I = I_o \, Sin \, \delta$, can be expressed as,

$$I = I_0 \, Sin\left(2\pi n - \frac{2q_e}{\hbar}\Phi\right) \qquad (2.16)$$

Putting the expression of current in equation – 2.14, we get self-consistence equation for flux through the loop as following,

$$\Phi = \Phi_{ex} + LI_0 \, Sin\left(\frac{2\pi}{\Phi_0}\Phi\right) \qquad (2.17)$$

where Φ_0 is defined to be $\frac{h}{2q_e}$.

As mentioned above, RF SQUID consists of a single SIS junction in a superconducting loop coupled to an electric circuit driven by a RF current source. Hence, the loop would experience a flux (Φ_{RF}) generated by current flowing in it. When this loop is kept in some flux (Φ_s) that we want to measure, the total external flux would be, $\Phi_{ex} = \Phi_{RF} + \Phi_s$. Now, considering equation – 2.17, one can plot Φ vs Φ_{ex} which is shown in figure 2.5 (right half). If, the RF current and hence flux (Φ_{RF}) changes with time as shown in orange colour in figure 2.5, then Φ trances out the paths shown by blue colour on account of flux quantum entering/leaving during the upward/downward transition. The amount of current and thus Φ_{RF} that needs to be supplied in the loop to preserve the energy during transition depends on the measuring flux (Φ_s). As the output of RF SQUID is associated with voltage, the Φ_s is measured in terms of voltage.

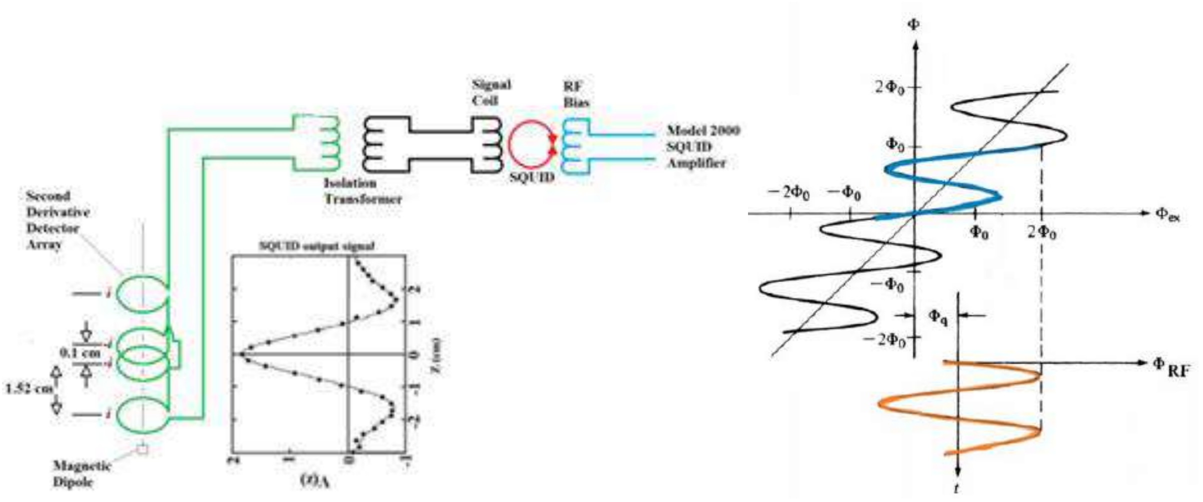

Figure 2.5: (Left) Schematic drawing of the basic circuitry of RF SQUID based magnetometer used for studies described in the thesis: a single Josephson junction (red coloured loop) is coupled to a LC circuit containing RF current generator. The distances between pickup coils in second-order gradiometer configuration are shown in green colour. The output of SQUID as a function of sample position is plotted (graph in black colour) when the sample (a magnetic dipole) is moved through the coils. (Right) A plot of total measured flux (Φ) vs external flux (Φ_{ex}) (graph in blue colour) in an oscillating flux (Φ_{RF}) (graph in orange colour).

It is noteworthy to mention that SQUID is a transducer which converts flux to an oscillatory function of voltage. Hence, usually it is used operating in flux-locked loop to linearize its response [121, 122]. We provide below a brief description of normal measurement scheme of a RF SQUID magnetometer.

Measurement Scheme

The general measurement scheme used in Magnetic Property Measurement System (MPMS) involves two major steps: sample transport through the detection coils and output signal analysis for extraction of magnetic moment associated with the sample. With regard to sample transport, initially the sample is positioned far below the detection coils (magnetic dipole position in the left half of figure 2.5). Then the sample is moved upwards through the detection coils which are wound in a second-order derivative configuration (coils in green colour in figure 2.5), while simultaneously measuring the output of the SQUID detector. The sample is moved for a specified scan length. During this scanning, the sample is stopped at a number of positions and at each position several readings of SQUID voltage are collected and averaged. The complete scan can be repeated a number of times and the signal is averaged to get a better signal to noise ratio. Since the sample is moved through a second-derivative gradiometer in which the extreme upper and lower turns are counterwound, the shape of SQUID output voltage is the second derivative of a Gaussian function with respect to position of the sample, as shown in figure 2.5. The counterwound turns are important since they reject the signals coming from nearby magnetic sources e.g. superconducting shielding of SQUID sensing loop. The extraction of magnetic moment associated with sample from SQUID output voltage is done using an algorithm. There are three different methods of moment extraction. These are full scan, linear regression and iterative regression. In our measurements, we have used linear regression method for analysis of SQUID output voltage. In this method, the SQUID output voltage is fitted using a linear regression algorithm to an expected theoretical signal when a unit magnetic dipole is moved through a second-order gradiometer.

For the work included in the thesis, we have used the SQUID magnetometer of M/s. Quantum Design make (model no. MPMS), with temperature and field ranges of 5 K – 300 K and ±50 kOe respectively.

- **Vibrating Sample Magnetometer (VSM)**

Vibrating Sample Magnetometer (VSM) is a versatile instrument used to measure magnetic moments of sample. The sensitivity of this instrument is ~ 10^{-5} emu. It also works on Faraday's law of induction which tells us that changing magnetic field (B) will induce a voltage(V). This induced voltage can be measured to provide information about the changing magnetic field. In case of tightly wound coils of cross-sectional area 'A' and 'N' number of turns placed in an external magnetic flux 'B' which is changing with time, the induced electromotive force (V) in the coil is given by the following equation,

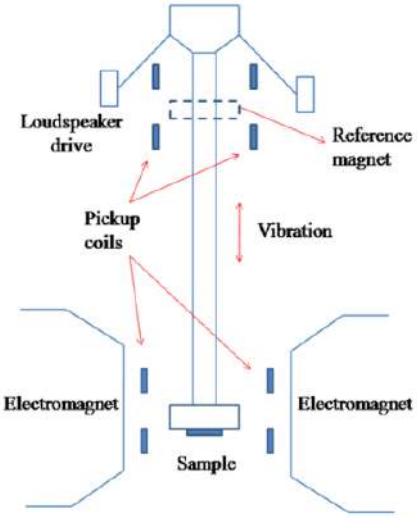

Figure 2.6: Schematic view of sample space of VSM.

$$V = -NA\left(\frac{\partial B}{\partial t}\right) \qquad (2.18)$$

The direction of 'V' is governed by Lenz's law. If the coil is kept in a constant magnetic field of H, the associated magnetic flux is given by,

$$B = \mu_0 H \qquad (2.19)$$

In the presence of a sample exhibiting magnetization M, the magnetic field is modified and flux linked to resultant field would be,

$$B = \mu_0 (H + M) \qquad (2.20)$$

Hence, the corresponding flux change,

$$\Delta B = \mu_0 M \qquad (2.21)$$

The induced EMF due to flux changes associated with the magnetic sample as obtained from equation 2.18,

$$Vdt = -NA\mu_0 M \qquad (2.22)$$

Thus, it is clear from above equation that the output signal of VSM depends only on M associated with sample under investigation and independent of external magnetic field H. A schematic diagram of sample space is presented in figure 2.6. In VSM, the sample under investigation is placed in between the poles of an electromagnet (see figure 2.6) where the sample faces a constant magnetic field. The sample is held in a non-magnetic sample holder and connected to transducer for vibration of the sample. The change in magnetic flux associated with magnetization of the sample is detected by a pick-up coil and then amplified by a lock-in amplifier. The signal in the pick-up coil is proportional to the magnetization of the sample. However, it is also proportional to the amplitude and frequency of vibration of the sample. Hence, to avoid undesirable signal, a nulling method is used by employing a vibrating capacitor as a reference signal.

Here we have used the VSM-PPMS instrument (M/s. Quantum Design, model: PPMS) with temperature and field ranges of 1.8 K – 300 K and ±140 kOe respectively.

2.6 Polarization-Electric Field (P-E) Loop Tracer

To understand the multiferroic properties of materials, it is important to characterize ferroelectric properties of that material. The existence of spontaneous polarization and ferroelectric hysteresis loop are the hallmark of a ferroelectric material in which the polarization (P) can be switched by application of electric field (E). A P-E loop of a material is a plot of charge or polarization as a function of applied electric field measured at a particular frequency. Using this method one can measure the important parameters of a material such as maximum polarization (P_{max}) at a particular field, remnant polarization (P_r) and coercive field (E_c).

A traditional and frequently used method for P-E measurement is based on Sawyer-Tower circuit. In 1930, scientists Sawyer and Tower published a paper [123] on development of this technique and did some seminal measurement on Rochelle salt. Figure 2.7 shows a schematic diagram of Sawyer-Tower circuit and a typical ferroelectric hysteresis loop [124].

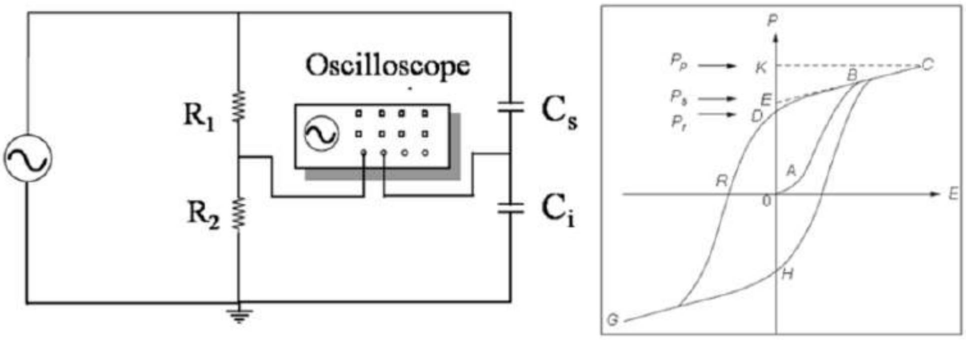

Figure 2.7: Schematic drawing of P-E loop tracing circuit (left) and a typical P-E hysteresis loop of a ferroelectric material (right).

The circuit consists of a signal generator, an oscilloscope, two capacitors in series labelled C_s (ferroelectric sample) and C_i (internal reference) and load resistance R (a series combination of R_1 and R_2). As the capacitors are in series, the charge ($Q = C \times V$) on both the capacitors will be the same. Now, considering the following equations from the Sawyer-Tower circuit shown in figure 2.7,

$$C_i \times V_i = C_s \times V_s \qquad (2.23)$$

and
$$V_T = V_s + V_i \qquad (2.24)$$

where, V_T is the total applied voltage and V_i is the voltage that can be measured. If we know the internal reference capacitance (C_i) value, capacitance of the sample (C_s) can be calculated using equations 2.23 & 2.24. Now, multiplying C_s with V_s, we can get the charge on the measured sample and from thereon, using the known dimensions of the sample, one can find out the polarization value on the sample [125].

Figure 2.7 shows typical P-E loop of a ferroelectric material. Initially, on application of a small field, a field induced polarization occurs as represented by OA leg in the plot. On increasing the applied field, polarization increases and follows AB path as more number of domains align with the field direction. If we further increase the field, the polarization attains a maximum value (path BC) as maximum number of domains align in the field direction. On decreasing the applied field, the polarization decreases and follow path CBD. The extrapolation of CB path to zero applied field gives spontaneous polarization (P_s) in the material, while point D provides remnant polarization (P_r). The field require to bring the polarization to zero is called the coercive field (E_c) of the material, which depends on the frequency of applied field, temperature of the material and waveform applied.

The P-E measurements on all the samples were carried out using aixACCT's TF analyser 2000 on circular pellets of 6 mm diameter and less than 1 mm thickness.

2.7 Magneto-electric Measurement

Measurement of Magneto-electric (ME) coupling coefficient is important to understand the mutual dependency of electric and magnetic degrees of freedom. As there is a lack of well-established technique for this measurement, researchers adopt different techniques to measure ME effect. Some of the extensively used techniques are described below:

a) Magneto-capacitance/magneto-dielectric measurement: In this method, the dielectric constant of the sample is measured both in the presence and absence of an external magnetic field [126]. Any change in the dielectric constant observed in this experiment gives an idea of ME effect. It is an indirect way to measure ME coupling. Sometimes, the change in dielectric constant may originate due to magneto-resistive behaviour of the sample, so the change in dielectric constant may not be ME coupling [127].

b) Pyroelectric current measurement: Pyroelectric current of a sample measures the spontaneous change of polarization as a function of temperature. If the material shows ME effect, a large change in pyroelectric current is observed in the presence of an external magnetic field near magnetic transition temperature [128].

c) Piezo-electric measurement: The ME coupling coefficient of a sample can be measured in terms of piezo-electric response by applying stress and magnetic field simultaneously. The slope of the variation of piezoelectric response as a function of applied magnetic field will give ME coupling coefficient [129].

d) Scanning probe microscopy measurement: Scanning probe microscopy like magnetic force microscopy (MFM) and piezoelectric force microscopy are used to explore the presence of ME coupling in the sample. Particularly, PFM and MFM are used together to describe strain mediated ME effect in the sample [130].

e) Measurement of magnetization induced by an external electric field: A Vibrating Sample Magnetometer (VSM) or SQUID magnetometer is used to measure the magnetization of the sample after exciting it with an external electric field [131]. Here, magnetization is measured as a function of electric field. This is a little complicated procedure because physical movement of delicate sample holder may affect electrical connections to the sample.

f) Measurement of electric polarization induced by an external magnetic field: In this technique, the polarization of the sample is measured as a function of external magnetic field. This method is more convenient than the previous one. In this case, the sample is exposed to a unidirectional magnetic field generated by an electromagnet having high input impedance, preferable varying at a slower rate, say, 0.05T/min i.e quasi-static method [132]. An improvement of the method involves measuring the generated voltage with ac and dc magnetic fields applied simultaneously to the sample. The method of magnetoelectric voltage measurement carried out in this thesis work is described below.

The magnetoelectric voltage measurements were carried out at room temperature by adopting a dynamic process [133]. The measurement set-up makes use of a Helmholtz-coil (diameter 8 mm) having 125 turns of winding on each side with a separation of 4 mm, to generate ac magnetic field. The sample in the form of a pellet is mounted on a mica-sheet and placed between the coils. Being a bad electrical conductor and a good thermal conductor, mica-sheet ensures thermal contact between the sample and the thermometer. The temperature of the sample was measured using a Pt-100 thermometer mounted close to the sample. An electromagnet was used to generate dc magnetic field in the range ±10 kOe using a bipolar power supply. Figure 2.8 shows a schematic view of sample holder and samples space between the poles of electromagnet (reprint). The direction of sample surface was parallel to both ac and dc magnetic fields. Conducting silver paste epoxy was used to electrically connect the sample to the measuring probes and coaxial wires were used to supply AC signal to Helmholtz coil (see figure 2.8) and to measure induced ME voltage.

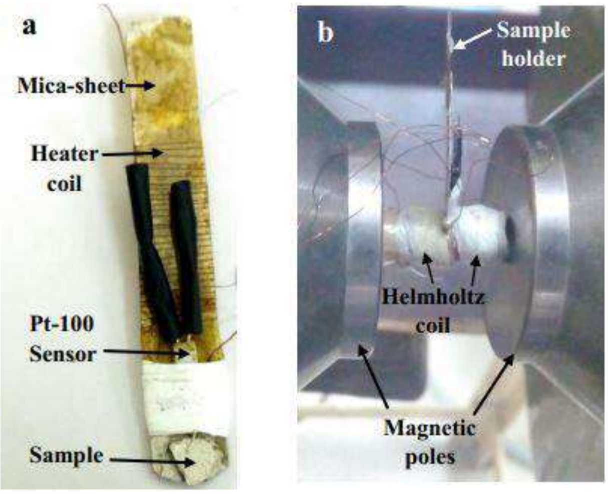

Figure 2.8: Schematic view of (a) mica-sheet sample holder and (b) Helmholtz-coil with sample holder in between the poles of electromagnet.

In this measurement, the samples were excited with an AC magnetic field, $h = h_0 sin\omega t$ along with a DC magnetic field. Here, $h_0 = 20$ Oe and $\omega = 2\pi f$, $f$being the frequency of applied AC signal. When a DC magnetic field is applied across the sample, the magnetic field induced voltage (odd contribution due to magneto-electric effect and even contribution due to magneto-conduction effect) (MIV) in the sample can be expressed as a polynomial of applied magnetic field H as [134],

$$V = E.d = \alpha H + \beta H^2 + \gamma H^3 + \delta H^4 + \ldots. \qquad (2.25)$$

where E and d are the electric field across the sample and pellet (sample) thickness respectively. On superposition of AC magnetic field over the DC field, the modulated magnetic field faced by the sample is,

$$H_m = H + h_0 sin\omega t \qquad (2.26)$$

Inserting H_m in equation 2.25, we get,

$$V = \alpha(H + h_0 sin\omega t) + \beta(H + h_0 sin\omega t)^2 + \gamma(H + h_0 sin\omega t)^3 + \ldots. \qquad (2.27)$$

whereα, β, γ, etc., are first, second, third order magneto-electric coefficients respectively. Now, considering the coefficient of $sin\omega t$, we get,

$$V' = h_0(\alpha + 2\,\beta H + 3\gamma H^2 + \ \ldots) \qquad (2.28)$$

Hence, the expression for magneto-electric coefficients is obtained as follows,

$$\frac{dE}{dH} = \frac{V'}{h_0 d} = \frac{\alpha + 2\,\beta H + 3\gamma H^2 + \ \ldots}{d} \qquad (2.29)$$

So, by measuring the magnetic field induced voltage across the sample, one can estimate magneto-electric coefficient.

Our computational and/or experimental observations on various samples studied in this thesis work have been discussed in detail in ensuing chapters. The following chapter provides basic principles of DFT and a brief discussion of computational tools, along with results obtained for $GdFeO_3$.

Chapter 3

Density Functional Theory Based Computational Study on $GdFeO_3$ Using Vienna Ab-initio Simulation Package (VASP)

This chapter presents the electronic structure and magnetic properties of $GdFeO_3$ modelled using Density Functional Theory (DFT) based computational methods. At the onset, we have provided a brief introduction to the theory behind DFT based computation, including Schrodinger equation, Khon-Sham equation, Exchange-correlation functional, Pseudo-potentials etc. A brief description of input and output files of Vienna Ab-initio Simulation Package (VASP) has been given followed by the structural optimization for $GdFeO_3$. Finally, the magnetic properties of various spin configurations of Gd and Fe moments in $GdFeO_3$ have been investigated systematically and a comparison has been made between our results and literature reports.

3.1 Density Functional Theory

DFT is a computational quantum mechanical modeling method that is used to investigate electronic properties, principally in the ground state of many-body systems in material science. This computational method became very popular after 1990s when approximations began to be used in the theory, which led to a better understanding of exchange and correlation interactions. The basis of DFT is that any property of a system of many interacting particles can be described in terms of functional ground state electron density $n_0(\vec{r})$. The great advantage of DFT method is that it does use total electron density as a basic function instead of N-body electron wave functions of the electrons. Moreover, with increasing electron number, the density also increases and easier to calculate. Hence, DFT improves the calculation accuracy significantly over previously used Hartree-Fock (HF) method.

3.1.1 Quantum mechanics and Schrodinger equation

To investigate electronic structure of a solid, one needs to calculate total energy of the system and subsequent minimization of that energy with respect to atomic coordinates. The minimum energy state corresponds to ground state of the system under investigation.

Approximations play a very important role in computational studies. For example, if one considers a single atom under investigation, simple non-relativistic theory is a very good approximation. However, if one considers electrons, nucleus, atoms etc. for investigation, then relativistic case is necessary.

Consider a system which is described by M nuclei and N electrons whose position vectors are $\vec{R}_A$ and $\vec{r}_i$ respectively. The corresponding Hamiltonian operator (**Hamiltonian**) of the system considering a Coulombic interaction between them, is given by,

$$\widehat{H} = \widehat{K}_A + \widehat{K}_i + V_{A-i} + V_{i-i} + V_{A-A} \qquad (3.1)$$

The above equation can be expressed in the following way considering atomic units i.e. $m_e = \hbar = e^2/(4\pi\epsilon_0) = 1$,

$$\widehat{H} = -\sum_{A=1}^{M}\frac{1}{2M_A}\nabla_A^2 - \sum_{A=1}^{M}\frac{1}{2}\nabla_i^2 - \sum_{i=1}^{N}\sum_{A=1}^{M}\frac{Z_A}{|\vec{r}_{iA}|} + \sum_{i=1}^{N}\sum_{j>1}^{N}\frac{1}{|\vec{r}_{ij}|} + + \sum_{A=1}^{M}\sum_{B>A}^{M}\frac{Z_A Z_B}{|\vec{R}_{AB}|} \qquad (3.2)$$

where the first two terms are the kinetic energy operators associated with nuclei ($\widehat{K}_A$) and electrons ($\widehat{K}_i$), latter terms correspond to the Coulombic interaction between nucleus and electron (V_{A-i}), electron and electron (V_{i-i}), and nucleus and nucleus (V_{A-A}) respectively. The ground state energy of the system is calculated by solving the Schrodinger equation which is nothing but an eigen value problem, described by,

$$\widehat{H}\Psi = E\Psi \qquad (3.3)$$

The expression for $\hat{H}$ is shown in equation (3.2). So, we get,

$$\left| -\sum_{A=1}^{M} \frac{1}{2M_A} \nabla_A^2 - \sum_{A=1}^{M} \frac{1}{2} \vec{\nabla}_i^2 - \sum_{i=1}^{N} \sum_{A=1}^{M} \frac{Z_A}{|\vec{r}_{iA}|} + \sum_{i=1}^{N} \sum_{j>1}^{N} \frac{1}{|\vec{r}_{ij}|} + + \sum_{A=1}^{M} \sum_{B>A}^{M} \frac{Z_A Z_B}{|\vec{R}_{AB}|} \right| \Psi = E\Psi \qquad (3.4)$$

E is eigenvalue of the system and $\Psi = \Psi\,(\vec{r}_1, \vec{r}_2, \ldots, \vec{r}_N;\ \vec{R}_1, \vec{R}_2, \ldots, \vec{R}_M)$ is the many-ion may-electron wave function. The condition for solving equation (3.4) is

$$< \Psi | \Psi > \; = 1 \qquad (3.5)$$

Unfortunately, it is very difficult and simultaneously time consuming to solve equation (3.4) exactly due to the involvement of a large number of variables. To find out the energy eigen value associated with a practical system, it is necessary to make several approximations as discussed below.

3.1.2 The Born-Oppenheimer Approximation

The fundamental idea behind the Born-Oppenheimer approximation is the separation of nuclear and electronic motion because of the large difference in nuclear (M_A) and electronic (m_e) masses ($\frac{M_A}{m_e} \geq 1857$) [135] leading to different time scales. For example, the frequencies of ionic vibrations in molecules or solids are ~ 10^{12} Hz, whereas the transition between electronic eigenstates in atoms leads to the electromagnetic radiation in the frequency range of 10^{17} - 10^{18} Hz. This approximation results in a molecular wave function defined in term of electronic and nuclear position coordinates. The Born-Oppenheimer approximation is stated as follows,

1. The electronic wave function depends upon the nuclear coordinates but not upon nuclear velocity because the nuclear motion is much slower than electronic motion. The nuclei are assumed to be fixed with respect to electrons.
2. The nuclei feel a smeared out potential due to electrons moving with high velocity.

In the Born-Oppenheimer approximation, the Schrodinger equation of sub-system associated with electrons in solid can be represented in the following way,

$$\left(K_i + V_{A-i}\left(\{\vec{R}_A\}\right) + V_{i-i}\right)\Psi_1(\vec{r}_1,\vec{r}_2,\ldots..,\vec{r}_N) = E(\{\vec{R}_A\})\Psi_1(\vec{r}_1,\vec{r}_2,\ldots..,\vec{r}_N) \qquad (3.6)$$

where $\vec{R}_A$ is ionic position vector which is just an external parameter, not a dynamic variable. Similarly, the Schrodinger equation associated with ionic sub-system can be described in the following way,

$$\left(K_A + E(\{\vec{R}_A\} + V_{A-A}\right)\Psi_2(\vec{R}_1,\vec{R}_2,\ldots..,\vec{R}_M) = E\Psi_2(\vec{R}_1,\vec{R}_2,\ldots..,\vec{R}_M) \qquad (3.7)$$

Still, solving equations (3.6) and (3.7) is difficult and so, more simplifications are needed.

3.1.3 The Hohenberg-Kohn Theorems

The Hohenberg-Kohn theorems were introduced to better describe the system consisting of electrons which are moving under the influence of an external potential. The theorems are stated as follows,

Theorem 1 (existence theorem)

The ground state of any interactive many electron system can be described as a unique functional of electron density [136]. This means that the total energy of a many electron system in an external potential $V_{ext}(\vec{r})$ is a unique functional of electron density $\rho(\vec{r})$, *i.e.*

$$E[\rho(\vec{r})] = \int \rho(\vec{r})V_{ext}(\vec{r})d^3\vec{r} + F[\rho(\vec{r})] \qquad (3.8)$$

where the first term corresponds to the interaction energy of electrons with an external potential and the last term is associated with the kinetic energy and electron-electron interaction energy which is a universal functional.

Theorem 2 (variational principle)

The electron density that minimizes the functional of the system is the true electron density associated with ground state. At this stage, the functional $E[\rho(\vec{r})]$ has a minimum relative to the all other variations of density *i.e.*

$$\left.\frac{\partial E[\rho(\vec{r})]}{\partial \rho(\vec{r}\,)}\right|_{\rho(\vec{r})=\rho_0(\vec{r})} = 0 \qquad (3.9)$$

The main drawback of Hohenberg-Kohn (H – K) theorems was that they do not provide any idea about the exact form of the functional $F[\rho(\vec{r})]$ without which one cannot find the ground state electron density of the system in practice. About one year after the publishing of H – K theorems, Kohn – Sham proposed a simple theory of carrying out DFT calculations which provides a way to calculate the ground state electron density.

3.1.4 Kohn – Sham Theory

Kohn – Sham proposed a method to find out the ground state energy of interactive many particles system [137]. The fundamental idea in this theorem is to replace the interactive system by a non-interactive one, assuming that it exhibits the same electronic state. All the contribution to the total energy of the system can be expressed in term of electronic density of states $\rho(\vec{r})$. The Kohn – Sham method is particularly based on the parameterization of $\rho(\vec{r})$ in terms of one-electron orbitals $\varphi_i(\vec{r})$, i.e.,

$$\rho(\vec{r}) = \sum_i \varphi_i^*(\vec{r})\varphi_i(\vec{r}) \qquad (3.10)$$

and the total energy of the system can be expressed by parts as a function of $\rho(\vec{r})$ as:

$$E[\rho(\vec{r})] = K[\rho(\vec{r})] + E_H[\rho(\vec{r})] + E_{xc}[\rho(\vec{r})] + E_{ext}[\rho(\vec{r})] \qquad (3.11)$$

where,

$$E_H[\rho(\vec{r})] = \iint \frac{\rho(\vec{r})\rho(\vec{r}')}{|\vec{r} - \vec{r}'|} d\vec{r} d\vec{r}' \qquad (3.12)$$

$$E_{ext}[\rho(\vec{r})] = \int V_{ext}(\vec{r})\,\rho(\vec{r})\,d\vec{r} \qquad (3.13)$$

are the electron-electron Coulombic interaction energy and interaction energy with external field respectively.

The kinetic energy term can be described within the framework of non-interacting particle states $\varphi_i(\vec{r})$ as,

$$K[\rho(\vec{r})] = \sum_i \int \varphi_i^*(\vec{r})\left(-\frac{1}{2}\vec{\nabla}_i^2\right)\varphi_i(\vec{r})\,d^3r \qquad (3.14)$$

The other contributions to total energy are accounted for in the exchange-correlation energy term, $E_{xc}[\rho(\vec{r})]$. As one-electron orbitals are variational quantities, the variation of total energy functional expressed in equation (3.11) with respect to the orbital, $\varphi_i^*(\vec{r})$ results in one electron equation. Differentiating equation (3.11) with the variable $\varphi_i^*(\vec{r})$, we get,

$$\left(-\frac{1}{2}\vec{\nabla}_i^2 + \int \frac{\rho(\vec{r}')}{|\vec{r} - \vec{r}'|}d^3\vec{r}' + V_{ext}(\vec{r}) + \frac{\delta E[\rho(\vec{r})]}{\delta\rho(\vec{r})}\right)\varphi_i(\vec{r}) = \varepsilon_i\varphi_i(\vec{r}) \qquad (3.15)$$

For simplification, we assume that,

$$V_{eff}(\vec{r}) = \int \frac{\rho(\vec{r}')}{|\vec{r} - \vec{r}'|}d^3\vec{r}' + V_{ext}(\vec{r}) + V_{xc}(\vec{r}) \qquad (3.16)$$

and

$$V_{xc}(\vec{r}) = \frac{\delta E[\rho(\vec{r})]}{\delta\rho(\vec{r})} \qquad (3.17)$$

Equation (3.17) is the variational derivative of exchange-correlation energy with respect to density of electron, known as exchange-correlation potential. Hence, equation (3.15) is reduce to,

$$\left(-\frac{1}{2}\vec{\nabla}_i^2 + V_{eff}(\vec{r})\right)\varphi_i(\vec{r}) = \varepsilon_i\varphi_i(\vec{r}) \qquad (3.18)$$

Equation (3.18) is known as **Kohn – Sham equation**. ε_i introduced in **Kohn – Sham equation** do not represent true energy of the system, but are Lagrange parameters that preserve the orthogonality condition,

$$\int \varphi_i^*(\vec{r})\varphi_i(\vec{r})\, d^3\vec{r} = \delta_{ij} \qquad (3.19)$$

The only unknown quantity in **Kohn – Sham equation** is the exchange-correlation parameter. Due to complexity, several approximations need to be made to evaluate the exchange-correlation term.

3.1.5 Exchange-correlation Functional

Several methods have been proposed to calculate the exchange-correlation functional. Some important methods e.g. Local Density Approximation (LDA), Generalized Gradient Approximation (GGA) etc., have been discussed below.

3.1.5.1 Local Density Approximation (LDA)

This is one type of approximation to the exchange-correlation (XC) functional in the DFT, and probably the most important one, proposed by Hohenberg and Kohn in their first DFT paper [2]. It has been derived from Homogeneous Electron Gas (HEG) model. Considering electrons to be a homogeneous electron gas, the LDA approximation assumes that the electron density changes slowly on atomic scale [138]. So, an inhomogeneous electron system in practice can be considered as a homogeneous electron system for which the exchange-correlation energy is known precisely.

The LDA is only dependent on local density, and in general, the exchange-correlational energy of a spin-un-polarized system in LDA framework can be described by,

$$E_{xc}^{LDA}[\rho(\vec{r})] = \int d^3\vec{r}\,\rho(\vec{r})\varepsilon_{xc}[\rho(\vec{r})] \qquad (3.20)$$

where $\varepsilon_{xc}[\rho(\vec{r})]$ is the exchange-correlation energy density corresponding to a homogeneous electron gas system with the electron density $\rho(\vec{r})$.

3.1.5.2 Local Spin-Density Approximation (LSDA)

The LDA does not consider the spin of the electron in calculations. So, LDA provides a poor explanation for the properties that are spins dependent such as magnetism. An extension of LDA has been developed which accounts for electron spins to calculate the exchange-correlation energy of the system, known as Local Spin-Density Approximation (LSDA) [139].

The exchange-correlation energy considering the spins in the spin-polarized system can be represented in the following way,

$$E_{xc}^{LSDA}[\rho_\alpha(\vec{r}),\rho_\beta(\vec{r})] = \int d^3\vec{r}\,\rho(\vec{r})\varepsilon_{xc}[\rho_\alpha(\vec{r}),\rho_\beta(\vec{r})] \qquad (3.21)$$

where $\rho_\alpha(\vec{r})$ and $\rho_\beta(\vec{r})$ are two spin densities with the constrain $\rho = \rho_\alpha(\vec{r}) + \rho_\beta(\vec{r})$. The spin-dependent calculation is performed by the introduction of relative spin-polarization factor defined by,

$$\zeta = \frac{\rho_\alpha(\vec{r}) + \rho_\beta(\vec{r})}{\rho_\alpha(\vec{r}) - \rho_\beta(\vec{r})} \qquad (3.22)$$

where the allowed values of ζ are 0, +1 and -1. A system with $\zeta = 0$ indicates paramagnetic spin un-polarized situation with equal ρ_α and ρ_β spin densities. Whereas, $\zeta = \pm 1$ corresponds to fully spin polarized situation. In this case one particular type of spin vanishes.

The E_{xc}^{LSDA} can also be expressed in terms of individual spin un-polarized functional in the following way,

$$E_{xc}^{LSDA} = \frac{1}{2}[E_{xc}[2\rho_\alpha] + E_{xc}[2\rho_\beta]] \qquad (3.23)$$

The LSDA provides a reasonable explanation of molecular properties such as crystal structure, molecular vibration, charge, magnetic moment etc. But when the electronic density varies rapidly, it provides a poor explanation for energy related details such as energy barriers, bond vibration etc.

3.1.5.3 Generalized Gradient Approximation (GGA)

The drawbacks of LDA have been solved by proposing Generalized Gradient Approximation (GGA) which is based on the non-homogeneous electron gas assumption and also takes care of non-local electron effects. GGA has been derived from the extension of LDA and is a Gradient Expansion approximation (GEA). This exchange correlation functional attracts the computational research communities because of its accuracy in calculations and reasonable explanation of electronic properties.

GGA was first proposed by Perdew [140] by introducing a cutoff procedure that sharply terminates the GEA exchange-correlation functional using a delta function. The GGA exchange-correlation energy term can be described by considering the gradient of electronic density $\vec{\nabla}\rho$,

$$E_{xc}^{LSDA}[\rho(\vec{r})] = \int d^3\vec{r}\,\rho(\vec{r})\varepsilon_{xc}^{homo}[\rho(\vec{r})]F_{xc}[\rho(\vec{r}),\vec{\nabla}\rho(\vec{r})] \qquad (3.24)$$

where $F_{xc}[\rho(\vec{r}),\vec{\nabla}\rho(\vec{r})]$ is known as enhancement factor.

Because of very good results of molecular geometries and ground state energies, GGA implementations have become a standard choice for calculations. There are several GGA exchange-correlation functionals developed by various groups [141-144].

The exchange-correlation functional that leads to more accurate results than GGA functional is the meta-GGA which basically includes more terms in the expansion. Generally, it includes the gradient of the electronic density and second derivative (Laplacian) of electronic density. Here, we have used Perdew – Bruke – Ernzerhof exchange correlation functional for the calculation of atomization energy and electronic properties of $GdFeO_3$.

3.1.6 The Bloch Theorem

The DFT calculations on an infinite system (e.g. solid) assume that its crystal structure is homogeneous in all direction and the periodic boundary condition (PBC) is applicable. Using PBC, the infinite system is represented by a unit cell, and this model is assumed to be stable when the total energy and forces in the system converge. For practical calculations, we use a set of coordinates of atoms that build up a super-cell associated with a periodic arrangement of atoms that obey the translational symmetry.

The Bloch theorem states that the solution of Schrodinger equation of electrons in periodic potentials take a form of plane wave modulated by a periodic function [145, 146]. Mathematically, this can be represented as,

$$\Psi_{n\vec{k}}(\vec{r}) = e^{i\vec{k}.\vec{r}} u_{n\vec{k}}(\vec{r}) \qquad (3.25)$$

where n is the 'discrete index' also called the 'Band Index', $\vec{k}$ is the wave vector which can be restricted to the first Brillouin zone of the reciprocal lattice without loss of generality. The eigen states $\Psi_{n\vec{k}}(\vec{r})$ are called Bloch functions. Vector $u_{n\vec{k}}(\vec{r})$ is the modulating periodic function which is translationally invariant, i.e.,

$$u_{n\vec{k}}(\vec{r} + \vec{R}_s) = u_{n\vec{k}}(\vec{r}) \qquad (3.26)$$

where $\vec{R}_s$ is a vector in direct space of crystal lattice. The Bloch functions transform under a translational by lattice vector $\vec{R}_s$ in the following way,

$$T_{vec,\vec{R}_s}\Psi_{n\vec{k}}(\vec{r}) = \Psi_{n\vec{k}}(\vec{r}+\vec{R}_s) = e^{i\vec{k}.\vec{R}}\Psi_{n\vec{k}}(\vec{r}) \qquad (3.27)$$

In reciprocal space, $\Psi_{n\vec{k}}(\vec{r})$ varies with reciprocal vector $\vec{k}$ within a band (for a constant n value) and the energy does the same. $\Psi_{n\vec{k}}(\vec{r})$ remain constant up to a constant lattice vector $\vec{K}$ in reciprocal space, i.e.,

$$\Psi_{n\vec{k}+\vec{K}}(\vec{r}) = \Psi_{n\vec{k}}(\vec{r}) \qquad (3.28)$$

Hence, it is sufficient to consider $\Psi_{n\vec{k}}(\vec{r})$ and corresponding eigenvalue only in the first 'Brillouin-zone'. Using PBC and Bloch function, one can solve the **Kohn – Sham equation (**equation 3.18) to find out the electronic density $\rho(\vec{r})$ which can be used to describe various electronic properties.

3.1.7 Planewaves and Pseudopotentials

The electron orbitals that are obtained by solving the **Kohn – Sham equation** (equation 3.18) can be represented as an expansion of plane waves (plane waves basis set) in the following way,

$$\varphi_i(\vec{r}) = \sum_{\vec{K}} C_{\vec{K}}^{n,\vec{k}}\, e^{i(\vec{k}+\vec{K}).\vec{r}} \qquad (3.29)$$

Considering the Bloch theorem, the advantages of using planewave basis sets are

- The planewave basis sets are impartial, independent of the type of problem.
- Due to the Bloch theorem, planewave basis sets are a natural choice for the representation of electron orbitals in a periodic system.
- The kinetic energy operator and the potential are diagonal in planewave and real space. So, the transformation between real space and reciprocal space using Fast Fourier Transformation (FFT) provides a large saving in computational cost.

The main drawback of planewave basis set is its inefficiency due to the large number planewaves required to express the atomic wave function accurately near nucleus. The problem is solved by introducing the pseudopotentials [145] which describe the potential associated with ionic core only. The assumption behind the pseudopotentials is that only valence electrons have significant impact on the electronic properties of the system. The pseudopotential represents the contribution only from nucleus and core electrons with the following conditions,

- The wave function associated with the valence electrons remains unchanged outside the core region.
- The pseudo (PS) wave function inside the core region matches correctly at the boundary.
- The PS wave function and its first derivative with respect to position coordinates must be continuous at the boundary, i.e.,

$$\varphi_i^{PS}(\vec{r})\Big|_{r=r_c} = \varphi_i^{AE}(\vec{r})\Big|_{r=r_c} \qquad (3.30)$$

$$\frac{\partial \varphi_i^{PS}(\vec{r})}{\partial r}\Bigg|_{r=r_c} = \frac{\partial \varphi_i^{AE}(\vec{r})}{\partial r}\Bigg|_{r=r_c} \qquad (3.31)$$

where AE stands for the all electron energy.

A schematic drawing of the PS potential (V_{pseudo}) and PS wave function (Ψ_{pseudo}) (drawn in red color) along with the real Coulomb potential (V) and wave function (Ψ) (drawn in blue color) have been shown in figure 3.1. The sketch is taken from ref. 147. There are mismatches between PS and real wave functions and potentials and it is clear that the PS wave function is node less near the core region. So, all the aforesaid conditions must be fulfilled before using any kind of PS potential.

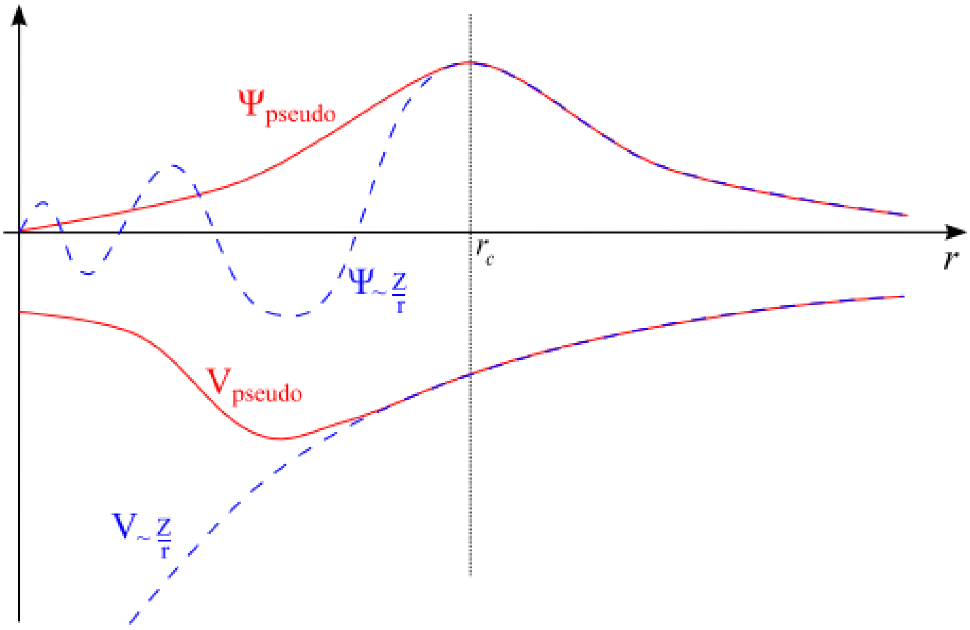

Figure 3.1: A comparison of PS potential (V_{pseudo}) and PS wave function (Ψ_{pseudo}) (drawn in red color) to the real Coulomb potential (V) and wave function (Ψ) (drawn in blue color). The two potentials and wave function match well above certain distance (cutoff radius) from the core of the nucleus.

The typical examples of PS potential are Ultra Soft Pseudo Potential (USPP), Norm Conserving Pseudo Potential (NCPP), Projector Augmented Waves (PAW), Orthogonalised Plane Wave (OPW) etc.

We have used PAW method in our calculations. This is a generalization of linear augmented plane wave method and pseudo-potential, which provides results of greater accuracy and efficiency. It was first proposed by Bloch [148] and was implemented in Vienna Ab-initio Simulation Package (VASP) by Kresse et al [149, 150]. This method works based on the transformation of the PS wave function to the all-electron (AE) wave function. The PS wave function in PAW method consist of three parts as described below,

$$\Psi = \tilde{\Psi} + \sum_{i}^{N} C_i \varphi_i - \sum_{i}^{N} C_i \breve{\varphi}_i \qquad (3.32)$$

where the first part represents the PS wave function, while φ_i and $\check{\varphi}_i$ represent the AE partial wave and AE PS partial wave. Although, the PS wave function agrees well with AE wave function above cutoff radius (r_c), it deviates significantly near the core region. The second and third parts in equation (3.32) are introduced for the correction near the core region (as is clear from figure 3.1). The expression for φ_i and $\check{\varphi}_i$ is obtained from the solution of radial part of Schrodinger equation.

3.2 Computational Approach

We have used VASP code for the computational studies. It is a computer program written in FORTARAN language for the atomic scale modelling using the first principle approach [149 - 151]. A periodic system can be developed in three dimension (3D) using the unit cell information in VASP. The ground state energy and hence electronic properties can be calculated by solving the many-particle Schrodinger equation (equation 3.18) in DFT frame. Some important files required for calculations using VASP are discussed below. For more detailed information, one can go through the VASP user manual.

3.2.1 VASP input files

VASP has four input files for the production runs. These are INCAR, POSCAR, POSCAR and KPOINTS. A brief description of each file is provided below.

INCAR file

INCAR is the central input file of VASP which steers the entire calculation. It contains some important keywords with respective commands. A typical INPUT files for a normal Self Consistent Field (SCF) calculation is discussed here.

SYSTEM = Name of the system for investigation.

PREC = HIGH.

LREAL = AUTO, projection is done in real space, fully automatic optimization of projection operators.

IBRION = 2, a conjugate-gradient algorithm is used to relax the ions into their ground state.

ALGO = FAST, specifies the electronic minimization algorithm. Davidson (IALGO = 38) is used for the initial phase, and then VASP switches to RMM-DIIS (IALGO = 48).

NSW = 100, 100 ionic steps are performed maximally.

ISMEAR = 0, uses Gaussian smearing.

LORBIT = 10, writes DOSCAR and PROCAR file.

GGA = PE, performs GGA calculation with Perdew-Burke-Ernzerhof pseudo-potentials.

SIGMA = 0.01, determines the width of the smearing in eV.

ISPIN = 2, makes spin-polarized calculations possible.

ISIF = 2, force and stress tensor are calculated, ions relaxed, cell shape and volume not changed.

ENCUT = 500, Cut-off energy for plane wave basis set in eV. All plane-waves with a kinetic energy smaller than ENCUT are included in the basis set, got from test.

EDIFFG = -0.02, defines the break condition for the ionic relaxation loop. The relaxation will stop if all the forces are smaller than the |EDIFFG|.

POTIM = 0.5, a scaling constant for the step widths.

ISPIND = 2, performs spin polarized calculations.

EDIFF = 0.001, specifies the global break condition for the electronic SC-loop. The relaxation of the electronic degrees of freedom will be stopped if the total (free) energy change and the band structure energy change ('change of eigen values') between two steps are both smaller than EDIFF.

POSCAR file

POSCAR file contains the structural geometry and ionic positions. The first line in POSCAR file is the command line where the system under investigation is mentioned. The second line indicates the universal scaling factor used to scale the lattice parameters and ionic positions, followed by three lines which are used to express the three lattice parameters. The sixth and seventh lines present the symbol and the number of atomic species present in the system. The eighth line is optional with flags ‘T’ and ‘F’. Flag ‘T’ corresponds to changing of atomic coordinate during the calculation, whereas flag ‘F’ corresponds to their not changing. If the eighth line is not selected dynamics, then by default, all the atomic coordinates are allowed to change during the calculation. Next line confirms the method of expressing the atomic coordinate i.e. whether it is in Cartesian (‘C’) or in direct coordinates (‘D’). Next consecutive lines are associated with respective atomic coordinates consistent with the order mentioned in sixth line.

POTCAR file

POTCAR file contains the list of PS potentials of each atomic species present in the system under investigation. As the electronic properties are highly dependent on valence electrons, one needs to wisely select the PS potentials considering the valency of anion or cation. If the system exhibits more than one atomic species, the POTCAR file should contain all the PS potentials maintaining the same order as in the POSCAR file (sixth line).

KPOINTS

KPOINTS file carries the information of k-point coordinates and weights that will be used for sampling the Brillouin zone. There are various ways such as (a) explicit list of k-point coordinates and their weights (b) by mentioning the beginning and ending points of line segments, (c) automatically generate regular mesh of points using Monkhorst-Pack method etc. for specifying the k-point information in the KPOINTS file. We have used Monkhorst-Pack method to specify the k-points for Brillouin zone sampling.

3.2.2 VASP output files

VASP has three major output files. These are CONTCAR, OUTCAR and OSZICAR. A brief description of each file is provided below.

CONTCAR file

This file of VASP output contains the information of final atomic coordinates of each atom involved in the calculation. After each ionic step and at the end of each job a file CONTCAR is written. It has the identical format as POSCAR file.

OZSICAR file

Information about convergence speed and about the current step is written in OZSICAR file. It is a simplified version of OUTCAR file. It sums up all the necessary information and expresses in one line after each electronic iteration.

OUTCAR file

This is the main output file of VASP. All the output data are included in this file. First, it reads data from input files such as INCAR, POSCAR, POTKAR and KPOINTS. The results of calculations like bond distances, energy of the system, atomic position coordinates, charges, stress tensor, eigen values etc., and other information such as detailed job information, PS potentials used for the calculation etc. are written in this file after each ionic cycle.

3.3 Computational Study of GdFeO$_3$

In this section, we have discussed our computational study on GdFeO$_3$, with VASP package used as a computational tool. The results of structural optimization, magnetic properties and density of states have been discussed including literature survey and computational methodology.

3.3.1 Introduction

Multiferroic materials have attracted a noticeable attention because of the presence of more than one ferroic order [152] and the mutual coupling between electric and magnetic properties [152, 46]. Among single phase multiferroic material, BiFeO$_3$ is a potential candidate which has been studied widely. It shows an anti-ferromagnetic transition below $T_N \sim 643\ K$ [153] and a sufficiently large spontaneous polarization ($\sim 59.4\ \mu C.cm^{-2}$) below Curie temperature $T_C \sim 1100\ K$ [154]. Perovskite BiFeO$_3$ stabilizes in distorted rhombohedral structure with $R3c$ space group [155]. Being a similar magnetic material like BiFeO$_3$, perovskite GdFeO$_3$ with a distorted orthorhombic structure and $T_N \sim 661\ K$, has sparked a substantial curiosity to become a subject of deep research interest [37, 156 - 158].

The GdFeO$_3$ compound contains two different kinds of magnetic elements such as $4f$ based Gd^{3+} ions and $3d$ based Fe^{3+} ions. Due to complex interactions between $4f - 3d$ electrons, it undergoes plural magnetic phase transitions associated with a dramatic change of electrical properties [159]. In addition to anti-ferromagnetic ordering of Fe^{3+} spins, a weak ferromagnetic and ferroelectric [10] behavior is observed at lower temperatures [157, 158]. Apart from spontaneous magnetization and polarization, it shows a magneto-electric phenomenon suitable for a variety of technological applications [160]. The magnetic structure of Fe^{3+} sub-lattice below $T_N \sim 661\ K$ in $GdFeO_3$ can be expressed as $(G_xA_yF_z)$ in Bertaut's notation [161, 162]. However, Gd^{3+} sub-lattice undergoes an anti-ferromagnetic transition below $\sim 2.5\ K$, associated with G_x type magnetic structure [161, 162]. The exchange interaction between these two magnetic sub-lattices results a spontaneous polarization below Gd^{3+} ordering temperature [163]. Hence, the complex magnetic interactions between $4f - 3d$ electrons give rise to interesting phenomena. For example, a spontaneous polarization has been observed in single crystal $DyFeO_3$ below anti-ferromagnetic ordering temperature of Dy^{3+} moments [10]. The magnetic structure of Sm has a great impact on the origin of ferroelectric behavior in $SmFeO_3$ [164, 165]. So, it is clear that the magnetic structure of cations in strongly correlated electron system of ABO_3 structure plays an important role on interesting physical properties which need to be understood more clearly.

Recently, it has been shown using DFT calculations that the magnetic structure associated with Fe^{3+} sub-lattice in $GdFeO_3$ forms G-type anti-ferromagnetic arrangement [166] which does not support the experimental observation of weak ferromagnetism. Although, a large number of experimental studies are available, the computational studies describing the origin of magnetism are extremely meager. So, it is imperative to develop a suitable theoretical model describing spin structure of Fe^{3+} and Gd^{3+} moments. Here, we have studies structural and magnetic properties of $GdFeO_3$ considering collinear and non-collinear spin arrangements of Fe moments.

3.3.2 Computational Methodology

To study the structural stability of $GdFeO_3$, the electronic structural calculations have been performed considering spin-polarized wave based DFT as implemented in VASP [149, 167]. PAW PS potential has been considered to describe the electron-ion interactions [13]. The valence states of Gd, Fe and O have been described considering 18 valence electrons ($5s^2$,

$5p^6$, $4f^7$, $5d^1$, $6s^2$), 8 valence electrons ($3d^7$ $4s^1$) and 6 valence electrons (s^2 p^4) respectively. The calculations were performed considering GGA in PBE parameterization [168]. The sampling over Brillouin zone is carried out using 7×5×7 k-point meshes (140 irreducible k-points in Brillouin zone) generated by Monkhorst-Pack method [169]. A cutoff energy (E_{cut}) of 600 eV for the plane wave basis set is used and the choice of E_{cut} and k-point mesh is sufficient for energy convergence of less than 0.1 meV/atom. The total energy of GdFeO$_3$ unit-cell is optimized with respect to volume, shape and atomic positions as permitted by the space group symmetry of the crystal structure. Also, the structural relaxations are performed to determine unit-cell parameters at high pressures using the conjugate gradient algorithm until the residual forces and stress in the equilibrium geometry were of the order of 0.01 eV/Å and 0.01 GPa, respectively. In the standard mode, VASP performs a fully relativistic calculation for the core-electrons and treats valence electrons in a scalar relativistic approximation. Spin-orbit coupling for the *d* and *f* valence electrons is included by the second-variation method using the scalar-relativistic Eigen functions of the valence states [170, 171].

3.3.3 Structural Optimization

The structural optimization calculations have been performed on GdFeO$_3$ by adopting five different spin configurations associated with Gd^{3+} and Fe^{3+} moments. These are (1) ferromagnetic (FM) structure in which Gd and Fe moments are aligned along same direction (along – c axis), (2) A-type anti-ferromagnetic (A-AFM) in which inter-plane and intra-plane Fe spins are, respectively, anti-ferromagnetically and ferromagnetically coupled, (3) C-type anti-ferromagnetic (C-AFM) in which intra-plane and inter-plane Fe spins are anti-ferromagnetically and ferromagnetically coupled, (4) G-type anti-ferromagnetic (G-AFM) in which both inter-plane and intra-plane Fe spins are anti-ferromagnetically coupled, and (5) canted G-type antiferromagnetic (canted G-AFM) in which both inter-plane and intra-plane

Fe spins are antiferromagnetically coupled with an additional canting in ‘ac’ plane. Gd spins are anti-ferromagnetically coupled along ‘a’ direction in all the AFM configurations. The magnetic structures of the unit cells of FM, A-AFM, C-AFM and canted G-AFM configurations are shown in figure 3.2.

Table 3.1: DFT-GGA calculated equilibrium lattice parameters and volume and energy (in FM, A-AFM, C-AFM, G-AFM and canted G-AFM configurations) are compared with experimental results

Configuration	a (Å)	b (Å)	c (Å)	V (Å^3)	ΔE
FM	5.2992	5.7357	7.5642	229.91	38.68
A-AFM	5.3274	5.6918	7.6165	230.95	35.51
C-AFM	5.3506	5.6661	7.7300	234.35	18.97
G-AFM	5.3477	5.6716	7.7263	234.34	18.95
Canted G-AFM	5.3458	5.6748	7.7068	233.79	0.00
Reported G-AFM	5.399	5.714	7.612	234.83	---
Experimental	5.349,	5.611,	7.669,	230.17,	---

Table – 3.1 compares DFT-GGA calculated equilibrium lattice parameters, and volumes of FM, A-AFM, C-AFM, G-AFM and canted-AFM configurations with existing experimental [172, 173] and previous DFT-GGA calculated [166] values. Table – 3.1 also shows the GGA-PBE calculated energy difference of structures having different magnetic configurations with respect to the most stable canted G-AFM configuration. Based on the calculated energy sequence, canted G-AFM configuration is the most stable one followed by G-AFM, C-AFM, A-AFM and FM configurations. The observation is consistent with the experimental results [159]. The calculated equilibrium lattice parameters in canted G-AFM configuration are in closest agreement with experimental lattice parameters (within 1.2% agreement). However, the calculated equilibrium volume is overestimated by 1.5% compared to experimental values.

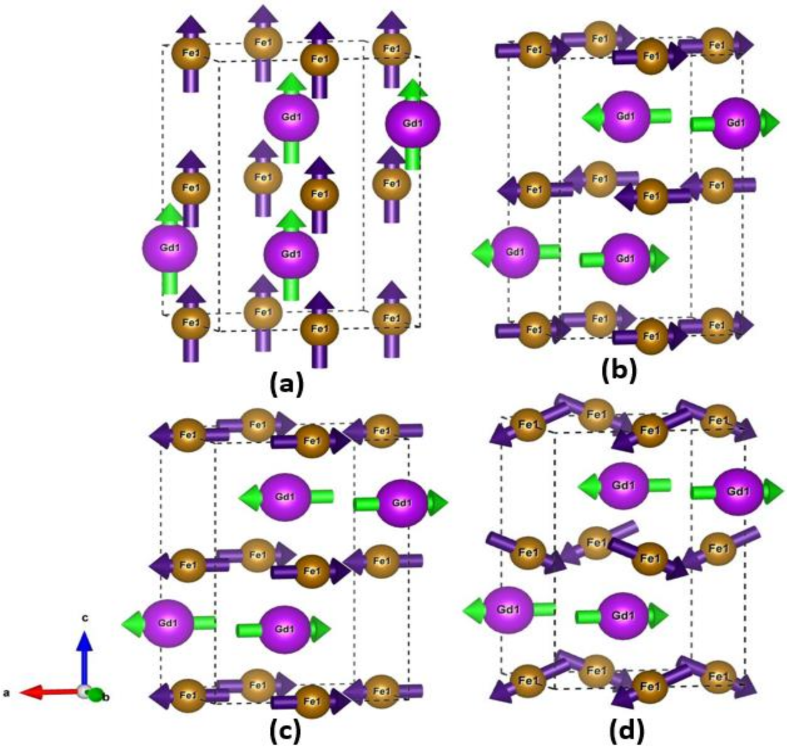

Figure 3.2: The crystal structures with spin orientation of all Gd and Fe atoms for a) ferromagnetic (FM) (all spins of Gd and Fe are oriented in the same direction) b) A-type antiferromagnetic (A-AFM) (inter-plane and intra-plane Fe spins are, respectively, anti-ferromagnetically and ferromagnetically coupled) c) C-type antiferromagnetic (C-AFM) (intra-plane and inter-plane Fe spins are antiferromagnetically and ferromagnetically coupled) and d) canted G-type antiferromagnetic (canted G-AFM; both inter-plane and intra-plane Fe spins are antiferromagnetically coupled) configurations.

The GGA-PBE optimized Wyckoff positions are tabulated in table 3.2. After internal structural optimization, the Wyckoff positions of Gd, Fe, O1 and O2 for canted G-AFM are $(0.01860, 0.06807, 0.25)$, $(0.0, 0.5, 0.0)$, $(0.69685, 0.30278, 0.05463)$ and $(0.10525, 0.46486, 0.25)$ respectively. It is noticed that the x coordinate of Gd is off with the experimental result, but there is a close agreement with the value reported by Coppens et al [174].

Table 3.2: Optimized Wyckoff positions for FM, A-AFM, C-AFM, G-AFM and canted G-AFM configurations are compared with experimental results

Configuration	Atom	Site	x	y	z
FM	Gd	$4c$	0.01970	0.07836	0.25
	Fe	$4b$	0.0	0.50	0.0
	$O1$	$8d$	0.70284	0.31325	0.04904
	$O2$	$4c$	0.09635	0.47743	0.25
A-AFM	Gd	$4c$	0.02000	0.07089	0.25000
	Fe	$4b$	0.00000	0.50000	0.00000
	$O1$	$8d$	0.69884	0.30325	0.05250
	$O2$	$4c$	0.10346	0.46922	0.25
C-AFM	Gd	$4c$	0.01930	0.06840	0.25
	Fe	$4b$	0.0	0.5	0.0
	$O1$	$8d$	0.69748	0.30310	0.05589
	$O2$	$4c$	0.10744	0.46486	0.25
G-AFM	Gd	$4c$	0.01931	0.06909	0.25
	Fe	$4b$	0.0	0.5	0.0
	$O1$	$8d$	0.69696	0.30281	0.05570

	$O2$	$4c$	0.10717	0.46514	0.25
Canted G-AFM	Gd	$4c$	0.01860	0.06807	0.25
	Fe	$4b$	0.0	0.5	0.0
	$O1$	$8d$	0.69685	0.30278	0.05463
	$O2$	$4c$	0.10525	0.46486	0.25
Previous DFT-GGA [166]	Gd	$4c$	0.9911	0.0639	0.250
	Fe	$4b$	0.0000	0.5000	0.0000
	$O1$	$8d$	0.7024	0.3121	0.0488
	$O2$	$4c$	0.0927	0.4726	0.2500
Experimental [172]	Gd	$4c$	0.9844	0.0628	0.25
	Fe	$4b$	0.0	0.5	0.0
	$O1$	$8d$	0.6957	0.3016	0.0506
	$O2$	$4c$	0.1005	0.4672	0.25

3.3.4 Magnetic Properties

To get a better understanding of ground state magnetic properties, we have performed magnetic moment calculation for all AFM spin configurations considering each magnetic element in the unit cell. Our $0\ K$ first principle calculations confirm that canted G-AFM spin configuration is energetically the most favorable state in GdFeO$_3$. Tables (3.3 – 3.6) show DFT-GGA calculated magnetic moments (angular momentum decomposed and total) on Gd and Fe atoms in A-AFM, C-AFM, G-AFM and canted-AFM configurations.

Table 3.3: Magnetic moments in canted G-AFM spin state calculated using DFT-GGA for $GdFeO_3$

Atoms	Direction	Contribution to moment from various electrons				Total (μ_B)
		s	p	d	f	
Gd1	x	0.000	-0.018	0.045	6.805	6.832
Gd2`		0.000	0.018	-0.045	-6.805	-6.832
Gd3		0.000	-0.018	0.045	6.805	6.832
Gd4		0.000	0.018	-0.045	-6.805	-6.832
Fe1	x	0.007	0.005	3.696	0.000	3.708
Fe2		-0.007	-0.005	-3.696	0.000	-3.708
Fe3		-0.007	-0.005	-3.969	0.000	-3.708
Fe4		0.007	0.005	3.696	0.000	3.708
Fe1	y	0.000	0.000	0.029	0.000	0.029
Fe2		0.000	0.000	0.029	0.000	0.029
Fe3		0.000	0.000	-0.029	0.000	-0.029
Fe4		0.000	0.000	-0.029	0.000	-0.029
Fe1	z	0.000	0.000	-0.026	0.000	-0.026
Fe2		0.000	0.000	-0.026	0.000	-0.026

Fe3		0.000	0.000	-0.026	0.000	-0.026
Fe4		0.000	0.000	-0.026	0.000	-0.026

Table 3.4: Magnetic moments in G-AFM spin state calculated using DFT-GGA for $GdFeO_3$

Atoms	Direction	Contribution to moment from various electrons				Total (μ_B)
		s	p	d	f	
Gd1	x	0.000	-0.018	0.043	6.803	6.829
Gd2`		0.000	0.018	-0.047	-6.806	-6.835
Gd3		0.000	0.018	0.043	-6.803	-6.829
Gd4		0.000	-0.018	-0.047	6.806	6.835
Gd1	y	0.000	0.000	0.000	-0.011	-0.011
Gd2`		0.000	0.000	0.000	-0.009	-0.009
Gd3		0.000	0.000	0.000	-0.011	-0.001
Gd4		0.000	0.000	0.000	-0.009	-0.009
Fe1	x	-0.013	-0.013	-3.676	0.000	-3.702
Fe2		0.013	0.013	3.676	0.000	3.702
Fe3		-0.013	-0.013	-3.676	0.000	-3.702

Fe4		0.013	0.013	3.676	0.000	3.702
Fe1	y	0.000	0.000	-0.024	0.000	-0.024
Fe2		0.000	0.001	-0.028	0.000	-0.028
Fe3		0.000	0.000	-0.028	0.000	-0.028
Fe4		0.000	0.001	-0.024	0.000	-0.024

Table 3.5: Magnetic moments in C-AFM spin state calculated using DFT-GGA for GdFeO$_3$

Atoms	Direction	Contribution to moment from various electrons				Total (μ_B)
		s	p	d	f	
Gd1	x	0.002	-0.018	0.043	6.803	6.829
Gd2`		0.000	0.019	-0.047	-6.806	-6.835
Gd3		-0.002	0.018	0.043	-6.803	-6.829
Gd4		0.000	-0.019	0.047	6.806	6.835
Gd1	y	0.000	0.000	0.000	-0.019	-0.019
Gd2`		0.000	0.000	0.000	-0.018	-0.018
Gd3		0.000	0.000	0.000	-0.019	-0.019
Gd4		0.000	0.000	0.000	-0.018	-0.018

Fe1	x	-0.013	-0.013	-3.676	0.000	-3.702
Fe2		0.013	0.013	3.676	0.000	3.702
Fe3		-0.013	-0.013	-3.676	0.000	-3.702
Fe4		0.013	0.013	3.676	0.000	3.702
Fe1	y	0.000	0.000	-0.031	0.000	-0.031
Fe2		0.000	0.001	-0.018	0.000	-0.018
Fe3		0.000	0.000	-0.018	0.000	-0.018
Fe4		0.000	0.001	-0.031	0.000	-0.031

Table 3.6: Magnetic moments in A-AFM spin state calculated using DFT-GGA for GdFeO$_3$

Atoms	Direction	Contribution to moment from various electrons				Total (μ_B)
		s	p	d	f	
Gd1	x	0.001	-0.018	0.045	6.803	6.830
Gd2`		-0.001	0.018	-0.045	-6.803	-6.830
Gd3		0.000	0.018	-0.045	-6.803	-6.830
Gd4		0.000	-0.018	0.045	6.806	6.830
Gd1	y	0.000	0.000	0.000	0.010	0.010

Gd2`		0.000	0.000	0.000	0.010	0.010
Gd3		0.000	0.000	0.000	-0.010	-0.010
Gd4		0.000	0.000	0.000	-0.010	-0.010
Fe1	x	-0.018	-0.021	-3.347	0.000	-3.386
Fe2		-0.017	-0.021	-3.286	0.000	-3.324
Fe3		0.018	0.021	3.346	0.000	3.385
Fe4		0.017	0.021	3.288	0.000	3.325
Fe1	y	0.000	0.000	0.256	0.000	0.256
Fe2		0.000	-0.001	-0.252	0.000	-0.253
Fe3		0.000	0.000	-0.256	0.000	-0.256
Fe4		0.000	0.001	0.253	0.000	0.253

In all the AFM calculations, the magnetic structure associated with Gd^{3+} spin is G_x in Bertaut’s notation, i.e. both intra and inter plane Gd^{3+} moments are anti-ferromagnetically coupled. However, structural optimization with spin-orbit coupling rotates the final magnetic moment in ‘ab’ plane for A-AFM, C-AFM and G-AFM, although the angle of rotation with respect to ‘b’ axis is less than one degree. Surprisingly, in the case of canted G-AFM, no tilting of Gd^{3+} moment along b-axis is found. On the other hand, Fe^{3+} moments have three components viz., anti-ferromagnetic orientation along a-axis and b-axis and a ferromagnetic orientation along negative c-axis (shown in the figure 3.2). Our calculations show a spontaneous magnetic moment of 0.026 μ_B/f.u. associated with Fe atoms which is in concurrence with the experimental observation [173]. The computational results are supported by our experimental observations as discussed in the next chapter (chapter 4). The magnetic structure associated with Fe^{3+} moments in GdFeO$_3$ as suggested by our calculation is (G$_x$, A$_y$, F$_z$) in Bertaut's notation, which is hitherto unreported.

3.3.6 Conclusion

We have used spin polarized PAW method to investigate structural and magnetic properties of orthorhombic GdFeO$_3$. The GGA-PBE approach confirms that canted G-AFM spin configuration of Fe spin is energetically the most favorable state. The optimized lattice parameters and unit-cell volume are in good agreement with experimental observations (chapter 4). The spin arrangements in canted-G-AFM associated with Gd^{3+} and Fe^{3+} ions are G$_x$ and (G$_x$, A$_y$, F$_z$) in Bertaut's notation. Magnetic moment calculations on the canted G-AFM structure reveals a ferromagnetic component of $\sim 0.026\ \mu_B$ per Fe^{3+} ion, aligned along negative 'c' axis. This observation is validated by our experimental studies discussed in the next chapter (chapter 4).

Chapter 4

Structural and Magnetization Studies on Polycrystalline $GdFeO_3$

4.1 Introduction

Emergent technologies are being increasingly forecasted from novel functional materials that exhibit striking phenomena like multiferroism, magnetization reversal, spin switching etc. Rare-earth based orthoferrites $RFeO_3$ (R = rare-earth element) have drawn a noticeable attention because of the presence of such striking phenomena which can be used in possible potential application such as inertia-driven spin magneto-optics, gas sensing, switching, laser induced ultrafast spin reorientation etc. [165, 175 – 180].One of the most interesting phenomena that these materials exhibit is the appearance of spontaneous magnetization and polarization and the mutual controllability of the two order parameters (called magneto-electric coupling) which are in high demand in data storage technology, magneto-optic materials, sensors etc. [37, 10, 163, 181, 182].There are but a very few materials (e.g. $Bi_{0.9-x}Tb_xLa_{0.1}FeO_3$ [183], $GdFeO_3$ [37], $DyFeO_3$ [10]) that show spontaneous polarization as well as magnetization in the same temperature range. Some of these materials exhibit a strong coupling between these two ferroic behaviours. For example, a large magneto-electric coupling is observed in single crystal $DyFeO_3$ below Dy^{3+} ordering temperature due to exchange striction effect between Dy and Fe sub-lattices [10].

Perovskite $GdFeO_3$, a member of $RFeO_3$ orthoferrite family, crystallizes in an orthorhombic structure at room temperature with ‘Pbnm’ space group. Its unit cell accommodates four formula units of $GdFeO_3$,with Gd and Fe atoms occupying 4c and 4b sites respectively. The magnetic structure involves two different sub-lattices, namely, *4f*electron based Gd sub-lattice and *3d* electron based Fe sub-lattice. The Fe^{3+} ions with spin (S) = 5/2 order anti-ferromagnetically below the Neel temperature $T_N(Fe^{3+})$ ~ 650 K. In addition to antiferromagnetic ordering, Fe^{3+} ions possess a weak ferromagnetic moment below $T_N(Fe^{3+})$ due to the anti-symmetric exchange interaction (Dzyaloshinskii-Moriya (DM) interaction) between Fe^{3+}- Fe^{3+} ions [184, 185, 77, 78]. Point symmetry speculates that the plausible spin orientation for Fe^{3+} ions is of (*Gx, Ay, Fz)* type in Bertaut's notation [37], where *Gx, Ay* and *Fz* denotes the spin components along '*a*', '*b*' and '*c*' directions of the orthorhombic unit cell. The Gd moments go through an antiferromagnetic transition below $T_N(Gd^{3+})$ ~ 2.5 K and the magnetic structure associated with Gd^{3+} ions is prognosticated to be *(Gx, Ay)* [37]. However, a magnetic structure of G_x has been observed in crystallographically isostructural $GdCrO_3$ [186] and $GdAlO_3$[187, 188]. Since the exchange interaction between *3d* electrons is much stronger than that between *4f* electrons, the magnetic behaviour of the two sub-lattices show different temperature dependences and the complex magnetic structure of the system results in multiple magnetic phase transitions [189 - 191, 164]. For example, a spin reorientation of Fe^{3+} ions as a function of magnetic field below $T_N(Fe^{3+})$ has been observed in polycrystalline $GdFeO_3$ [188]. In addition, the interaction between these two sub-lattices results in other interesting phenomena like spin flipping of Fe^{3+} ions below$T_N(Gd^{3+})$, in conjunction with spontaneous polarization, reported in $GdFeO_3$ single crystal at 5 kOe [37]. The observation of this spontaneous polarization was explained on the basis of a strong exchange striction between Gd^{3+} and Fe^{3+} sub-lattices. Similarly, the appearance of spontaneous polarization in a single crystal of $DyFeO_3$below Dy ordering (AF) temperature has been explained in terms of exchange striction between Dy^{3+} and Fe^{3+} sub-lattice layers [10]. In case of $SmFeO_3$, however, the connection between the magnetic structure of Sm and the spontaneous polarization is less obvious [164, 165]. So, it is clear that the magnetic structure in this class of compounds plays an important role in multiferroic properties which needs to be understood more clearly.

In this chapter, we have studied the structural and magnetic properties of polycrystalline $GdFeO_3$ and compared our observations with computational studies described in chapter 3. An emphasis has been made to investigate the response of magnetic Fe^{3+} and Gd^{3+} sub-lattices as a function of temperature as well as applied magnetic field.

4.2 Experimental Details

Polycrystalline $GdFeO_3$ has been prepared following the conventional solid-state reaction route. High purity (99.99%) oxide powders of Gd_2O_3 and Fe_2O_3 were used as starting materials. Stoichiometric quantities of precursor oxides were mixed and ground in an agate mortar for 1 hour. A small amount of AR grade acetone was used at the time of mixing to make a homogeneous solid solution. The powder thus ground was calcined at 600˚C for 8 h in air. Pre-sintered powder was again ground for 1 h followed by pelletization under 6 tons pressure. 10 mm diameter circular pallets were then kept in a ‘box furnace’ for sintering at 1000˚C for 24 h in air. After that, sintered pallets were taken out and ground into fine powder for characterization. Compositional homogeneity was analysed by X-Ray diffraction (XRD) technique. Measurements of the magnetic moment as a function of temperature (T) and applied field (H) were performed using the Physical Property Measurement System (M/s. Quantum Design, model: PPMS) and Superconducting Quantum Interference Device (SQUID) magnetometer (M/s. Quantum Design, model MPMS) in the temperature range 1.8 K– 300 K under applied dc magnetic fields up to ± 140 kOe. Zero field cooled (ZFC) and field cooled (FC) processes were used to measure the temperature dependence of magnetization under 50 kOe. In ZFC measurement, the sample was cooled from room temperature down to 1.8 K in zero applied field and magnetization data was collected while the sample was being heated to room temperature in the presence of an external dc field. Thereafter the FC measurements were carried out while cooling the sample to the lowest temperature in the same external field. Isothermal magnetization measurements were carried out over a wide temperature range of 2 K to 300 K.

4.3 Results and Discussion

4.3.1 Structural Analysis

Figure 4.1 shows the XRD pattern of polycrystalline $GdFeO_3$ recorded at room temperature, along with Rietveld-refinement. The XRD pattern has been obtained using Cu-Kα radiation (λ = 1.5406 Å) and Fullprof Suite Program [191] was employed for the refinement of the crystal structural parameters.

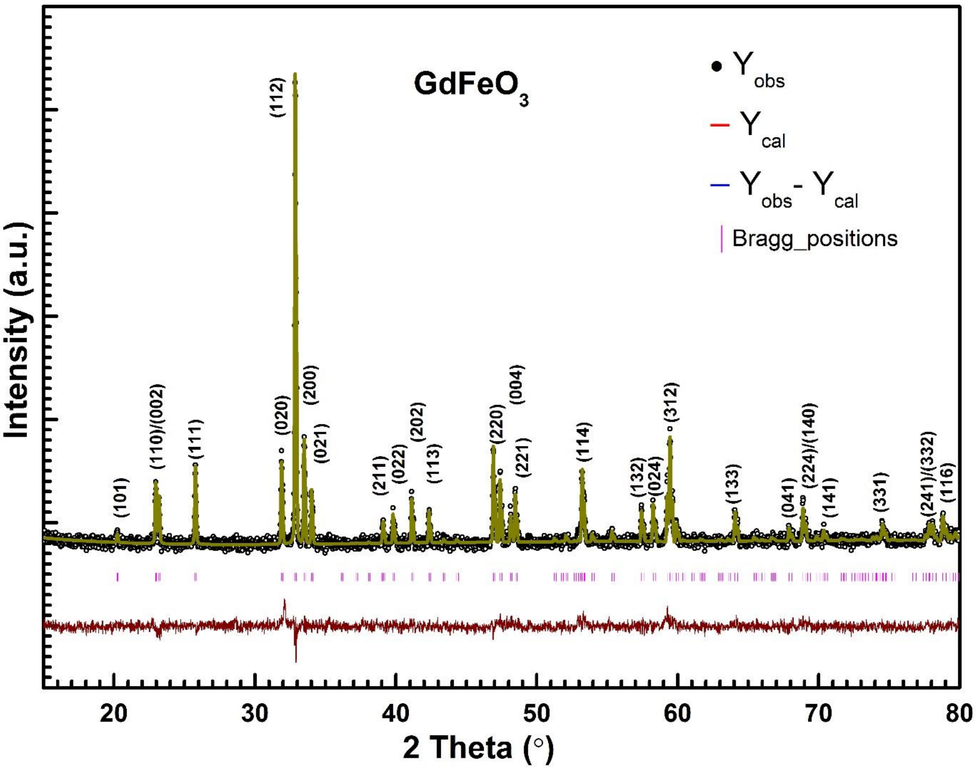

Figure 4.1: Rietveld-refinement of XRD pattern of polycrystalline $GdFeO_3$ recorded at room temperature.

All the observed peaks in XRD pattern correspond to the orthorhombic crystal structure with the '*Pbnm*' space group symmetry [192, 174]. Hence, Rietveld-refinement of XRD data has been carried considering 'Pbnm' space group. The reference input for refinement has been taken from the ICSD database with collection code 23823 [174]. Any traces of starting materials or other bi-products have not been observed within the resolution of XRD measurement. A satisfactory agreement between experimental and calculated intensities has been obtained, with a goodness of fit of 1.14. Refined lattice parameters and unit cell volume have been tabulated in table – 4.1.

Table 4.1: Lattice parameters obtained from Rietveld-refinement of XRD pattern of polycrystalline $GdFeO_3$.

Sample	a (Å)	b (Å)	c (Å)	Volume (Å^3)
Experimental	5.3482 (2)	5.6084 (2)	7.6671 (3)	229.97(1)
Reported [174]	5.3460	5.6160	7.6680	230.22

Figure 4.2 shows a schematic view of the crystal structure of $GdFeO_3$. The illustration was made using VESTA software [193], using the experimental crystallographic information file obtained from Rietveld-refinement.

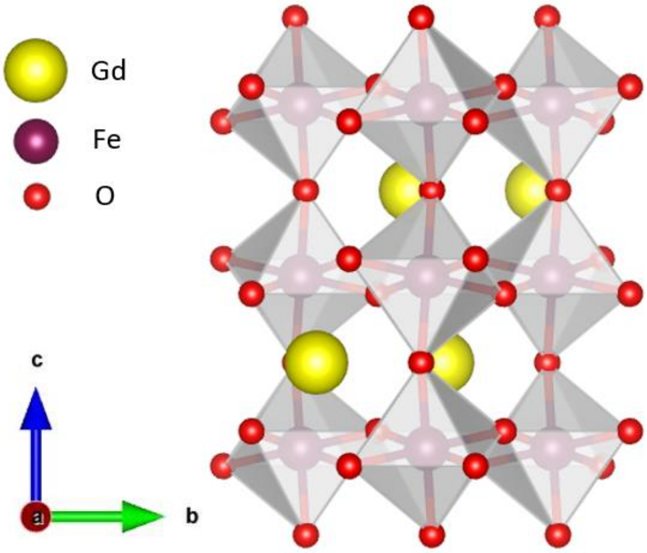

Figure 4.2: Schematic view of the crystal structure of $GdFeO_3$based on Rietveld-refinement.

4.3.2 Magnetization Studies

4.3.2.1 Temperature-dependent Magnetization

To investigate the magnetic properties of polycrystalline $GdFeO_3$, temperature-dependent magnetization (M-T) measurements have been carried out in zero field cooled (ZFC) and field cooled (FC) conditions under dc magnetic fields of 100 Oe, 2 kOe and 50 kOe. In ZFC measurement, we first cooled the sample down to 1.8 K from room temperature and magnetization data was collected while heating the sample under the presence of an external dc field. On the other hand, FC magnetization data was recorded as the sample cools down in the presence of an applied filed.

Figure 4.3 shows the M-T of polycrystalline $GdFeO_3$ measured in ZFC and FC protocols under a dc field of 100 Oe. The temperature dependence of magnetization seen is rather complex and not at all typical to a system of weakly interacting Gd spins with an underlying antiferromagnetic Fe^{3+} sub-lattice.

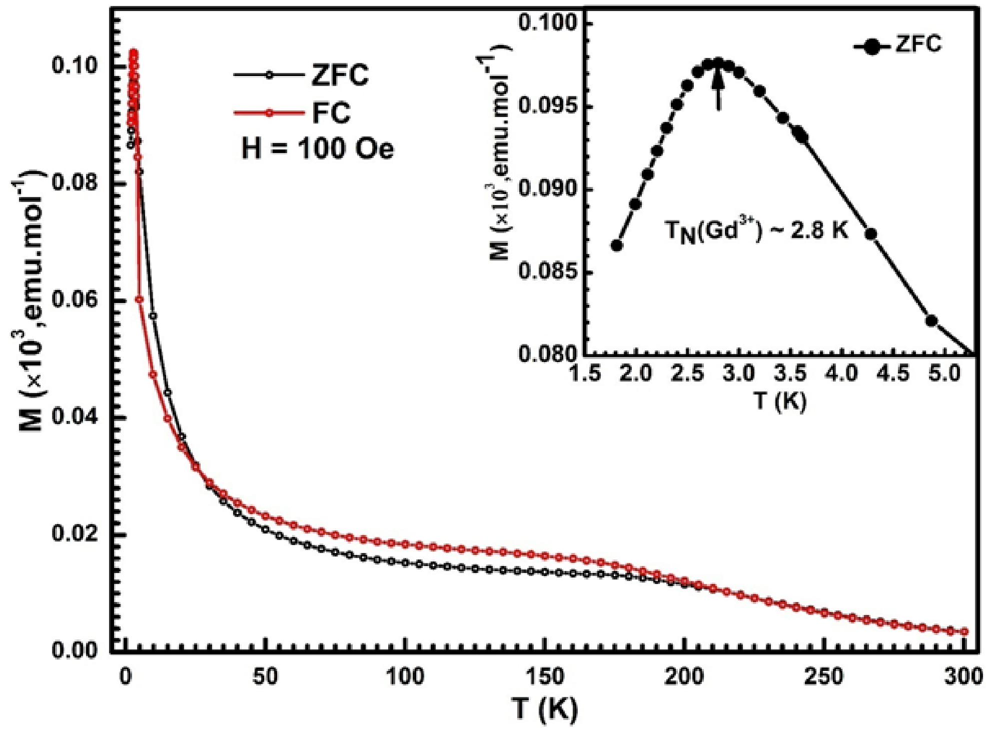

Figure 4.3: Temperature-dependent magnetization (M-T) of polycrystalline $GdFeO_3$ measured in ZFC and FC protocols under a dc field of 100 Oe. Inset shows the enlarge view of ZFC M-T data depicting the anti-ferromagnetic transition associated with Gd^{3+} moments.

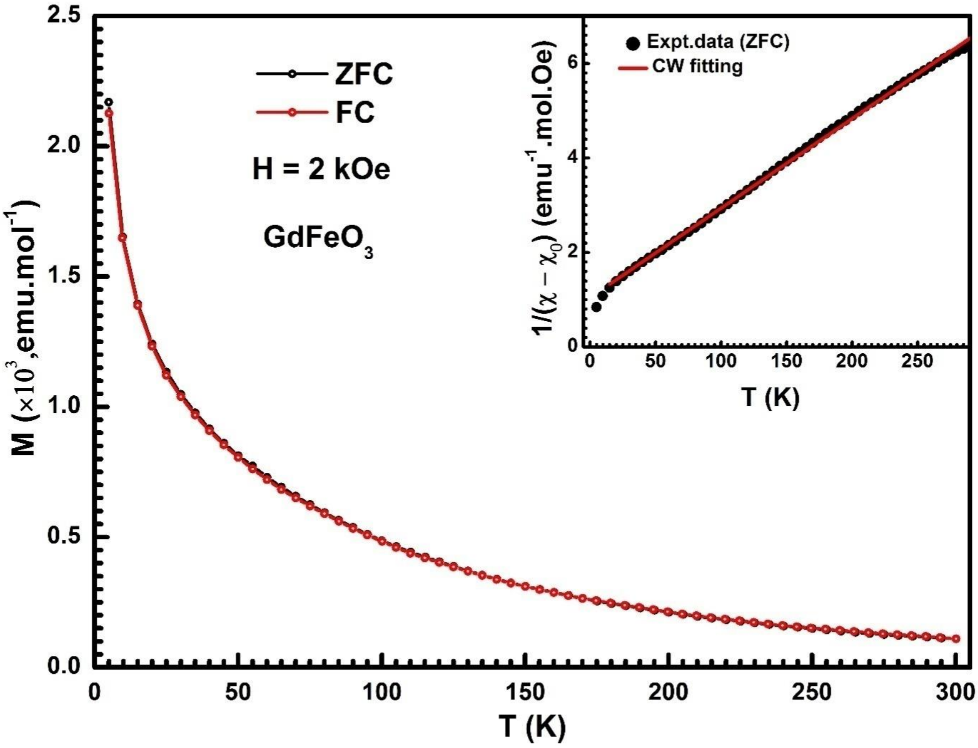

Figure 4.4: Temperature-dependent magnetization (M-T) of polycrystalline $GdFeO_3$ measured in ZFC and FC protocols under a dc field of 2 kOe. Inset shows ZFC '$1/(\chi - \chi_0)$ – T' curve along with Curie-Weiss (CW) fitting.

The magnetization below room temperature tends to increase with decreasing temperature down to 200 K. At this point an anomalous change of slope has been observed in contrast to the expected Curie-Weiss (CW) behaviour. Below 200 K, a bifurcation between the FC and ZFC data has been observed and the increase in magnetization in ZFC seem to follow CW behaviour. However, an attempt to fit this part of the data to modified CW behaviour (equation 4.1) results in a Gd moment far less (7.09 μ_B) than the theoretically expected value (7.94 μ_B). Similar observations have been presented in reference [18],

but no explanation has been offered. For a better understanding of M-T behaviour of the sample, we have carried out further measurements under 2 kOe. Figure 4.4 shows M-T of polycrystalline $GdFeO_3$ measured under a dc field of 2 kOe in ZFC and FC protocols. A clear overlap of ZFC and FC magnetization has been observed. The ZFC magnetization data has been analyzed by fitting with modified Curie-Weiss (CW) law as expressed below,

$$\chi = \chi_0 + \frac{C}{T - \theta cw} \qquad (4.1)$$

where χ_0 is the temperature-independent contribution to susceptibility, C is the slope of fitting called CW constant, and θcw is the CW temperature associated with paramagnetic moment. The effective paramagnetic moment per formula unit has been calculated using the following formula,

$$\mu_{eff} = \sqrt{8C} \qquad (4.2)$$

The CW fitting of $1/\chi$ vs T plot measured under a dc field of 2 kOe is shown as the inset of figure 4.4. The slope of the curve obtained from fitting is 0.0189 which results in an effective moment value of ~ 20 μ_B which is highly unphysical although a satisfactory fitting has been observed. We believe that this anomalous result is related to the temperature dependent behaviour of weak ferromagnetic (WFM) component (due to DM interaction) of Fe^{3+} sub-lattice. Also, one cannot neglect the interaction between Fe^{3+}and Gd^{3+}sub-lattices. Since one could saturate the WFM component at a high field, we have carried out M-T measurement under a field of 50 kOe and the results are shown in figure 4.5. A complete overlap of ZFC and FC magnetization has been observed in the temperature range 10 K to 300 K. CW fitting of FC magnetization data in the temperature range 10 K – 300 K is shown as the inset of figure 4.5, and magnetic parameters obtained from the fit are tabulated in table - 4.2. It is clear from the table that the high field data follows Curie-Weiss behaviour without a significant χ_0.

In the high field case, C value corresponds to the effective paramagnetic moment very close to the expected value (7.94 μ_B) associated with Gd^{3+} spin corresponding to S = 7/2. The temperature-independent part (χ_0) obtained from fitting gives

Table 4.2: Magnetic parameters obtained by fitting susceptibility data of polycrystalline GdFeO$_3$ with Curie-Weiss equation (with and without temperature independent part).

GdFeO$_3$	Field Cooled			Zero-Field Cooled		
	χ_0	μ_{eff}	θcw	χ_0	μ_{eff}	θcw
100 Oe	0.122	7.22	-3.60	0.093	7.09	-3.20
(10 K – 180 K)	---	12.9	-29.5	---	12.2	-27.4
50 KOe	1.12×10^{-4}	7.96	-12.8	9.11×10^{-4}	7.76	-12.4
(10 K – 300 K)	---	7.97	-12.8	---	7.83	-12.7

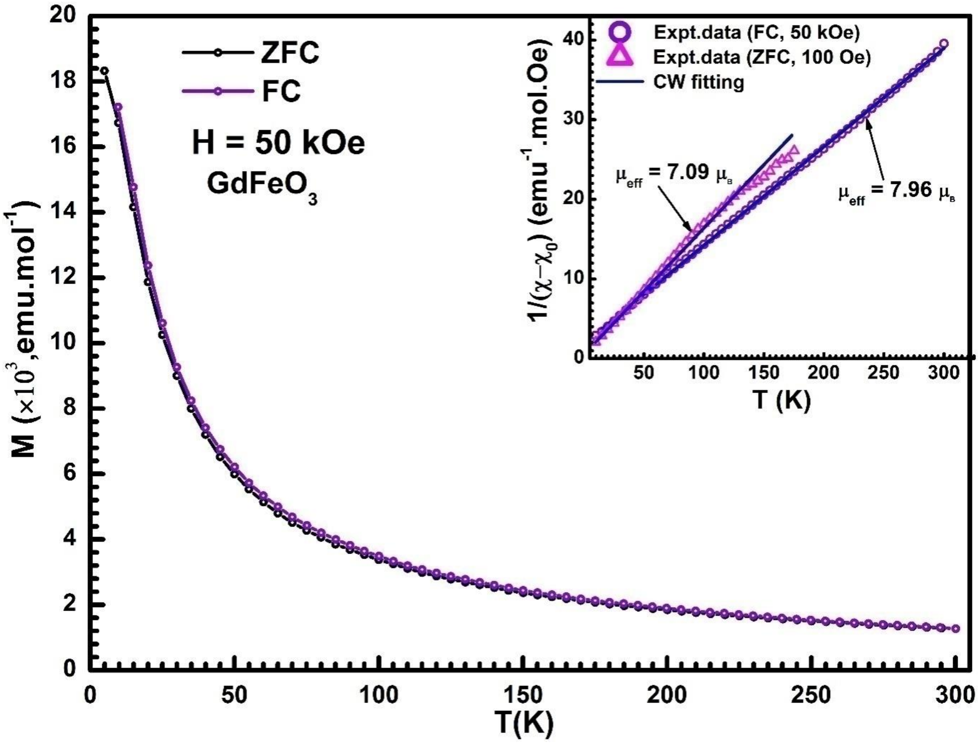

Figure 4.5: Temperature-dependent magnetization (M-T) of polycrystalline GdFeO$_3$ measured in ZFC and FC protocols under a dc field of 50 kOe. Inset shows ZFC ‘1/(χ - χ_0) – T’ curve measured under 100 Oe and FC curve measured under 50 kOe along with Curie-Weiss (CW) fitting.

an equivalent moment of 0.022 μ_B/f.u which is very small compared to full moment of Fe^{3+} (S = 5/2) ions. Assuming that χ_0 ~ 0.022 μ_B/f.u corresponds to saturated WFM component of Fe^{3+} moments, it should be noted that a similar ferromagnetic component of 0.026 μ_B/f.u associated with Fe^{3+} moments has been obtained in DFT calculation discussed in the previous chapter (chapter 3). In the low field case, a large χ_0 is associated with an unreasonable value of μ_{eff}, while the fit without temperature independent part results in unphysical values (second row in 100 Oe category). So, it is conclusive from temperature-dependent magnetization that low field measurements lead to unphysical values of fitting parameters, presumably on account of temperature dependence of competing magnetic interactions, while measurements carried out at a field high enough to saturate WFM component (H = 50 kOe) result in expected values of μ_{eff} and χ_0, which are also validated by our computational studies.

Inset of figure 4.3 shows an enlarged view of M-T curve in the low temperature region (measured under a dc field of 100 Oe). The peak in M-T at ~ 2.8 K corresponds to a magnetic order associated with Gd^{3+} sub-lattice. It's a transition from paramagnetic to antiferromagnetic state, as supported by NMR study [194].

4.3.2.2 Field-dependent Magnetization

The isothermal magnetization (M-H) measured at 2 K is shown in figure 4.6. An increase in M with increasing applied field has been observed up to 4.5 kOe, beyond which it saturates at 3.82×10^4 emu/mol (~ 6.84 μ_B at 140 kOe). This saturation in M observed at 2 K is close to the saturation magnetization of Gd^{3+} corresponding to spin value of 7/2.At 2 K and under zero applied field,Gd^{3+}sublattice is expected to be in AF state [194]. However, the observed behaviour corresponds to that of a ferromagnet, thus indicating that the Gd sub-lattice undergoes a metamagnetic transition at a very small field. This is supported by the slope of virgin magnetization near zero field (see inset (a) of figure – 4.6) and the observation of very small hysteresis in the M-H curve as shown in the insets (b)&(c) of the same figure. A saturation magnetization of ~ 7 μ_B per Gd atom at 2 K has also been reported in single crystal

$GdFeO_3$ [37], which has been explained on the basis of Gd^{3+} spin flop occurring simultaneously with Fe^{3+} spin reorientation [37]. The inset (a) of figure 4.6 shows another hysteresis near zero-field region, originating from WFM component of Fe^{3+} moments. It is known that Fe^{3+} moments in $GdFeO_3$ undergo an anti-ferromagnetic transition below $T_N(Fe^{3+})$ ~ 650 K with a canted ferromagnetic component [184].

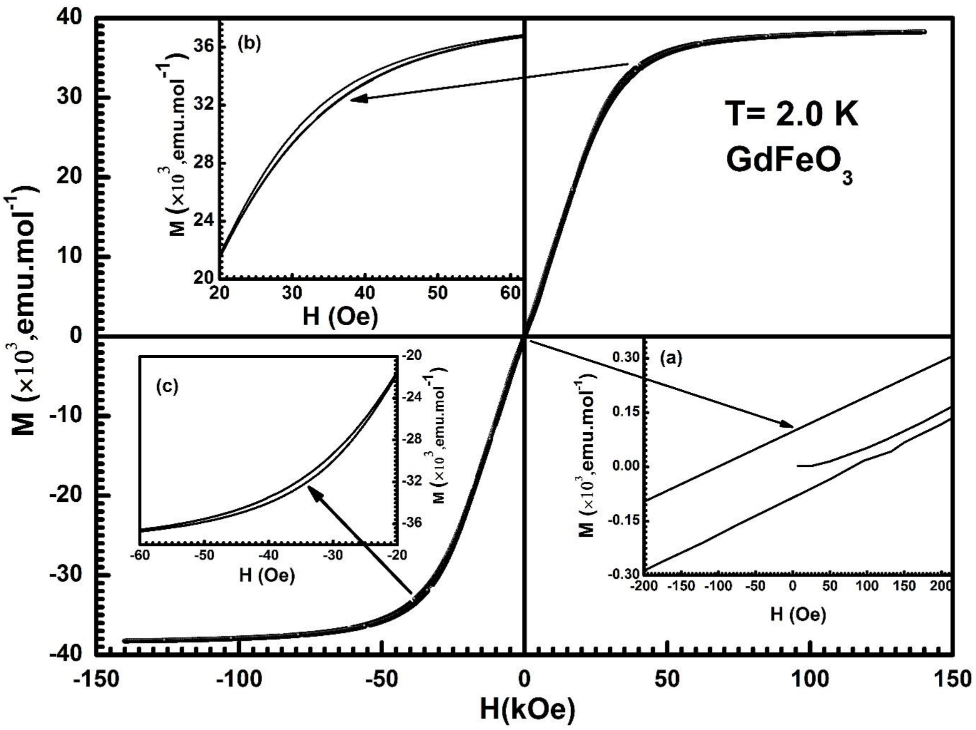

Figure 4.6: Field-dependent magnetization (M-H) of polycrystalline $GdFeO_3$ measured at 2 K. Insets shows an enlarged view of regions indicated by the arrow marks.

To study the magnetic hysteresis at near zero-field as well as large field region, the isothermal M-H has been measured at various temperatures below and above of $T_N(Gd^{3+})$ ~ 2.8 K. Figure 4.7 shows the isothermal M-H curves measured at 2.5 K, 3.0 K, 3.5 K, and 4.5 K for fields up to ± 140 kOe. An increase in M with increase in applied field has been observed for all the measurements up to 4.5 kOe, beyond which it nearly saturates, similar to that observed at 2 K (see figure 4.6). An identical behaviour of M-H has been observed as it is clear from Figure 4.7. The overall magnetic behaviour of bulk $GdFeO_3$ can be described in terms of contributions from two magnetic sub-lattices, (1) anti-ferromagnetically aligned canted Fe^{3+} moments due to Fe^{3+} - O - Fe^{3+}superexchange interaction below $T_N(Fe^{3+})$ ~ 650 K, and (2) the paramagnetic contribution from localized Gd^{3+} moments above $T_N(Gd^{3+})$ ~ 2.5 K. The appearance of zero-field moment and a small hysteresis in all the M-H measurements indicate the presence of a WFM contribution as shown in the insets of figure 4.7, possibly due to anti-symmetric exchange interaction (DM interaction) between Fe^{3+} - Fe^{3+} moments. To understand the origin of hysteresis near zero-field region, further M-H measurements have been carried out at 12 K, 17 K, 22 K, and 300 K and the results are shown in figure 4.8.A small hysteresis along with remnant magnetization (M_r) near-zero field region can be seen in the inset of the figure. The M_r values estimated at various temperatures have been tabulated in table – 4.3 and it can be seen that they remain around 0.020 μ_B per Fe-atom in the entire temperature range investigated. Further,

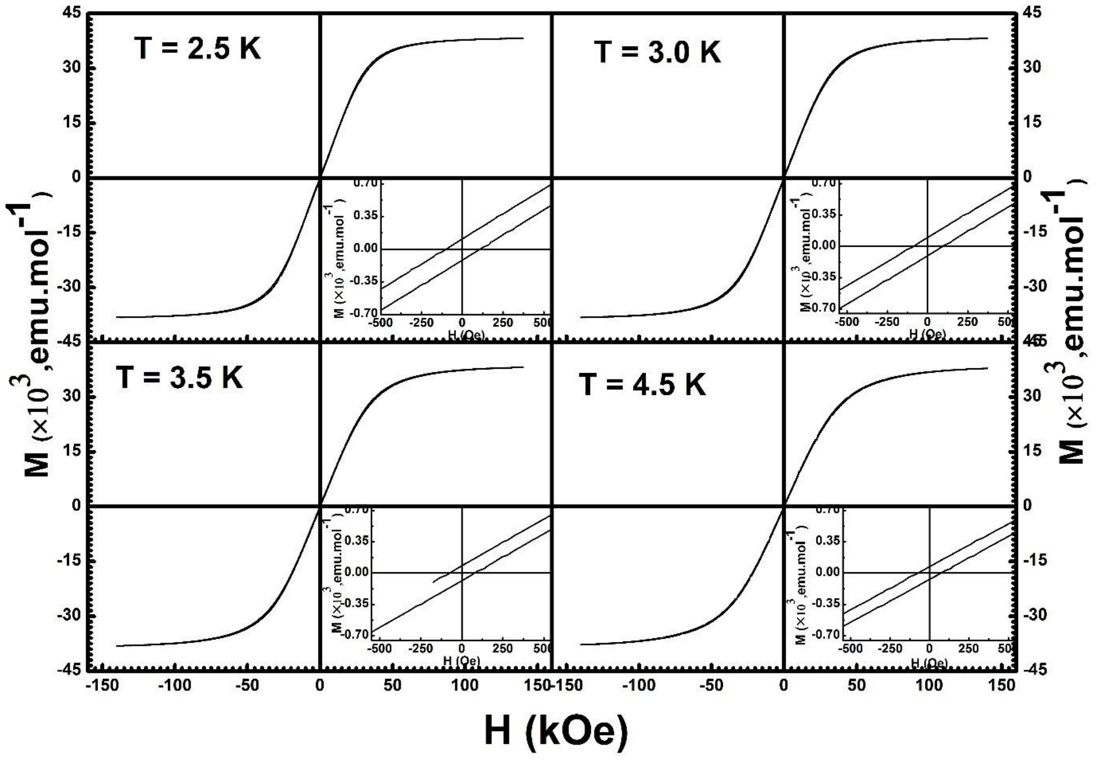

Figure 4.7: Field-dependent magnetization (M-H) of polycrystalline $GdFeO_3$ measured at 2.5 K, 3.0 K, 3.5 K and 4.5 K. Insets show an enlarged view near zero-field region.

our computational studies suggest that the magnetic structure associated Fe^{3+} moment is (G_x, A_y, F_z) (see chapter 3) with a small ferromagnetic component of 0.026 μ_B/f.u.

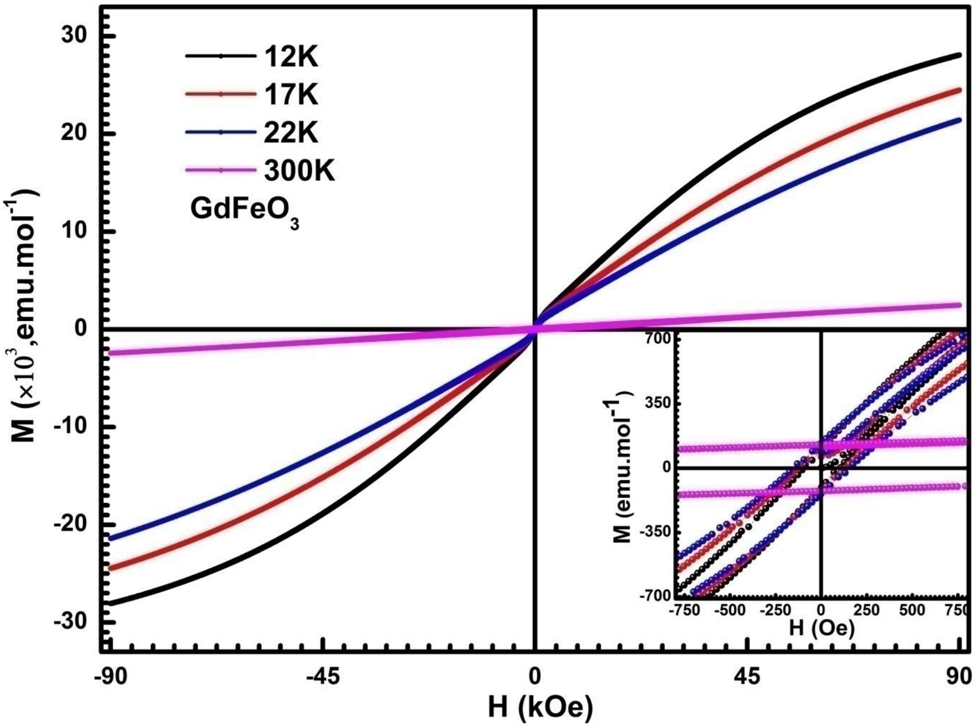

Figure 4.8: Field-dependent magnetization (M-H) of polycrystalline $GdFeO_3$sample measured against the applied field (H) at temperatures 12, 17, 22 K and 300 K. Inset shows the magnified view of hysteresis curves near zero-field region.

along negative ‘c’ axis which is very close to our experimentally observed value. A similar observation has been made in iso-structural single crystal of $GdCrO_3$ [186] and $GdAlO_3$ [187]. Thus, we have shown that a zero-field moment of 0.022 μ_B / Fe-atom observed at room temperature arises due to canted Fe^{3+}moments. Such a small value implies a canting angle of α= 3.73 mrad for those moments, with normal to the applied field, if the moment associated with $Fe^{3+}$is taken to be 5.9 μ_B. Also, an identical value of canting angle (α) has been observed in other rare earth orthoferrites [195, 196].

We have not noted any opening up of loops in the high-field region of M-H curves measured at 12 K, 17 K, 22 K, and 300 K, as evident from figure 4.8,

Table 4.3: Remnant magnetization (M_r)observed in M-H curves measured at different temperatures for polycrystalline $GdFeO_3$.

Temperature (K)	Remnant Moment (μ_B)/Fe atom
2	0.018
2.5	0.020
3	0.018
3.5	0.015
4.5	0.019
12	0.018
17	0.022
22	0.025
300	0.022

while such loops have been observed at temperatures below 5 K as shown in figure 4.9. For a clear view of loops in higher-field region, the first quadrant of M-H data at 2.5 K, 3.0 K, 3.5 K, 4.5 K and 12 K is selectively shown in figure 4.9. This phenomenon is attributed to the metamagnetic transition of Gd^{3+} moments from antiferromagnetic to ferromagnetic state. The extent of opening is maximum at the lowest temperature (i.e. at 2 K) and decreases with increasing temperature, finally vanishing by 12 K. Since temperature-dependent magnetization (see figure 4.3) shows an anti-ferromagnetic transition associated with Gd^{3+} moments at $T_N(Gd^{3+}) \sim 2.8$ K, Gd^{3+} moments are expected to behave paramagnetically above that temperature.

However, the presence of hysteresis at higher-field region of M-H curves measured at 3.0 K, 3.5 K, and 4.5 K suggests that the short range anti-ferromagnetic correlations between Gd^{3+} moments do not disappear right at $T_N(Gd^{3+})$, although the long range anti-ferromagnetic interaction vanishes. The presence of hysteresis near zero-field region at all temperatures and the absence of high-field loop at temperatures > 5 K provides

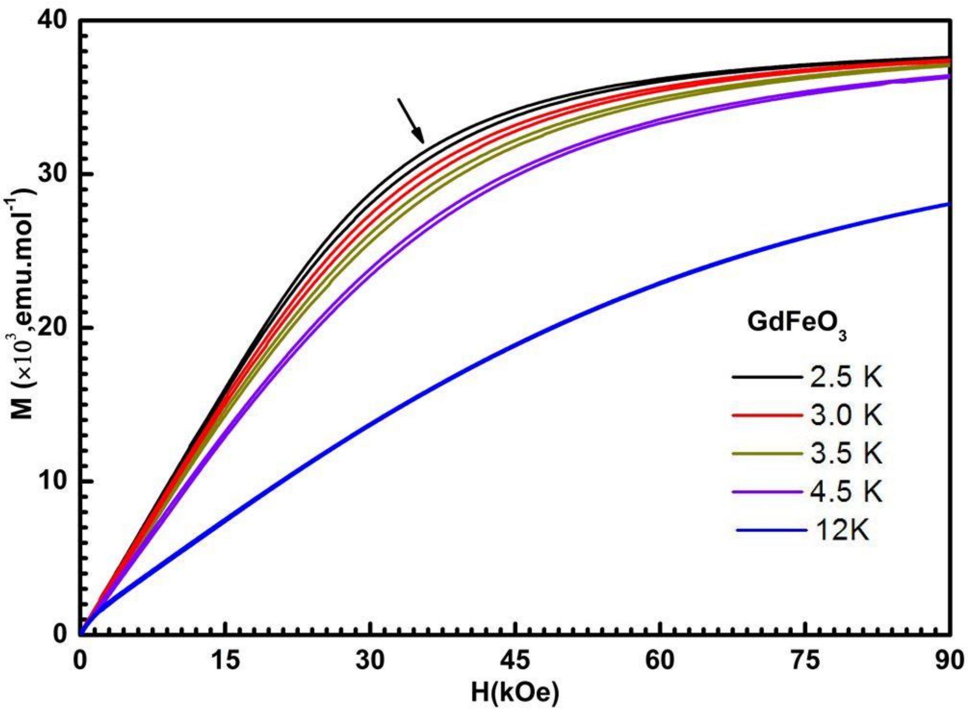

Figure 4.9: Loop opening at high-field region of M-H curves (as shown by arrow mark) measured at 2.5 K,3.0 K, 3.5 K, 4.5 K and 12.0 K for polycrystalline GdFeO$_3$.

a solid evidence that the former is associated with Fe^{3+} moments while the spin-flop metamagnetic transition to ferromagnetic state is linked to Gd^{3+} moments. Assuming that, the WFM moment due to canted Fe^{3+} sub-lattice saturates at sufficiently higher field (> 20 kOe), the virgin M-H curves measured at different temperatures above T$_N$(Gd^{3+}) ~ 2.8 K have been fitted with Brillouin (BJ) function [146] for paramagnetic materials in addition to a constant contribution due to Fe^{3+} moments as described by the following equation,

$$M = M_{Fe} + M_s\left[\frac{2J+1}{2J}Coth\left(\frac{2J+1}{2J}x\right) - \frac{1}{2J}Coth\left(\frac{x}{2J}\right)\right] \qquad (4.3)$$

where M_{Fe} is the contribution to the magnetization due to canted iron sub-lattice, $x = gJ\mu_B H\ /\ K_B T$ and $M_s = NgJ\mu_B$ is the saturation magnetization due to paramagnetic Gd^{3+} moments. Further,$K_B$is the Boltzmann constant, N is the number of Gd^{3+}

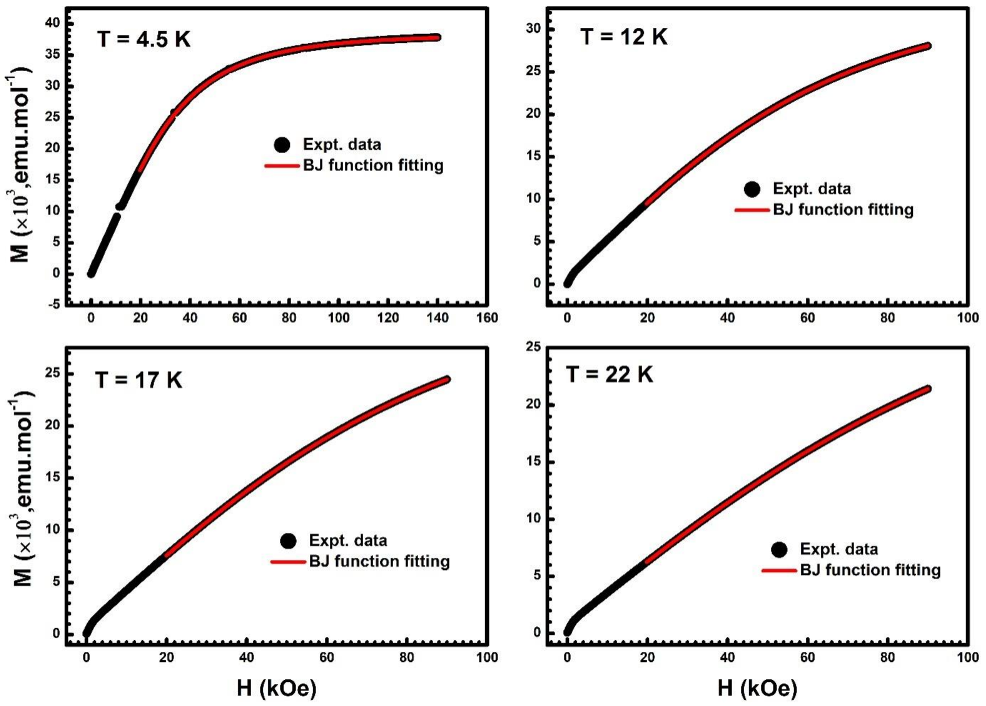

Figure 4.10: Brillouin function (BJ) fitting to virgin magnetization curves measured at 4.5, 12, 17 and 22 K for polycrystalline $GdFeO_3$.

moments, J is the angular momentum quantum number and g is the Lande factor which is assumed to be 2 (spin contribution alone). Figure 4.10 shows the virgin magnetization measured at 4.5 K, 12 K, 17 K, and 22 K along with fitting to BJ function (see equation 4.3). The shape of virgin magnetization curve depends on angular momentum quantum number J and the saturation magnetization on N and J. The magnetic parameters obtained from BJ function fitting are tabulated in table – 4.4.

Table – 4.4 shows that N and J values obtained at 4.5 K are 1.38×10^{24} and 1.51, which are far from the expected values of 6.023×10^{23} and 3.5 for Gd^{3+} moments. However, these values increase with increasing temperature to 6.02×10^{23} and 3.48 at 300 K, close to the expected values. Also, obtained saturation magnetization obtained (~ 6.96 μ_B) is very close to 7.0 μ_B expected for Gd^{3+} (S = 7/2).

Table 4.4: Parameters obtained from Brillouin function (BJ) fitting of virgin magnetization curves measured at 4.5, 12 K, 17 K and 22 K for polycrystalline $GdFeO_3$.

T (K)	N (per mol)	J	M_s(μB)	M_{Fe}(μB)
4.5	1.38×10^{24}	1.51	6.84	0.024
12	7.61×10^{23}	2.69	6.32	0.021
17	6.87×10^{23}	2.76	6.20	0.023
22	6.31×10^{23}	2.90	6.38	0.022
300	6.02×10^{23}	3.48	6.96	0.023

Finally, the contribution to magnetization from canted Fe^{3+} moments (M_{Fe}) remains nearly constant (~ 0.022 μ_B per Fe ion) which is well supported by our computational results as discussed in chapter 3.

4.4 Conclusion

Single-phase polycrystalline $GdFeO_3$ has been prepared following conventional solid-state reaction method. Magnetization measurements as a function of temperature measured under a dc field of 100 Oe show a complex behaviour along with an anti-ferromagnetic transition at ~ 2.8 K associated with Gd^{3+} sub-lattice. It has been observed that M-T measured under small magnetic fields (100 Oe & 2 kOe) results in unphysical values of CW parameters probably due to temperature dependence of competing magnetic interactions. Modified CW fitting of FC M-T data measured under a dc field of 50 kOe results in an effective paramagnetic moment of 7.96 μ_B/f.u. which is very close to expected spin only moment of Gd^{3+} (S = 7/2). The temperature independent part of magnetic susceptibility, χ_0~ 0.022μ_B/f.u., obtained from modified CW fitting is in corroboration with the computational results (component of Fe^{3+} moment along – ‘c ‘axis is 0.026 μ_B) as well as the remnant magnetization observed in M-H curves. A small hysteresis has been observed near zero-field region of M-H curves measured at different temperatures provides a solid evidence that this phenomenon is associated with canted Fe^{3+} sub-lattice. The appearance of a loop at higher-field region in field-dependent magnetization measurements performed below $T_N(Gd^{3+})$ at 2 K confirms spin-flop type metamagnetic transition to ferromagnetic state of Gd^{3+} sub-lattices from anti-ferromagnetic alignment. The presence of such a loop even above $T_N(Gd^{3+})$ could be ascribed to short range anti-ferromagnetic interaction between Gd^{3+} moments at temperatures slightly above the ordering temperature. The width of the loop decreases with increasing temperature and vanishes entirely by ~ 12 K provides a solid evidence of metamagnetic transition and thus evades the instrumental artefact.

The following chapter describes our observation of Mn-valence fluctuation and magnetic frustration in $YMnO_3$.

Chapter 5

Study of Magnetic Frustration in Polycrystalline Y(Mn,Ga)O_3

5.1 Introduction

Rare-earth manganese oxides ($RMnO_3$) belong to a class of multiferroic materials that demonstrate several interesting physical phenomena because of the coupling between magnetic and electric order parameters. Depending on the ionic radius of rare-earth element (R), the crystal structure of $RMnO_3$ stabilizes in two variants. In case of larger ionic radius of R atom (La – Dy in lanthanide series), it stabilizes in distorted orthorhombic perovskite structure, whereas for comparatively smaller ionic radius of R (Ho – Lu and Y), it stabilizes as a hexagonal phase [197 - 199].

At room temperature, $YMnO_3$ has a hexagonal structure with non-centrosymmetric '$P6_3cm$' space group [72, 200]. The unit cell of $YMnO_3$ accommodates six Mn atoms arranged in triangular geometry in the z = 0 and z = ½ planes: placed along the axes **a**, **b** and **-(a+b)** in the z = 0 plane and along -**a**, -**b** and (**a**+**b**) directions in the z = ½ plane. Each Mn atom sits at the centre of corner sharing MnO_5 polyhedron which contains two apical O atoms along '**c**' axis and three basal O atoms in the 'ab' plane. Mn atoms occupy equivalent positions in triangular geometry in the unit cell of $YMnO_3$, as shown in Figure 5.1(a).

Hexagonal $YMnO_3$ undergoes an antiferromagnetic transition at T_N ~ 72 K and a ferroelectric transition at T_E ~ 913 K [38, 201, 202]. Below the transition temperature (T_N), $YMnO_3$ exhibits an antiferromagnetic alignment of Mn^{3+} moments in two dimensions (2D), i.e. in the 'ab' plane, and exhibits Curie-Weiss (CW) behaviour in the temperature region far above of T_N. The CW constant (θ_{cw}) obtained for this compound vide equation – 1 varies from – 400 K to – 575 K, as reported by different studies [38, 202 - 204]. In addition, the antiferromagnetic interaction between Mn^{3+} moments in triangular geometry [201] induces a magnetic frustration in $YMnO_3$ [205, 206]. A measure of magnetic frustration is described by the frustration factor, $f = \theta_{cw}/T_N$, introduced by A. P. Ramirez in 1994. The value of f is reported to vary from 5.7 to 7.9 [38, 207]. A plausible magnetic structure below T_N associated with Mn^{3+} obtained from neutron diffraction studies [201, 208] is presented in Figure 5.1(b).

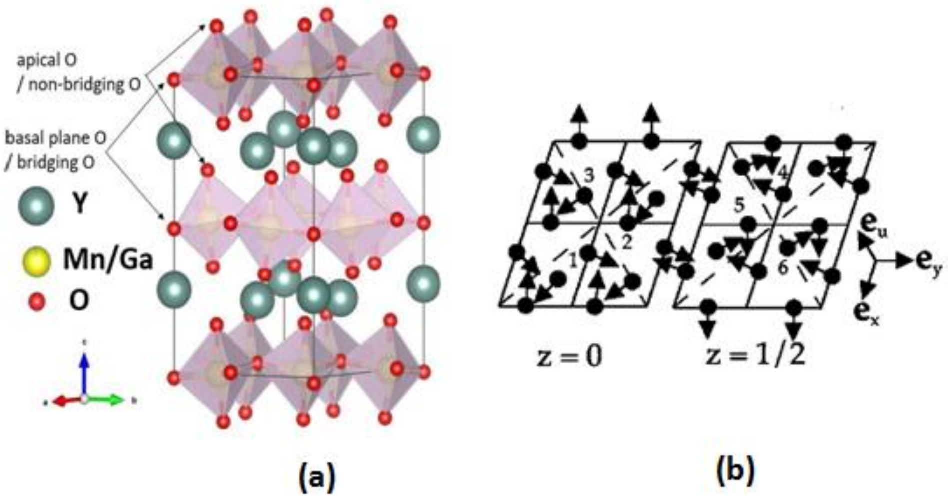

Figure 5.1: (a) A schematic of atomic positions in hexagonal crystal structure of $YMn_{1-x}Ga_xO_3$ (space group P6-$_3$cm) obtained from Rietveld-refinement. Mn / Ga are at the centres of trigonal-bipyramids, (b) schematic representation of magnetic structure associated with Mn^{3+} in $YMnO_3$ below 75 K.

The crystal structure and magnetic properties of $YMnO_3$, modified by substitution at Y and Mn sites with both magnetic and non-magnetic ions, have been studied by several research groups [207, 209 – 217]. A nominal effect on magnetic frustration has been noted in $Y_{1-x}Lu_xMnO_3$ $(0 \leq x \leq 1)$ system [202], whereas a significant effect has been observed in $Y_{1-x}Er_xMnO_3$ $(0 \leq x \leq 1)$ [203]. However, a spin glass like behaviour has been observed in divalent ion substitution at Y-site in $YMnO_3$ compound [211, 212]. On the other hand, a partial substitution at Mn-site has been found to impact magnetic frustration in $YMnO_3$ more strongly. A weak ferromagnetism and decreased magnetic frustration have been observed by Xiao Li-Xia et al in $Y(Mn,Cu)O_3$ system [213], whereas Jeuvrey et al [214] observed that frustration factor remains almost invariant in $YMn_{1-x}Cu_xO_3$ ($x < 0.15$). Substitution by Fe at Mn-site [215] results in a systematic variation of frustration factor in $YMnO_3$, whereas Neekita et al [207] have reported no variation of frustration factor in 10% Fe substitution at Mn site. As an example of non-magnetic ions substitution, Ti modified $YMnO_3$ [217] shows a decrease of both CW temperature and frustration factor, whereas Ga substitution results in a decrease of both CW temperature and antiferromagnetic transition temperature with an increase in frustration factor [207]. Nugroho et al however observed a relatively gradual decrease of θ_{cw} than noted in ref. 13. In this case, the frustration factor is found to increase mainly due to decreasing T_N.

The effective paramagnetic moment (μ_{eff}) values obtained by CW fitting for unsubstituted $YMnO_3$ are reported to vary in the range of $5.0\mu_B$ to $5.3\ \mu_B$ which is larger than the expected theoretical value of $4.90\ \mu_B$ corresponding to Mn^{3+}. However, in substituted $YMnO_3$compound, if the substituted elements exhibit a magnetic moment, μ_{eff} corresponds to the weighted average of the element and Mn^{3+} ion moments. In cases where the substituted elements do not exhibit a magnetic moment, μ_{eff} decreases according to the concentration of substitution. Although, Ga doping at Mn-site in $YMnO_3$ decreases μ_{eff}, the reduction is possibly connected to the change in Mn valency, as in the case of Co substitution at Mn-site [38]. The μ_{eff} in $YMnO_3$, is expected to depend strongly on Mn valency which in turn depends on the oxygen content in the sample. X-ray photoemission spectroscopy (XPS) studies on $YMnO_3$ show Mn^{3+} valence state [218] for Mn in most cases and a mixed valence state of Mn^{3+} and Mn^{4+} in some cases [219]. However, systematic studies involving $YMnO_3$ system to correlate effective Mn valency with magnetic moment are lacking.

In this chapter, we present structural and magnetic properties of $YMn_{1-x}Ga_xO_3$ (x = 0.0, 0.03 and 0.06). Our results of XPS and magnetization studies establish a correlation between Mn valency and effective paramagnetic moment.

5.2 Experimental details

Polycrystalline samples of $YMn_{1-x}Ga_xO_3$ (x = 0.0, 0.03 and 0.06) have been prepared following the conventional solid-state reaction method. High purity (99.99 %) Y_2O_3, Ga_2O_3 and MnO_2 have been used as starting materials. Their stoichiometric amounts have been weighed and mixed using an agate mortar and pestle, in a medium of AR grade Acetone, in order to achieve high homogeneity. Before weighing, all the starting materials were heated up to 473 K to get rid of moisture. Mixed powders were heated up to 1373 K with a rate of 3° C/min, and held at that temperature for 13 hours. The process of grinding, mixing and heating was repeated one more time. Thereafter, the powders were pelletized and sintered at 1573 K for 13 hours. The samples have been characterized using powder X-ray Diffraction (XRD) (Rigaku Miniflex-600, Cu K_α) in 2θ range of 10° to 80°. The oxidation states of Y, Mn and Ga have been measured by X-ray Photoemission Spectroscopy (XPS) using MgK_α (1253.6 eV) X-ray source and a DESA-150 electron analyzer (M/s. Staib Instruments, Germany). The binding energy scale has been calibrated using C-1s line of 284.8 eV. The analyzer was operated at 40 eV pass energy and pressure in the chamber during analysis was ~ 7×10^{-9} Torr. The XPS spectra have been analyzed using XPSPEAK41 software. Temperature dependence of magnetization has been measured in the temperature range 5 K - 300 K using a Superconducting Quantum Interference Device (SQUID) based magnetometer (M/s. Quantum Design, model MPMS) and Raman Spectra have been recorded using Jobin-Yvon HR-800 Evolution spectrometer with 532 nm laser and 600 rulings/mm grating, which gives a resolution of 1.5 cm^{-1} per pixel.

5.3 Results and discussions

5.3.1 X-ray diffraction and Rietveld-refinement

Figure 5.2 represents the XRD pattern of polycrystalline $YMn_{1-x}Ga_xO_3$ (x = 0, 0.03, 0.06) in the 2θ range of 15° to 70°, recorded at room temperature. Preliminary investigation reveals that all the peaks observed in XRD pattern are associated with the hexagonal crystal structure with ‘$P6_3cm$’ space group symmetry. Any impurity phases or starting precursors e.g. MnO_2, Y_2O_3 or Ga_2O_3 have not been observed within the resolution of X-ray diffractometer. Hence, we have performed Rietveld-refinement of XRD data using Fullprof [111] software considering space group ‘$P6_3cm$’. The initial structural parameters for refinement have been taken from ICSD database [220]. A very good agreement between observed and calculated intensities has been observed,

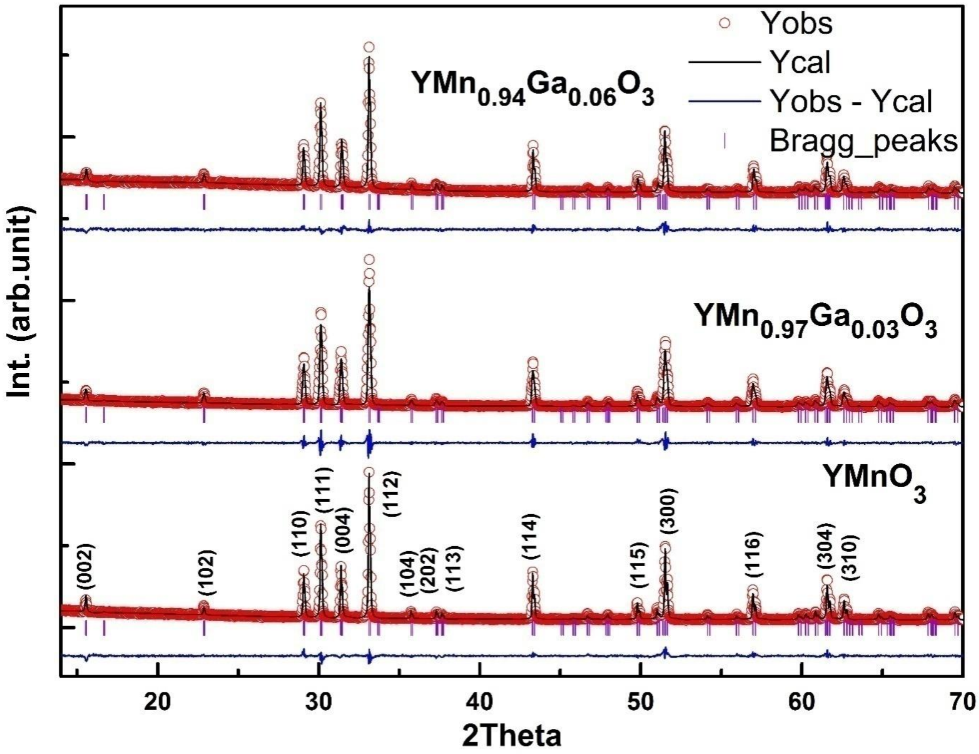

Figure 5.2: Rietveld-refinement of XRD patterns of polycrystalline $YMn_{1-x}Ga_xO_3$ (x = 0, 0.03, 0.06) samples recorded at room temperature.

Table 5.1: Lattice parameters, selected bond lengths and bond angles obtained from Rietveld refinement of XRD patterns of polycrystalline $YMn_{1-x}Ga_xO_3$ (x = 0.00, 0.03 and 0.06).

Parameters	$YMnO_3$	$YMn_{0.97}Ga_{0.03}O_3$	$YMn_{0.94}Ga_{0.06}O_3$
a = b (Å)	6.139(1)	6.142(2)	6.143(2)
c (Å)	11.398(2)	11.394(4)	11.381(3)
Mn-O1(Å)	1.896(2)	1.885(4)	1.896(2)
Mn-O2 (Å)	1.8103(8)	1.822(1)	1.807(6)
Mn-O3 (Å)	2.092(2)	1.950(1)	2.118(2)
Mn-O4 (Å)	2.047(9)	2.121(6)	2.037(9)
Y1-O1 (Å)	2.274(8)	2.261(1)	2.348(1)
Y1-O2 (Å)	2.276(8)	2.285(7)	2.241(5)
Y1-O3 (Å)	2.303(1)	2.330(2)	2.175(2)
Y2-O1 (Å)	2.300(5)	2.329(8)	2.352(7)
Y2-O2 (Å)	2.307(6)	2.325(1)	2.244(7)
Y2-O4 (Å)	2.420(1)	2.450(2)	2.580(2)
Mn/Ga-O3-Mn (˚)	119.00(1)	118.40(7)	119.00(1)
Mn/Ga-O4-Mn (˚)	118.30(4)	118.80(2)	118.20(5)

as shown in figure 5.2, which confirms the formation of a single phase with hexagonal ‘$P6_3cm$’ space group symmetry. The values of lattice parameters, selected bond lengths, bond angles, unit cell volume etc. have been tabulated in table – 5.1. It has been observed that the crystallographic ‘a’ axis increases with an increase in Ga doping concentration, whereas ‘c’ axis decreases, keeping the unit cell volume almost constant. An illustration of unit cell of $YMnO_3$ presented in Figure 5.1(a) has been drawn using VESTA software [193] with crystallographic information obtained from Rietveld-refinement.

A negligible change in lattice parameters is seen upon Ga substitution at Mn-site, presumably due to comparable ionic radii of Mn^{3+}(0.645 Å) and Ga^{3+} (0.62 Å). The apical bond lengths (see figure 1(a)) lengths (Mn-O1 and Mn-O2) are known to be smaller than basal bond lengths (Mn-O3 and Mn-O4) as evident from table – 5.1 [221]. It has been observed that Y2 - O4 bond lengths increase and ‘c’ axis decreases with an increase in Ga concentration, indicating that Ga substitution results in compression of MnO_5 polyhedron along ‘c’ axis. Intuitively, the substitution of non-magnetic Ga^{3+} for Mn^{3+} may results in reduction of magnetic frustration in $YMnO_3$, because replacement of one of the trimeric Mn^{3+} ions would diminish competitive magnetic interactions.

5.3.2 X-ray photoemission spectroscopy

The results of X-ray photoemission spectroscopy (XPS) studies have been presented in figures 5.3 and 5.4. The binding energies (BE) of Y-3d, Mn-2p, Ga-2p and O-1s obtained for unsubstituted as well as substituted compounds are summarized in table – 5.2. The BE values for Y observed in our samples are slightly lower than the values reported for Y_2O_3 which indicates that Y-O bond is comparatively less ionic in our system [222]. Figure 5.4 (a, b & c) shows the appearance of a pair of lines in the XPS spectrum corresponding to Y-3d which could have arisen due to oxygen deficient environment around Y atoms [223]. The spectra for O-1s for all the compounds are presented in figure 5.4 (d, e & f). A tail like feature is observed at lower energy region in all the O-1s spectra which could also be due to oxygen deficiency present in the compound [222]. The BE peaks of O-1s spectrum in $YMnO_3$ have been observed at 529.2 eV and 530.7 eV corresponding to non-bridging and bridging oxygen respectively. Our observations are in quite a good agreement with values reported in literature [111].

The right lower inset of figure 5.3 shows the XPS spectrum of Mn-2p in unsubstituted $YMnO_3$. A fit of Mn-2p spectrum for Mn-$2p_{3/2}$ and Mn-$2p_{1/2}$ peaks results in BE energies of 641.2 eV and 652.8 eV respectively. Thus, the spin orbit splitting of Mn-2p observed in unsubstituted $YMnO_3$ is 11.6 eV which is very close to that of MnO_2 [224]. Similarly, each peak in Mn-2p spectrum (Mn-2p$_{3/2}$ or Mn-2p$_{1/2}$) can be deconvoluted considering multiple Gaussian profiles corresponding to different oxidation states of Mn. For 2p$_{3/2}$, the fitted peaks have been observed at 640.6 eV and 642.5 eV corresponding to Mn^{2+} and Mn^{4+}, while those of 2p$_{1/2}$ are centred at 652.0 eV and 653.5 eV respectively.

Table 5.2: The binding energies in eV for all the atoms in YMn$_{1-x}$Ga$_x$O$_3$ (x = 0, 0.03, 0.06).

Sample	Y-3d		Mn-2p		Ga-2p		O-1s	
	3d$_{5/2}$	3d$_{3/2}$	2p$_{3/2}$	2p$_{1/2}$	2p$_{3/2}$	2p$_{1/2}$	1s-1	1s-2
YMnO$_3$	156.6	158.9	641.2	652.8	--	--	529.2	530.7
YMn$_{0.97}$Ga$_{0.03}$O$_3$	156.7	158.8	641.0	652.5	1117.0	1144.3	529.2	530.6
YMn$_{0.94}$Ga$_{0.06}$O$_3$	156.9	158.6	641.5	652.0	1116.3	1143.3	529.2	530.6

The deconvolution of peak corresponding to Mn-2p$_{3/2}$, as shown in right inset of figure 5.3, confirms the mixed valence state of Mn^{2+} and Mn^{4+} in unsubstituted YMnO$_3$. Considering the area under the fitted curves, the ratio of abundance of Mn^{2+} : Mn^{4+} is found to be 75 : 25 for YMnO$_3$ and 54 : 46 for YMn$_{0.97}$Ga$_{0.03}$O$_3$ compound. On the contrary, Mn-2p spectrum of YMn$_{0.94}$Ga$_{0.06}$O$_3$ could be fitted well with single Gaussian peak associated with Mn^{3+} as presented in the upper left inset of figure 5.3. The presence of Ga^{3+} ion has been confirmed from figure 5.3 which presents the complete survey spectrum of polycrystalline YMn$_{0.94}$Ga$_{0.06}$O$_3$. The BE values observed for Ga 2p$_{3/2}$ and 2p$_{1/2}$ are 1116.3 eV and 1143.3 eV respectively, very close to the values observed in Ga$_2$O$_3$ [225]. A peak associated with C-1s is shown in figure 5.3, which is expected (adventitious hydrocarbon present on samples introduced from laboratory environment) and was used to calibrate the spectrum. In oxide compounds, there exist two different mechanisms for mixed valence states. One is static case where the constituent valencies are present statically. Another mechanism is dynamic in which valency fluctuates about a mean value.

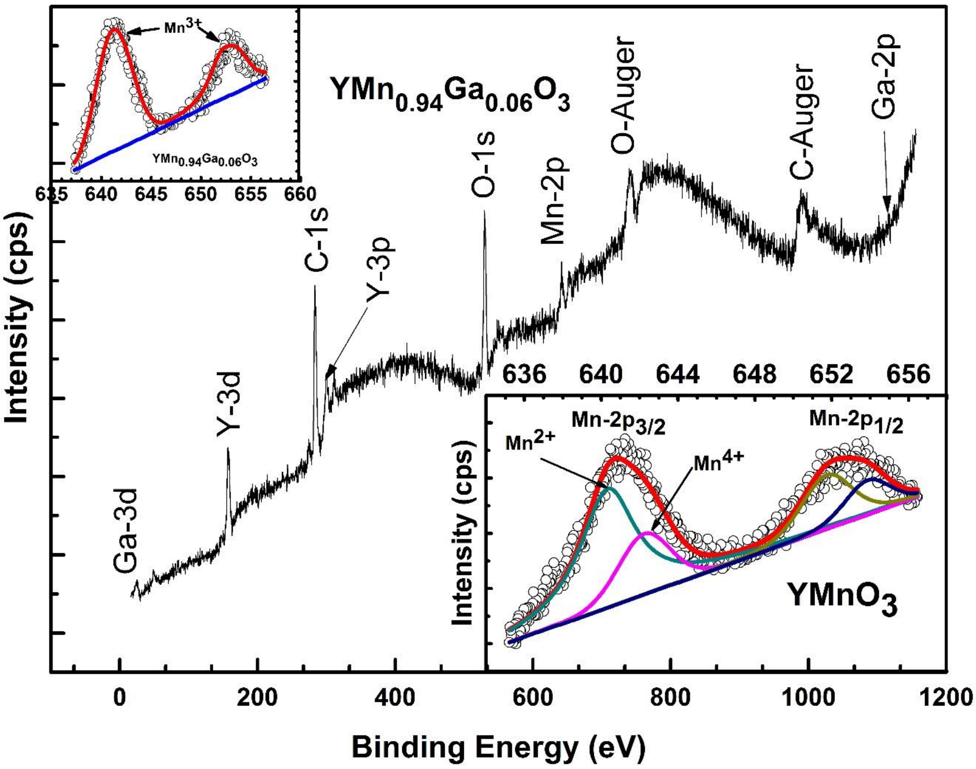

Figure 5.3: X-ray photoelectron spectroscopy survey spectrum for polycrystalline $YMn_{0.94}Ga_{0.06}O_3$. Inset shows XPS spectrum of Mn-2p in $YMnO_3$.

In dynamic case, the measured valency depends on the time constant of measurement [226, 227]. Measurements like XPS with time constants less than fluctuation time scales can look at the individual valencies, while slow or quasi static measurements like SQUID, VSM, XRD etc. can provide parameters associated with the average value of valencies. It is clear from our XPS analysis that unsubstituted $YMnO_3$ exhibits a mixed valence states of Mn^{2+} and Mn^{4+}, even though Mn atoms occupy crystallographically equivalent sites, indicative of Mn valence fluctuation between 2+ and 4+. We wish to clarify that the XPS spectrum of Mn-2p (upper left inset of figure 5.3) could be fitted with a combination of Mn^{2+} and Mn^{4+} ions as well as a single Mn^{3+} ion and in order to decide on the appropriate model we have relied on the magnetization data (see section on magnetization).

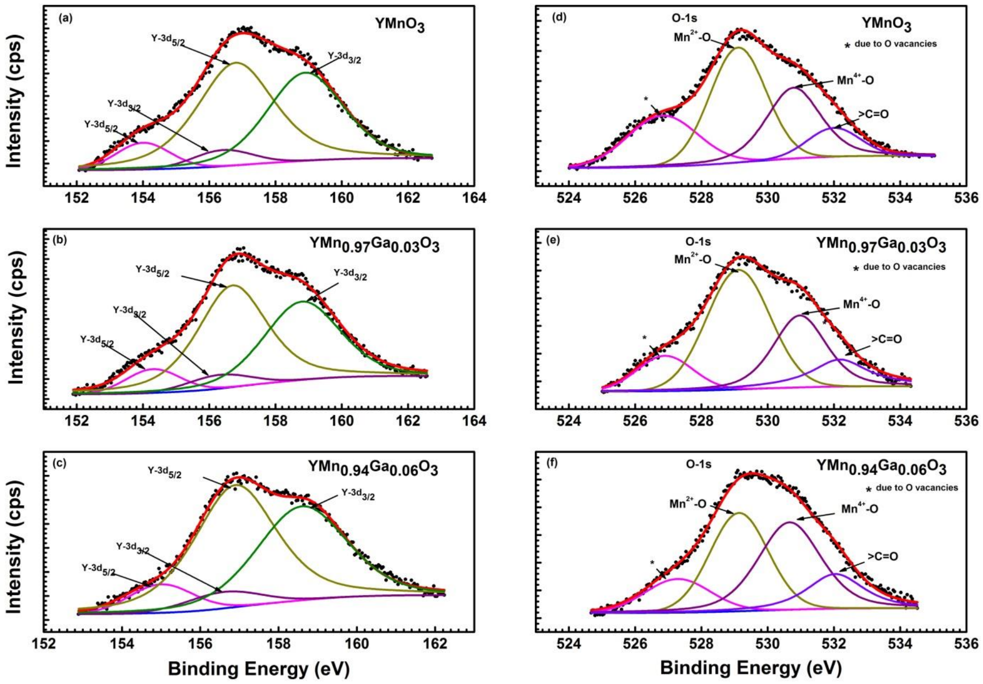

Figure 5.4: XPS spectra of Y-3d & O-1s respectively in $YMnO_3$ (a & d), $YMn_{0.97}Ga_{0.03}O_3$ (b & e) and $YMn_{0.94}Ga_{0.06}O_3$ (c & f). Black points and red lines are experimental data and fitting lines respectively.

5.3.3 Raman Spectroscopy

Figure 5.5 represents the Raman spectra of polycrystalline $YMnO_3$ and $YMn_{1-x}Ga_xO_3$ (x = 0.03 and 0.06) recorded in the range 50 – 800 cm^{-1} at room temperature. The unit cell of $YMnO_3$ stabilizes in a non-centrosymmetric structure with ‘$P6_3cm$’ space group symmetry. Group theory predicts 60 Γ- point modes for the ferroelectric phase of *h*-$YMnO_3$ (space group ‘$P6_3cm$’), out of which 38 Γ- point modes are Raman active [228, 229]. The irreducible representation for all the 38 Raman active modes can be shown as: $\Gamma_{Raman} = 9A_1 + 14E_1 + 15E_2$. In polycrystalline samples, many of these peaks get merged and appear as a broad peak. However, these broad peaks can be analyzed by multiple Lorentzian peak fitting method. Figure 5.6 represents the deconvolution of broad peaks that appeared in different frequency regions of Raman spectra of polycrystalline $YMn_{0.94}Ga_{0.06}O_3$ compound. The deconvoluted peak positions for all the compounds are tabulated in table – 5.3.

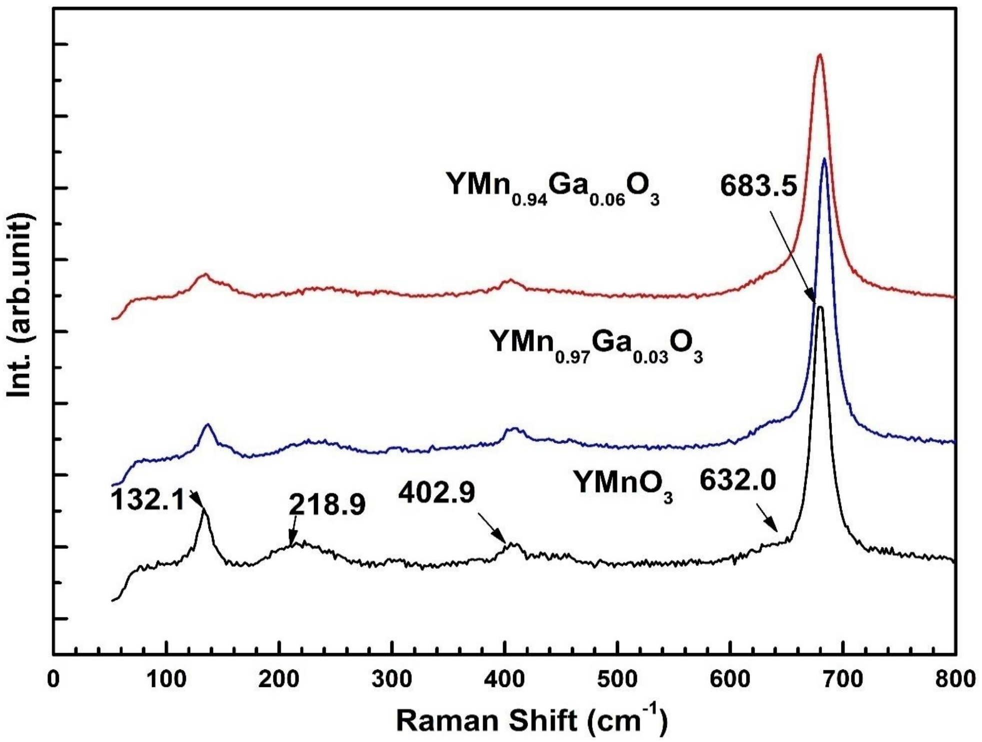

Figure 5.5: Raman spectra taken at room temperature for polycrystalline $YMnO_3$, $YMn_{0.97}Ga_{0.03}O_3$ and $YMn_{0.94}Ga_{0.06}O_3$.

The observed peak positions are close to the reported values [228, 230] and hence attest to the formation of a single phase. For comparison, we have also included the peak positions observed in single crystal $YMnO_3$ [228]. Although we have not observed any significant changes in the spectrum upon Ga substitution, some changes have been noticed which can be correlated to changes in the structure. Intensity of the peak at 632 cm^{-1} corresponding to E1 mode is seen to increase with increasing Ga concentration. This mode is associated with vibrations of basal oxygen atoms (O3 and O4) (see the figure 5.1 (a)). Similarly, a significant decrease in relative intensity of E2 mode at 135 cm^{-1} (associated with motion of Y atoms in 'ab' plane) has been observed. A significant variation of peak intensity at 215 cm^{-1} has also been noticed which is related to bonds of apical oxygen and Mn atoms [228]. The observed changes in intensity of peaks suggest variation in the oxygen content of the crystal structure which reflects in Mn valency (to be discussed in the next section).

Table 5.3: Experimental Raman-mode frequencies of hexagonal polycrystalline $YMn_{1-x}Ga_xO_3$ (x= 0.00, 0.03 and 0.06) and comparison with reported values.

Mode	$YMnO_3$(cm^{-1})	$YMn_{0.97}Ga_{0.03}O_3$	$YMn_{0.94}Ga_{0.06}O_3$	Reported [37]
A1	-----	147.7	147.1	148.0
A1	272.8	240.8	242.6	257.0
A1	296.6	298.2	296.2	297.0
A1	430.0	432.1	432.7	433.0
A1	447.6	456.1	450.9	459.0
A1	677.4	683.5	680.3	681.0
E1	633.2	638.5	635.7	632.0
E1	402.9	407.4	406.1	408.0
E2	132.1	136.8	132.2	135.0
E2	218.9	226.0	225.1	215.0

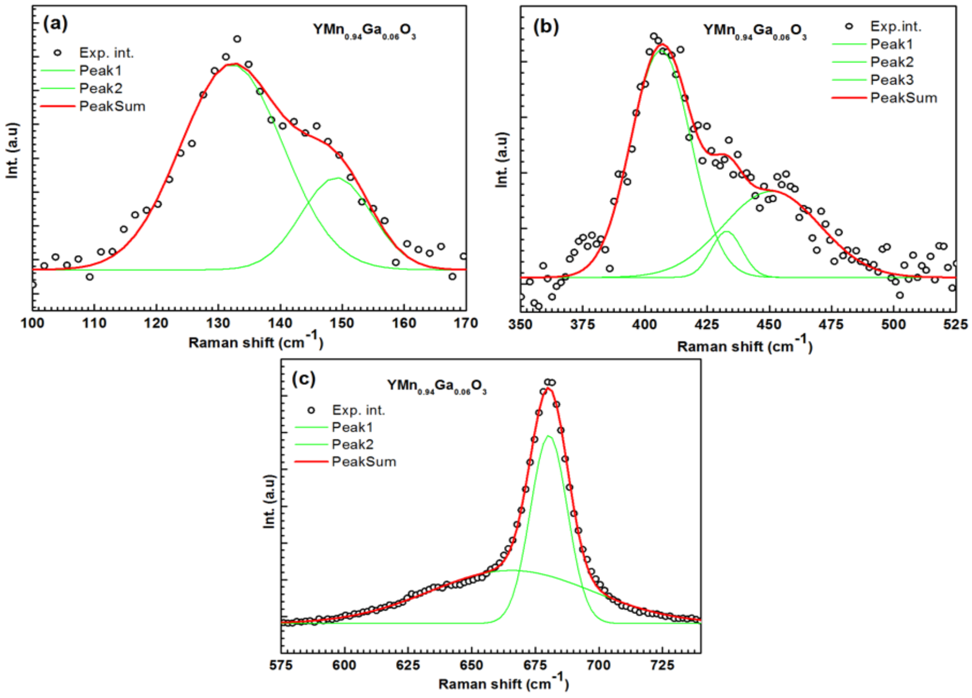

Figure 5.6: Deconvolution of broad peaks observed in Raman spectrum of polycrystalline $YMn_{0.94}Ga_{0.06}O_3$ in different frequency regions.

5.3.3 Magnetization studies

To study the magnetic frustration in polycrystalline $YMn_{1-x}Ga_xO_3$ (x= 0.00, 0.03 and 0.06), we have carried out temperature and field dependence of magnetization measurements in a wide range of temperature and magnetic field.

5.3.3.1 Temperature-dependent magnetization

The temperature-dependent magnetization (M-T) of polycrystalline $YMn_{1-x}Ga_xO_3$ (x= 0.00, 0.03 and 0.06) has been measured using a SQUID magnetometer in the temperature window 5 K – 300 K. The measurements have been performed under a dc field of 100 Oe in zero-field cooled (ZFC) and field-cooled (FC) protocols. In case of ZFC measurements, we cooled the sample first down to the lowest measuring temperature (~ 5 K) under zero magnetic field, applied a field of 100 Oe, and measured magnetization as the sample warmed up to 300 K. In case of FC measurements, data was acquired while the sample cooled down under the same field.

Figure 5.7 represents the ZFC and FC M-T of polycrystalline $YMn_{1-x}Ga_xO_3$ (x = 0.0, 0.03 and 0.06) measured under 100 Oe. The magnetization increases slowly with decreasing temperature down to 75 K for unsubstituted $YMnO_3$. However, it increases more rapidly at lower temperatures, with an anomaly at T_N ~ 75 K (i.e. bifurcation between ZFC and FC magnetization). A similar M-T response has been observed for all the compounds. The temperature at which the anomaly occurs decreases with increasing concentration of Ga. Mn^{3+} moments follow Curie-Weiss (CW) behaviour above T_N. Hence, the temperature-dependent magnetization data could be fitted to CW behaviour in the temperature range 130 K – 300 K for unsubstituted as well as substituted compounds. As the effective paramagnetic (μ_{eff}) moment depends on the number of magnetic ions present in the compound, it is expected that μ_{eff} should decrease with increasing concentration of Ga.

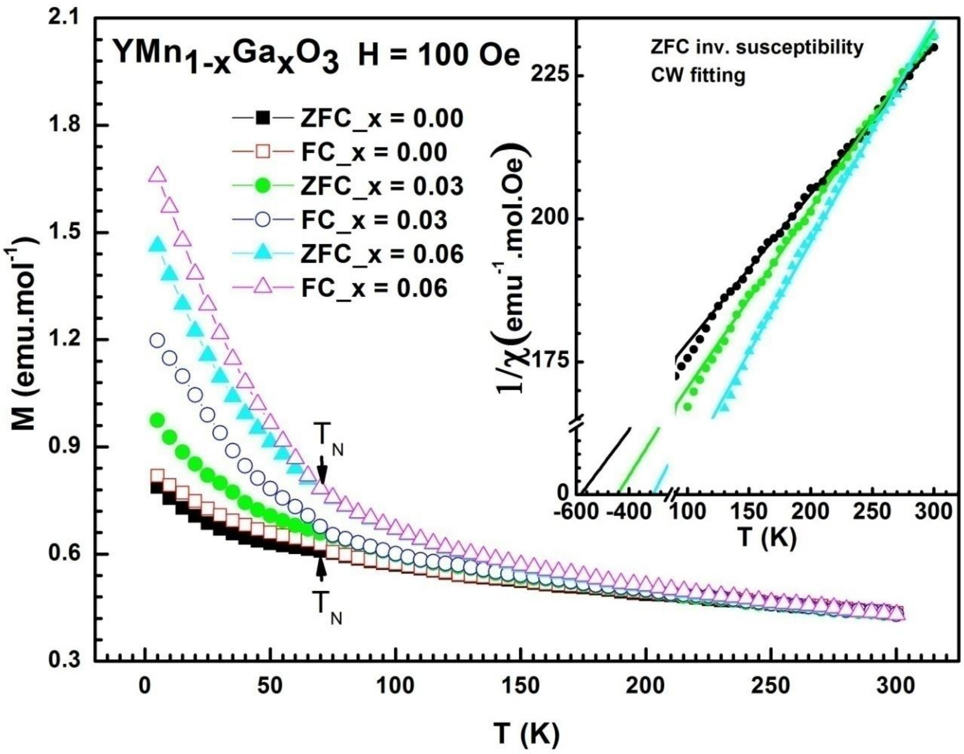

Figure 5.7: Temperature-dependent magnetization (M-T) of $YMn_{1-x}Ga_xO_3$ (x = 0.0, 0.03 and 0.06) measured under 100 Oe applied field. Inset shows Curie-Weiss fitting of ZFC susceptibility data for all the samples. Note that the data are plotted across broken axes to accommodate intercepts on temperature axis.

However, the overall magnetization, especially at lower temperatures, increases with Ga levels. The CW law (see equation – 1) predicts that the overall magnetization depends on θ_{cw} (CW temperature) inversely and on μ_{eff} directly (through constant ‘C’). An attempt has been made to analyze the ZFC M-T data by fitting with CW law as in equation – 1 and a satisfactory fit has been obtained in the temperature window 130 K - 300 K.

$$\chi = \frac{C}{T - \theta_{cw}} \qquad (1)$$

where C is the CW constant (slope of the curve) and θ_{cw} is the CW temperature. The magnetic moment per Mn atom (μ_{eff}) in Bohr Magnetons (μ_B) is given by,

$$\mu_{eff} = \sqrt{\frac{3k_B C}{(1-x)N\mu_B^2}} \qquad (2)$$

where x is the concentration of Ga atoms, while N and k_B are Avogadro number and Boltzmann constant. The effective paramagnetic moment per Mn atom has been evaluated from inverse susceptibility vs temperature curve as shown in the inset of figure 5.7. All the magnetic parameters obtained from CW fitting have been tabulated in table – 5.4.

Table 5.4: Magnetic parameters obtained by CW fitting of $\chi(T)$ for all the compounds.

Sample	T_N (K)	θ_{cw} (K)	$f=\theta_{CW}/T_N$	$\mu_{eff}(\mu_B)$
$YMnO_3$	75	-583	7.8	5.53 ± 0.04
$YMn_{0.97}Ga_{0.03}O_3$	75	-448	6.0	5.15 ± 0.04
$YMn_{0.94}Ga_{0.06}O_3$	65	-316	4.8	4.78 ± 0.03

It is seen from CW fitting that the variation in θ_{cw} is the dominating factor resulting in an increase in magnetization at low temperatures, as both μ_{eff} per Mn atom & θ_{cw} decrease with increasing Ga content (table – 5.4). It is important to mention that the estimation of CW temperature (θ_{cw}) could depend on the temperature range of CW fitting. While it is desirable to consider the temperature range far above the magnetic transition temperature for CW fitting, since the variation of magnetization in our case near room temperature is very small and may well be at the limits of measurement, it became necessary to consider data from a wide range of temperature for a reasonable change in susceptibility with temperature in order to reach at a dependable value of θ_{cw}. It is found that the selected temperature range of 130 K – 300 K is suitable and a satisfactory fitting has been obtained.

As there are no unpaired electrons in outer orbit of Ga^{3+}, contribution to magnetization due to Ga^{3+} is assumed to be zero and the entire magnetization arises from Mn ions alone. Considering the spin only values, the magnetic moment associated with Mn^{2+} ($3d^5$),

Mn^{3+} ($3d^4$) and Mn^{4+} ($3d^3$) ions works out to be 5.92 μ_B, 4.90 μ_B and 3.87 μ_B respectively. The effective paramagnetic moment for unsubstituted $YMnO_3$ compound obtained from CW fitting is 5.53 ± 0.04 μ_B.This value of μ_{eff} indicates that Mn ions perhaps are in a mixed valence state, an observation supported by XPS measurements as discussed earlier. It is noteworthy to mention that our XPS analysis reveals the presence of Mn^{2+} and Mn^{4+} in un-doped $YMnO_3$ compound. Assuming that the paramagnetic moment associated with Mn^{2+} and Mn^{4+} ions remain as an uncorrelated mixture in the temperature range above the transition temperature, the possible theoretical effective paramagnetic moment has been obtained using following formula [226],

$$\mu_{eff}(th) = \sqrt{y\mu^2(Mn^{+2}) + (1-y)\mu^2(Mn^{+4})} \qquad (3)$$

where, y and $(1-y)$ are the Mn^{2+} and Mn^{4+} ion concentrations present in the sample which can be calculated from the area under the binding energy curve of XPS.

The concentrations of Mn^{2+} and Mn^{4+} in un-doped $YMnO_3$ have been estimated from its XPS spectrum to be 75 : 25 and the calculated effective paramagnetic moment using this proportion is 5.46 μ_B, which is close to experimental value. Similarly, the values calculated for $YMn_{0.97}Ga_{0.03}O_3$ are 54:46 and 5.15 μ_B respectively. In case of $YMn_{0.94}Ga_{0.06}O_3$ the same fitting gives the proportion as 61:39, which corresponds to a magnetic moment of 5.22 μ_B. This value is far above the experimentally observed value of 4.78 μ_B. The fact that experimentally obtained effective moment is 4.78 μ_B close to that of Mn^{3+} ion (4.90 μ_B), combined with the fact that the spectrum could be fitted with a single Mn valency (Mn^{3+}), one could conclude that Mn is in 3+ state for this composition.

A bifurcation between ZFC and FC magnetization has been observed at 75 K for unsubstituted $YMnO_3$ which is a signature of a magnetic phase transition. A similar anomaly has been observed in specific heat and neutron diffraction studies confirming a magnetic phase transition to antiferromagnetic state from paramagnetic state at T_N ~ 75 K [201, 204]. 3% Ga substitution at Mn-site does not change the antiferromagnetic transition temperature significantly. However, the ordering temperature shifts to lower temperature (T_N ~ 65 K) in 6% Ga substituted compound. A similar observation has been reported by A. A. Nugroho et al [38] on single crystal of Ga doped $YMnO_3$, while an increase in transition temperature has been observed in polycrystalline Cr-modified $YMnO_3$ compound [230]. It is known that Mn^{3+} ions in $YMnO_3$ form a trimer as shown in Figure 5.1 (b). Due to an antiferromagnetic interaction between Mn^{3+} ions, this structure results in a geometrically frustrated magnetic system [72, 206]. The frustration factor (a measure of magnetic frustration) is defined as the ratio of CW temperature (θ_{cw}) and antiferromagnetic transition temperature (T_N). It is clear from table – 5.4 that the θ_{cw} plays a very important role in these cases. Although T_N has not changed in $YMn_{0.97}Ga_{0.03}O_3$ compound, it decreases to 65 K in $YMn_{0.94}Ga_{0.06}O_3$. On the other hand, θ_{cw} values obtained from CW fit are – 583 K, – 448 K and – 316 K for $YMnO_3$, $YMn_{0.97}Ga_{0.03}O_3$ and $YMn_{0.94}Ga_{0.06}O_3$ respectively. It is noted that the magnetic frustration factor decreases from 7.8 observed in unsubstituted $YMnO_3$ to 4.8 in $YMn_{0.94}Ga_{0.06}O_3$, as shown in table – 5.4. However, it has been reported in literature that the magnetic frustration factor increases at higher levels of Ga doping in $YMnO_3$, although such a doping decrease both θ_{cw} and T_N significantly. We believe this is due to the fact that higher concentrations result in larger decrease of T_N [38, 207].

5.3.3.2 Field-dependent magnetization

Magnetization measurements against applied magnetic field (M-H) on polycrystalline $YMn_{1-x}Ga_xO_3$ (x = 0.0, 0.03 and 0.06) compounds have been carried out upto a maximum field of ± 50 kOe at 300 K and 5 K.

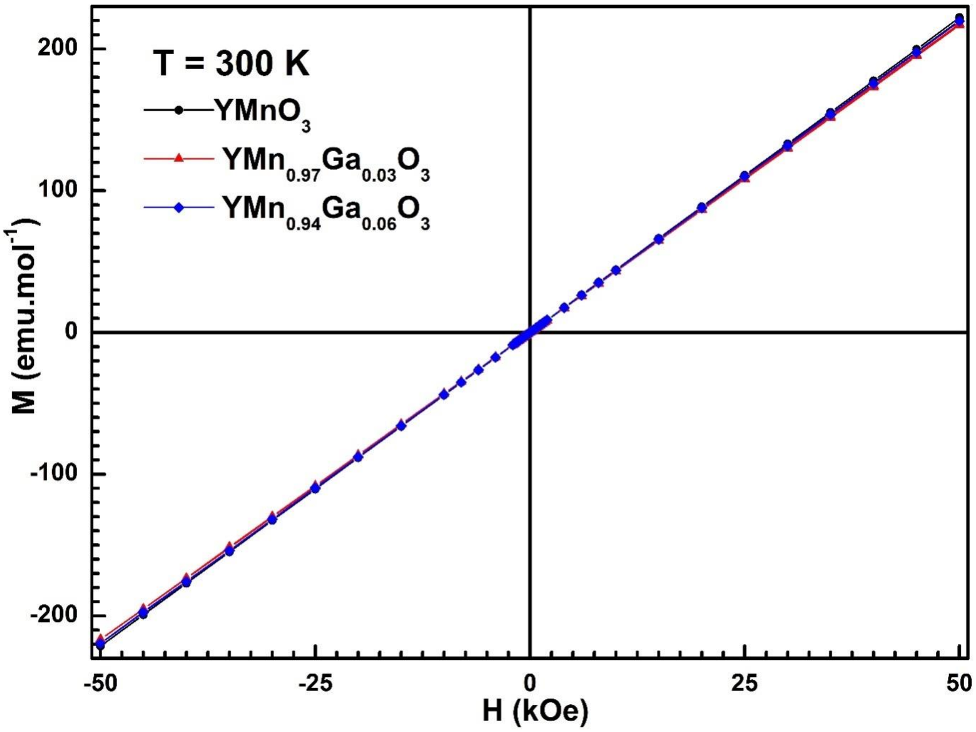

Figure 5.8: M as a function of H for $YMn_{1-x}Ga_xO_3$ (x = 0.0, 0.03 and 0.06) measured at 300 K.

The M-H measurement carried out at T = 300 K is shown in figure 5.8. A linear response of magnetization with applied field without any hysteresis is observed for all the compounds indicating a typical paramagnetic behaviour. Besides, magnetization of all the compounds overlaps completely in the entire field span. Figure 5.9 represents the M-H measurement performed at 5 K. It is clear from the figure that magnetization of unsubstituted compound shows a linear response with field, whereas a small coercivity of ~ 60 Oe is observed in substituted compounds. While coercivity is nearly the same in the two substituted compounds, a larger retentivity (0.956 emu.mol^{-1}) has been observed in $YMn_{0.94}Ga_{0.06}O_3$ in comparison to $YMn_{0.97}Ga_{0.03}O_3$ (0.686 emu.mol^{-1}). The presence of traces of Mn_3O_4 giving rise to such hysteresis can be ruled out because no indication of any magnetic ordering was observed at 42 K [231] and XRD does not show any indication of impurities.

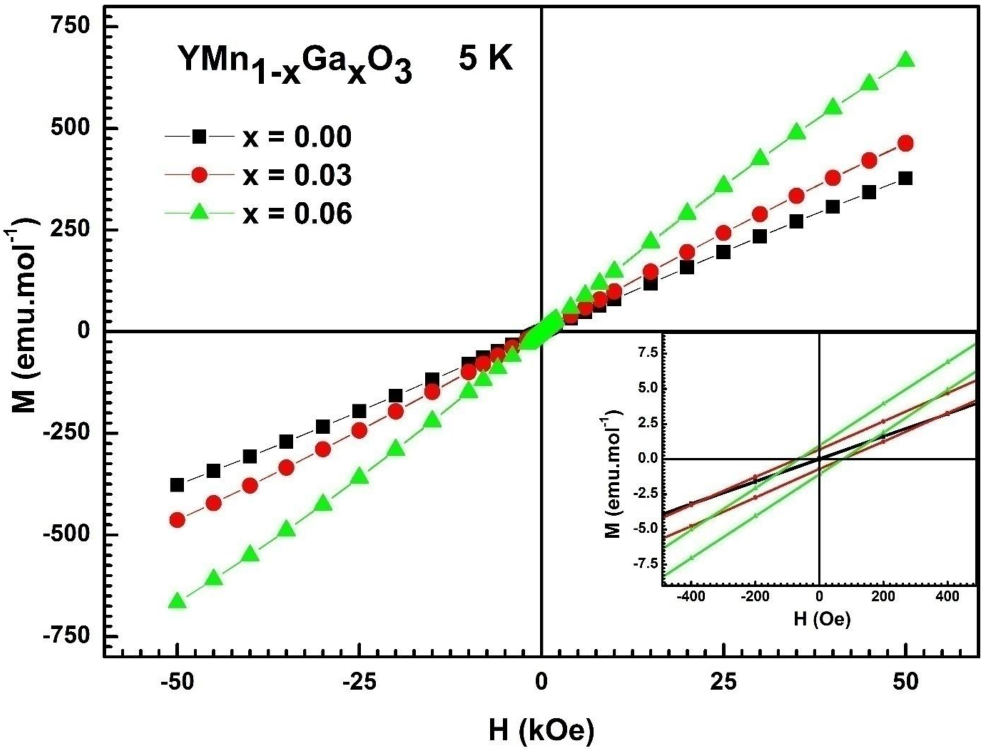

Figure 5.9: M as a function of H for $YMn_{1-x}Ga_xO_3$ (x = 0.0, 0.03 and 0.06) measured at 5 K. Inset shows magnified view in low field region.

5.4 Conclusion

Polycrystalline $YMn_{1-x}Ga_xO_3$ (x 0.0, 0.03 and 0.06) compounds have been prepared following solid-state reaction method. Rietveld-refinement of powder XRD patterns confirms the formation of single phases of Hexagonal structure with 'P63cm' space group symmetry in all the compounds. XPS analysis shows that Mn ions in unsubstituted $YMnO_3$ and $YMn_{0.97}Ga_{0.03}O_3$ exist in mixed valance states of Mn^{2+} and Mn^{4+} in proportions of 75 : 25 and 54 : 46 respectively. However, $YMn_{0.94}Ga_{0.06}O_3$ compound shows a stabilized Mn valency of 3+, an observation supported by our magnetization studies as well. Deconvolution of broad peaks in Raman spectra of $YMn_{0.94}Ga_{0.06}O_3$ shows the appearance of all the expected peaks which also confirms the phase purity of synthesized compound. We have not observed any significant differences in Raman spectra for unsubstituted and substituted compounds. Temperature-dependent magnetization of unsubstituted $YMnO_3$ reveals the known antiferromagnetic transition at T_N ~ 75 K. We could not observe any significant change in T_N for $YMn_{0.97}Ga_{0.03}O_3$, but it shifts to ~ 65 K for $YMn_{0.94}Ga_{0.06}O_3$ compound. The effective paramagnetic moment (μ_{eff}) obtained from CW fitting is 5.53 μ_B for unsubstituted compound which is larger than the expected moment associated with Mn^{3+} ion. However, as expected, μ_{eff} decreases with Ga substitution and the μ_{eff} value obtained for $YMn_{0.94}Ga_{0.06}O_3$ compound is 4.78 μ_B, which is close to the moment associated with Mn^{3+} ion. The magnetic moments obtained from temperature-dependent magnetization data are in good agreement with the mixed valency of Mn seen in XPS. Magnetization studies indicate geometric frustration in all the compounds, with frustration factor decreasing as Ga concentration increases.

A detailed study on magnetic frustration as a function of annealing atmosphere in $YMn_{0.67}Ga_{0.33}O_3$, a sample with a large Ga content, has been described in the following chapter.

Chapter 6

Role of Oxygen Stoichiometry on Structural and Magnetic Properties of $YMn_{0.67}Ga_{0.33}O_{3+\delta}$

6.1 Introduction

There has been an increased research interest in multiferroic materials in recent years because of their rich physical properties. Of particular interest is the coupling between magnetic and electric degrees of freedom, a demanding property in the emergent technology. The applications go beyond the obvious data storage to include the role of a transducer, electric and magnetic field sensors, etc. [232 ,233].

The perovskite rare-earth manganites ($LnMnO_3$, where, Ln = rare earth elements, In, Y and Sc) are one such class of materials that attracted special attention of the research community [234, 235]. These materials stabilize in two different structures, both displaying multiferroicity [236]. The orthorhombic form, a perovskite structure with space group (SG) 'Pbnm' at room temperature is favored for Ln = La – Tb. The other is the hexagonal polymorph with space group '$P6_3cm$', for Ln = Dy – Lu, In, Y, and Sc [199]. At room temperature, $YMnO_3$ stabilizes in hexagonal structure with a non-centrosymmetric '$P6_3cm$' space group (no. 185) [38]. The latter structure consists of layers of five-coordinated Mn^{3+} corner-sharing trigonal bipyramids separated by layers of Y^{3+} along 'c' direction. On cooling from high temperature, the MnO_5 units undergo a cooperative tilting distortion which buckles the trigonal planes and the Y^{3+} ions are displaced in the opposite direction along the polar 'c' axis [237]. A subtle shift of trigonal bipyramids layers connecting the Y^{3+} layer introduces ferroelectricity at 1250 K [72]. The Mn^{3+} sub-lattice has an antiferromagnetic order on the trigonal lattice with a N'eel temperature (T_N) ~ 75 K [238]. Well above 75 K, the temperature-dependent magnetization of $YMnO_3$ follows Curie-Wiess (CW) law with CW constant (θ_{cw}) varying in the range -400 K – 575 K as reported by different studies [208 - 210]. Due to triangular geometry and strong antiferromagnetic interaction between magnetic moments of Mn [72], $YMnO_3$ is known to be a magnetically frustrated system. A measure of magnetic frustration is defined by A. P. Ramirez [206] as the ratio of θ_{cw}/ T_N which is reported to vary from 5.7 to 7.9 for the $YMnO_3$ compound [38, 207].

Effect of doping on the structure and magnetic behavior of $YMnO_3$ has been studied by several research groups, using both magnetic and non-magnetic ions. Tai-Chun Han et al have observed improved magnetic properties and decreased magnetic frustration upon Cr substitution at Mn site [216]. Sonu Namdeo et al [215] substituted Fe for Mn which resulted in a non-monotonous variation in the frustration factor, while Neetika Sharma et al [207] observed no change in the frustration factor for 10% Fe substitution at Mn site. The latter have not seen any change with 10% Ga substitution either [207], whereas Nugroho et al [38] have noted an increase of magnetic frustration upon Ga substitution.

Also, oxygen nonstoichiometry in $LnMnO_3$ has become a subject of research interest because it influences the crystal structure as well as its electrical and magnetic properties. Synthesis of the $LnMnO_3$ phase in air or oxygen is seen to result in stoichiometric oxygen content, except for R = La [239], Nd [240] and Pr [240]. Takeda et al [241] studied the unit cell changes with oxygen nonstoichiometry in $LaMnO_{3+\delta}$ and suggested that oxygen excess can be explained in term of cation defects rather than by interstitial oxygen. Cherepanov et al [240] have studied the excess oxygen in $PrMnO_{3+\delta}$ and $NdMnO_{3+\delta}$ and explained the results in terms of manganese deficiency. However, it was reported by Remsen et al [242] that polycrystalline $(Dy,Y)MnO_{3+\delta}$ prepared in air possess oxygen nonstoichiometry. Skjærvø et al prepared polycrystalline $YMnO_{3+\delta}$ in air, studied its electrical conductivity and explained the results in terms of interstitial oxygen [243].

Here we have elaborated on this subject further. The effect on structural and magnetic properties of Ga substitution in $YMnO_3$ at low concentration has been discussed in the previous chapter (chapter 5). In this chapter, we have studied structural and magnetic properties of polycrystalline $YMn_{0.67}Ga_{0.33}O_{3+\delta}$ (YMGO) synthesized in different atmospheres like air, high purity oxygen, argon and vacuum. Significant changes in magnetic properties have been observed in YMGO compounds so prepared, in line with Rietveld-refinement analysis of their XRD data.

6.2 Experimental details

Polycrystalline $YMn_{0.67}Ga_{0.33}O_{3+\delta}$ (YMGO) compounds have been prepared following solid-state reaction route using high purity (4N) oxide powders of Y_2O_3, MnO_2, and Ga_2O_3. Stoichiometric amounts of starting materials have been weighed and mixed using an agate mortar and pestle in a medium of analytical grade acetone, to achieve high homogeneity. All the starting materials have been heated up and held at 623 K for 10 h to get rid of moisture. Mixed powders were heated in air to 1273 K with a rate of 3˚C/min and held for 24 h. The process of grinding, mixing, and heating has been repeated multiple times. Then the powder was pelletized and sintered at 1523 K for 24 h in high purity Argon (Ar) atmosphere. Subsequently, three additional samples of YMGO compound were prepared under different annealing atmospheres using pellets prepared in Ar, as follows: further heated to 773 K in the air for 10 h and quenched to room temperature, heated to 773 K in high purity O_2 and vacuum for 10 h separately, and then slowly cooled (1˚C /min) down to room temperature. We have chosen to indicate the samples as following, (1) YMGO heated in O_2 atmosphere as YMGO_O_2, (2) YMGO quenched in air as YMGO_AQ, (3) heated in Ar atmosphere as YMGO_Ar and (4) heated in a vacuum as YMGO_vacu. The phase purity of polycrystalline YMGO has been characterized using X-ray diffraction (XRD) technique by an X-ray diffractometer, model: Rigaku Miniflex-600, using a filtered Cu K_α radiation of average wavelength λ = 1.5418 Å. Scanning is done in the 2θ range 14°- 80° with a step size of 0.02° and a scan speed of 0.5 s per step. Magnetization (M) as a function of temperature (T) has been measured in the temperature range 5 K – 300 K using a SQUID magnetometer (M/s. Quantum Design, model MPMS) under applied magnetic field (H) of 1000 Oe. Isothermal field-dependent magnetization was measured under applied fields up to ± 50 kOe.

6.3 Results and discussion

6.3.1 X-ray diffraction and Rietveld-refinement

The phase purity of the synthesized polycrystalline YMGO compounds was analyzed using its powder X-ray diffraction (PXRD) pattern. The crystal structure of unsubstituted $YMnO_3$ (YMO) contains two sites for Y atoms (Y1 and Y2) at 2a and 4b positions, Mn atom at 6c position and four different sites for O atoms at 6c, 6c, 2a and 4b Wyckoff positions.

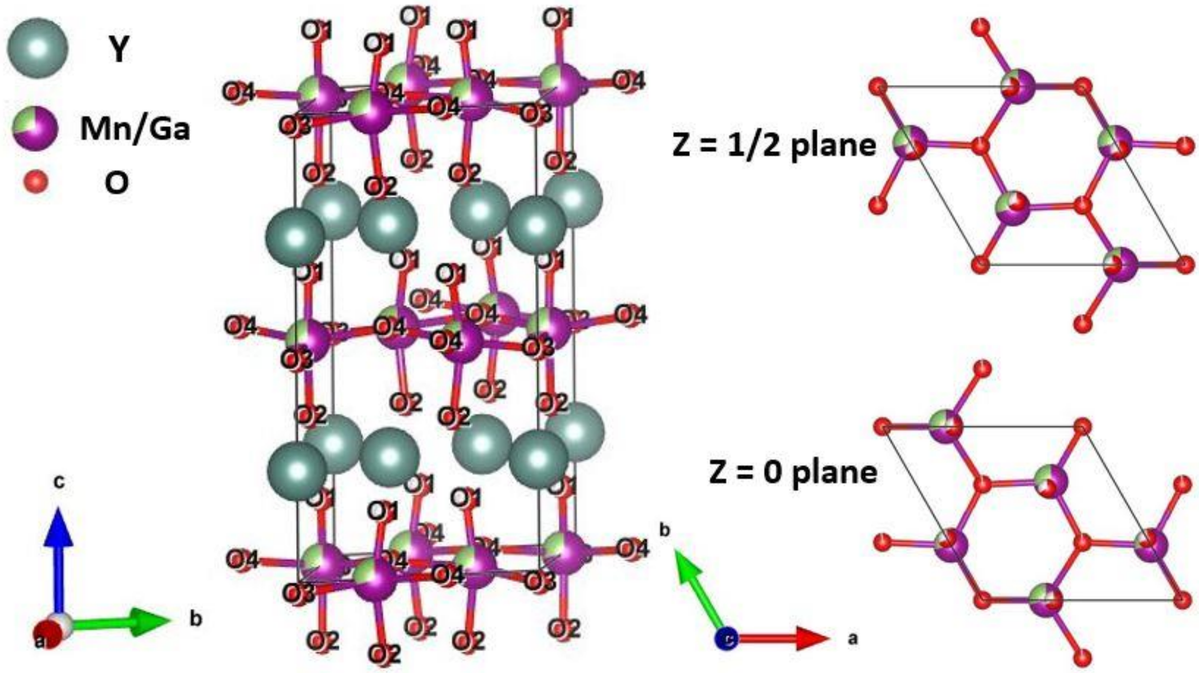

Figure 6.1: Crystal structure of unit cell of YMGO_O_2 obtained from Rietveld-refinement of PXRD pattern taken at room temperature (left). Perpendicular view (along ‘c’ axis) of ‘ab’ plane: an illustration of trimers formed by Mn^{3+} ions in Z = 0 and Z = ½ planes (right).

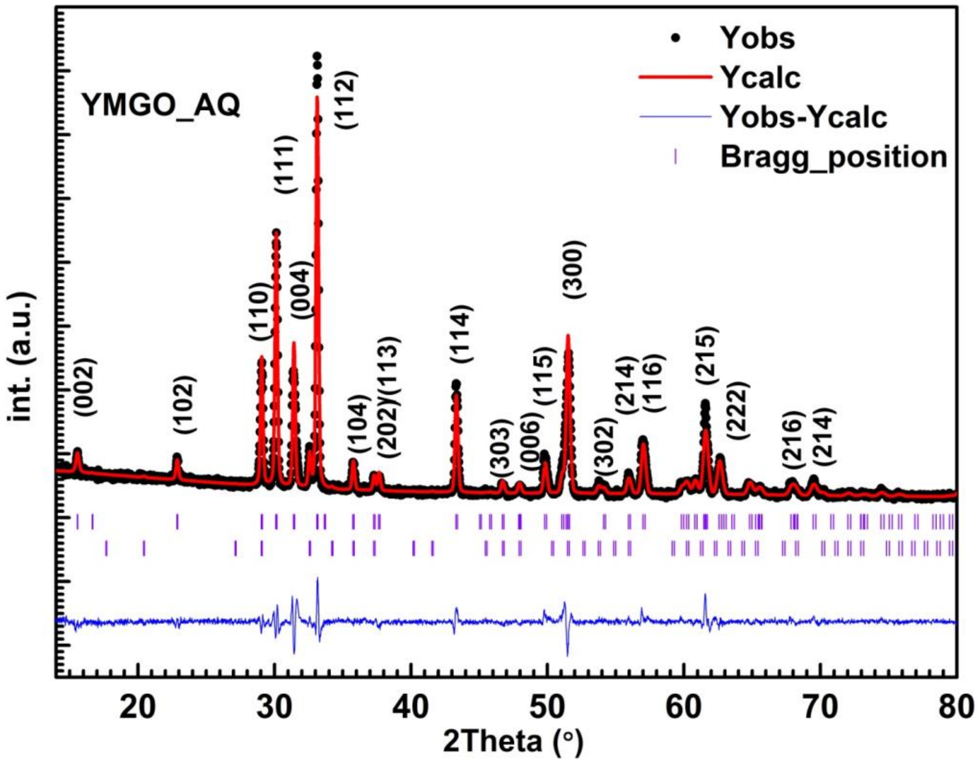

Figure 6.2: Rietveld-refinement of PXRD pattern of polycrystalline YMGO_AQ taken at room temperature along with indexing of observed peaks. Upper and lower indices correspond to '$P6_3cm$' and '$Ia\bar{3}d$' space group symmetries respectively.

Mn atoms located in 'ab' plane form a trimer with corner-sharing MnO_5 polyhedra. Layers of MnO_5 polyhedron are separated by layers of Y atoms along the 'c' axis as shown in figure 6.1. The PXRD patterns of polycrystalline YMGO_AQ, YMGO_Ar, YMGO_vacu and YMGO_O_2 recorded at room temperature have been represented in figure 6.2, figure 6.3, figure 6.4, and figure 6.5 respectively. Preliminary investigations of PXRD patterns reveal that all the peaks observed in each case correspond to hexagonal structure with '$P6_3cm$' space group (SG no. 185) [237]. In addition, a small shoulder at $2\theta \sim 31.15^\circ$ has been observed for all the compounds. Investigations reveal that the shoulder is due to the presence of Mn free $Y_3Ga_5O_{12}$ garnet phase with space group $Ia\bar{3}d$ (SG no. 230) [244]. Hence, we have refined the PXRD data in each case considering the hexagonal structure with '$P6_3cm$' space group as major phase along with the cubic structure with space group $Ia\bar{3}d$ as minor phase.

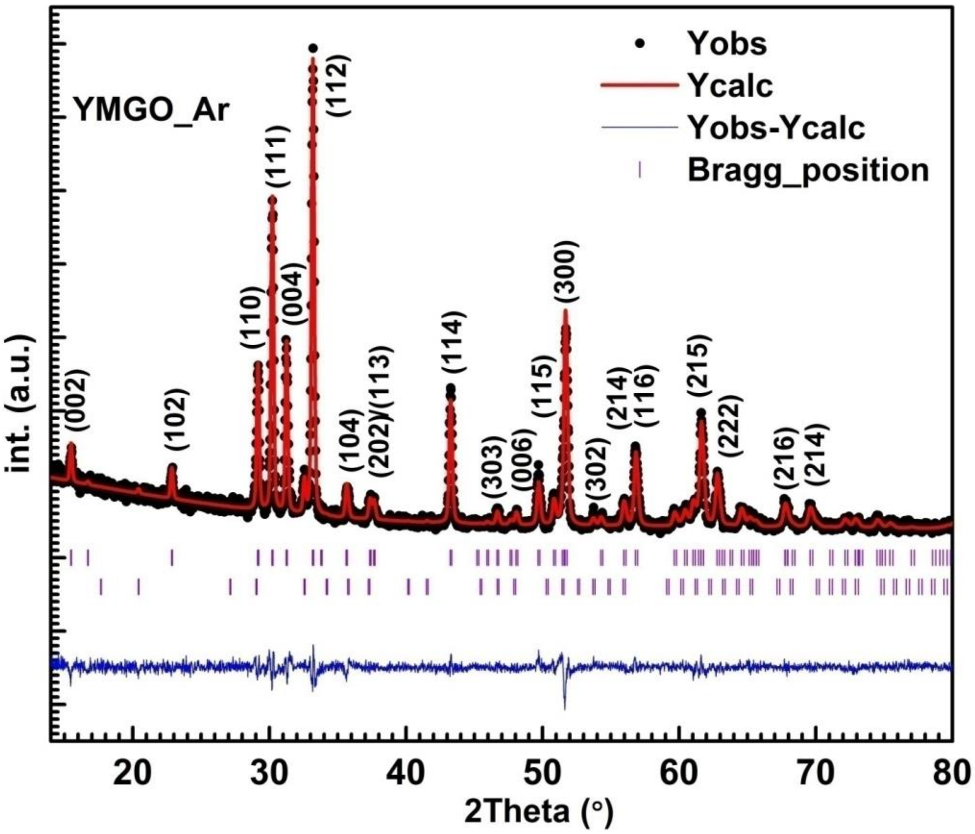

Figure 6.3: Rietveld-refinement of PXRD pattern of polycrystalline YMGO_Ar taken at room temperature along with indexing of observed peaks. Upper and lower indices correspond to ‘P6$_3$cm’ and ‘Ia$\bar{3}$d’ space group symmetries respectively.

The Rietveld-refinement has been carried out using Fullprof software [111, 191]. The reference inputs for the refinement have been collected from ICSD database with collection code 181183 [237] associated with major phase and garnet phase collection code no 14343 [244] associated with minor phase. Rietveld-refinement of PXRD patterns along with Bragg positions and the difference in calculated and experimentally observed intensities have been shown in figure 6.2, figure 6.3, figure 6.4, and figure 6.5 for YMGO_AQ, YMGO_Ar, YMGO_vacu and YMGO_O$_2$ respectively. A good agreement between observed and calculated intensities has been observed in all the cases as is clear from respective refinement plots. The lattice parameters, atomic positions, bond lengths, bond angles etc. obtained from Rietveld-refinement are summarized in table – 6.1.

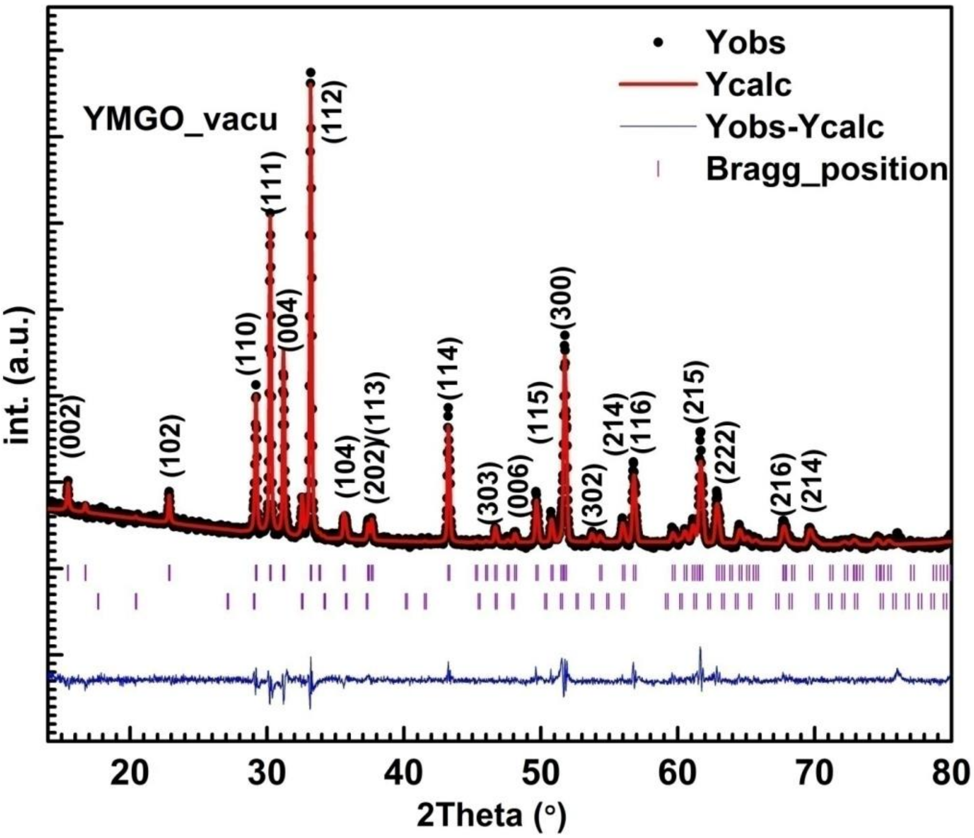

Figure 6.4: Rietveld-refinement of PXRD pattern of polycrystalline YMGO_vacu taken at room temperature along with indexing of observed peaks. Upper and lower indices correspond to '$P6_3cm$' and '$Ia\bar{3}d$' space group symmetries respectively.

Assuming that compounds prepared in different annealing environments have different oxygen stoichiometry, a significant effect of annealing environment on crystal structure is evident from table – 6.1. For a comparison, we have also included the structural parameters of unsubstituted $YMnO_3$ (prepared in air) from our previous studies discussed in Chapter 5. A large value of lattice parameter 'a' of 6.214(2) Å has been observed in the YMGO_O_2 compound whereas, the values obtained for YMGO_AQ, YMGO_Ar and YMGO_vacu are 6.144(1) Å, 6.123(5) Å and 6.117(2) Å respectively. Similarly, a smaller value of 'c' of 11.207(2) Å has been observed in YMGO_O_2 compared to 11.386(3) Å, 11.449(2) Å and 11.462(3) Å observed in YMGO_AQ, YMGO_Ar and YMGO_vacu compounds.

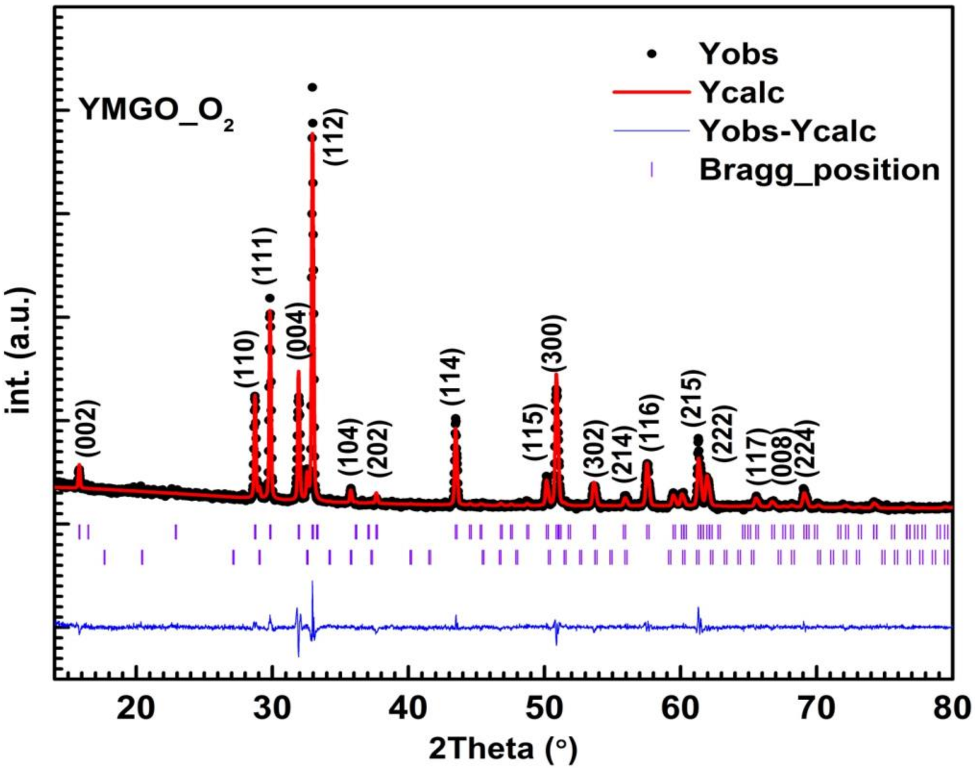

Figure 6.5: Rietveld-refinement of PXRD pattern of polycrystalline YMGO_vacu taken at room temperature along with indexing of observed peaks. Upper and lower indices correspond to '$P6_3cm$' and '$Ia\bar{3}d$' space group symmetries respectively.

Table 6.1: Lattice parameters obtained from Rietveld refinement of PXRD taken at room temperature for YMO and YMGO compounds.

Parameters	YMO	YMGO_O_2	YMGO_AQ	YMGO_Ar	YMGO_Vacu
a = b	6.140(3)	6.214(2)	6.144(1)	6.123(5)	6.117(2)
c	11.395(4)	11.207(2)	11.386(3)	11.448(2)	11.462(3)
Mn – O1	1.7919	1.629	1.6889	1.7502	1.8006
Mn – O2	1.8608	1.7839	1.8669	1.8903	1.8908
Mn – O3	2.0129	1.9774	1.9623	1.9633	1.9686
Mn – O4	2.0769	2.133	2.1119	2.0925	2.0837
Mn^{3+} - Mn^{3+}	3.585(3)	3.686(3)	3.624	3.607	3.595
Y1 - Y2	3.575	3.5943	3.577(2)	3.565(6)	3.562(2)
O1 -Mn – O2	175.29	170.37	179.18	175.14	173.22
Mn1-O4-Mn1	119.27	119.48	118.17	119.01	119.19
Mn1-O3-Mn1	118.89	118.53	119.99	119.82	119.94

Although there are significant variations in lattice parameters, one can observe that the unit cell volume (V) remains almost constant ($\Delta V \sim 0.7\%$ of YMO) in all the cases (see table – 6.1). It has been observed that the apical bond lengths (Mn – O1 and Mn – O2 as shown in figure 6.1) decrease and basal bond lengths (Mn – O3 and Mn – O4 as shown in figure 6.1) increase in YMGO_O_2 compound in comparison to others. This observation can be ascribed to elongation of axis 'a' and contraction of axis 'c' as shown in table – 6.1.

As Mn^{3+} ions are situated only in 'ab' plane, an expansion of 'a = b' axes increases the average distance between Mn^{3+} - Mn^{3+} ions in YMGO_O_2. The Mn^{3+} - Mn^{3+} distance observed in YMGO_O_2 is 3.686(3) Å which is comparatively larger than that observed in YMGO_AQ, YMGO_AR and YMGO_vacu compounds as shown in table – 6.1. We expect that an excess amount of oxygen in YMGO_O_2 compound and an increase in Mn^{3+} - Mn^{3+} inter-atomic distance would impact its magnetic properties, as magnetic interaction strongly depends on the overlap of atomic orbitals of neighboring atoms. Figure 6.1 shows the unit cell of the YMGO_O_2 system illustrated using VESTA software [193]. The crystallographic information file has been extracted from Rietveld refinement of PXRD of polycrystalline YMGO_O_2. The right-hand side of figure 6.1 shows a schematic diagram of Mn trimers in Z = 0 and Z = ½ planes. The amount of minor phase ($Y_3Ga_5O_{12}$) present in all the compounds is confirmed to be less than 5 % from Rietveld-refinement. Due to the absence of magnetic Mn ions, $Y_3Ga_5O_{12}$ would not affect the magnetic properties of YMGO compounds synthesized under different annealing atmospheres.

6.3.2 Magnetization studies

To study the effect of annealing atmosphere on magnetic properties of YMGO compounds, we have performed temperature and field dependent magnetization measurements over a wide range of temperature and magnetic field.

6.3.2.1 Temperature-dependent magnetization

Temperature-dependent magnetization (M-T) measurements in zero-field cooled (ZFC) and field cooled (FC) modes under a dc field of 1000 Oe have been carried out on polycrystalline YMGO compounds synthesized under different annealing atmospheres. The ZFC and FC protocols have been described in the previous chapter. A clear overlap of ZFC and FC magnetization has been observed for all YMGO compounds as shown in figure 6.6. For better clarity, we have plotted their FC magnetization alone and shown in figure 6.7, along with FC magnetization of unsubstituted YMO prepared in air for comparison. An enlarged view of magnetization near room temperature has been shown in the inset (a) of figure 6.7. It is clear from the inset (a) that magnetization of YMGO_AQ, YMGO_Ar and YMGO_vacu compounds is lower than that of YMGO_O_2 (also lesser than YMO magnetization, as expected).

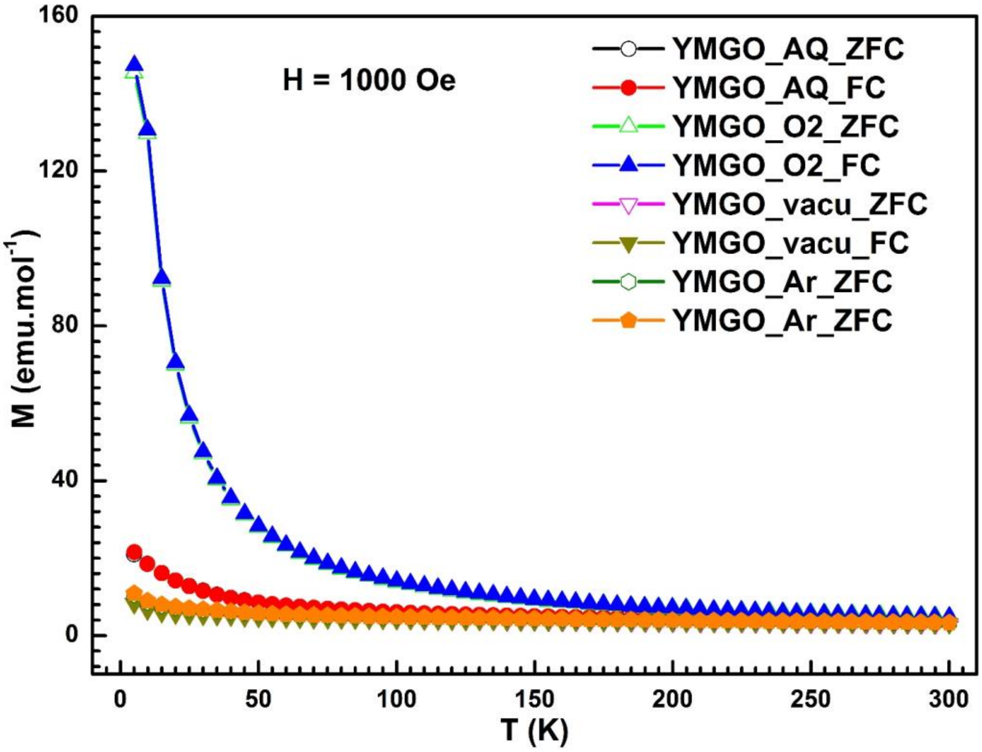

Figure 6.6: Zero-field cooled (ZFC) and field-cooled (FC) magnetization as a function of temperature of polycrystalline YMGO_AQ, YMGO_Ar, YMGO_vacu and YMGO_O_2 measured under a dc field of 1000 Oe.

However, a larger magnetization has been observed in YMGO_O_2 in comparison to unsubstituted YMO, presumably associated with excess oxygen content in the former compound.

Further, while magnetization of YMGO_O_2 follows Curie-Weiss (CW) behavior in the temperature range 5 K - 300 K, a near temperature-independent behavior is observed in case of YMGO_AQ, YMGO_Ar and YMGO_vacu. The low temperature magnetization of YMGO_AQ is seen to increase with decreasing temperature as shown in inset (b) of figure 6.7.

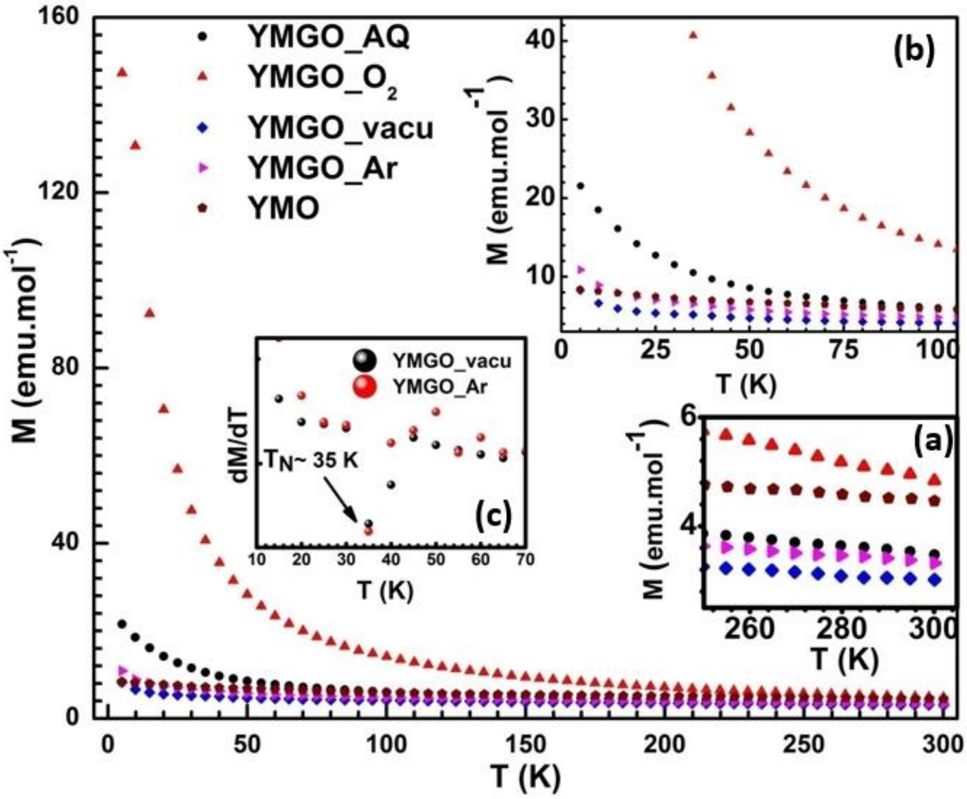

Figure 6.7: Temperature-dependent FC magnetization plots for polycrystalline YMO and YMGO compounds. Inset (a, b) shows an enlarged view in the low and high-temperature regions. Inset (c) shows the Neel temperature obtained from a minimum of dM/dT vs T plot for YMGO_Ar and YMGO_vacu.

The antiferromagnetic transition temperature for YMGO_Ar and YMGO_vacu compounds ($T_N \sim$ 35K) was determined as the minimum of the derivative of FC M-T curve, as shown in the inset (c) of figure 6.7, whereas we have not observed any such minima for other compounds. A similar antiferromagnetic transition has also been observed at $T_N \sim 35$ K in single crystal $YMn_{0.7}Ga_{0.3}O_3$ by Nugroho et al [38].

The temperature-dependent FC susceptibility data has been analyzed by fitting with modified CW law (shown in figure 6.8) as expressed in equation – 6.1,

$$(\chi - \chi_0)^{-1} = C^{-1}(T - \theta_{cw}) \qquad (6.1)$$

where χ_0 is the temperature-independent contribution to susceptibility mainly due to excess oxygen content, C is the Curie constant and θ_{cw} is the CW temperature. The magnitude of θ_{cw} is a measure of the strength of magnetic interaction among magnetic ions present in the compound, whereas the sign of θ_{cw} indicates the nature of magnetic interaction (positive and negative value corresponds to ferromagnetic and antiferromagnetic interactions). The effective paramagnetic moment (μ_{eff}) associated with each Mn atom in Bohr Magnetons (μ_B) has been calculated using CW constant as per the following equation – 6.2,

$$\mu_{eff} = \sqrt{\frac{3k_B C}{(1-x)N\mu_B^2}} \qquad (6.2)$$

where x and $(1-x)$ are the concentrations of Ga and Mn atoms, being 0.33 and 0.67 respectively. N is the Avogadro number and k_B is the Boltzmann constant.

It is worth mentioning that the estimation of θ_{cw} could depend on temperature range of fitting. Therefore, it is desirable to consider a large temperature range for a significant variation of susceptibility with temperature. A satisfactory fitting of inverse susceptibility data to modified CW law has been obtained in the temperature range 100 K – 300 K for all the compounds and same has been shown in figure 6.8. Magnetic parameters obtained from fitting have been tabulated in table – 6.2. For a better comparison, we have also included the

CW fitting results from our previous studies on unsubstituted YMO compound (see Chapter 5).

Table 6.2: The magnetic parameters extracted from modified Curie-Weiss fitting for polycrystalline YMO and YMGO compounds respectively.

Sample	χ_0 (emu.mol^{-1}.Oe^{-1})	θ_{cw} (K)	$f = \theta_{cw}/T_N$	μ_{eff} (μ_B)
YMO	0.00	-589	7.8	5.55 ± 0.04
YMGO_O$_2$	0.00031(1)	2	--	4.02 ± 0.02
YMGO_AQ	0.00107(4)	-93	--	3.39 ± 0.04
YMGO_Ar	0.00021(2)	-331	9.4	4.88 ± 0.05
YMGO_Vacu	0.00023(1)	-408	11.6	4.88 ± 0.02

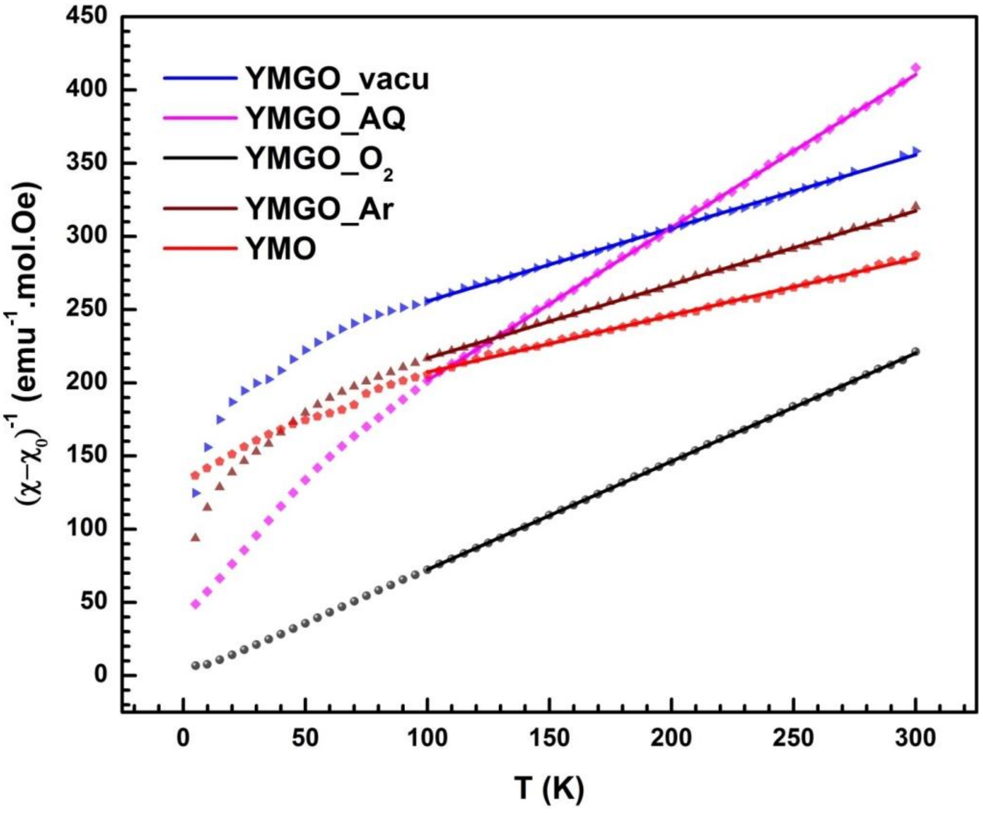

Figure 6.8: Curie-Weiss fitting of inverse FC susceptibility vs temperature data in the temperature range 100 K – 300 K. Symbols and lines represent experimental data and CW fitting respectively.

Considering spin only moment, the magnetic moment associated with Mn^{2+} ($3d^5$), Mn^{3+} ($3d^4$), and Mn^{4+} ($3d^3$) ions works out to be 5.92 μ_B, 4.90 μ_B, and 3.87 μ_B respectively. An effective magnetic moment (μ_{eff}) of ~ 5.55 μ_B has been obtained for unsubstituted YMO which indicates that Mn ions perhaps exist in mixed valences states. A similar observation has also been reported previously [218]. CW fitting in the same temperature range for YMGO_Ar and YMGO_vacu compounds (figure 6.8) results in μ_{eff} ~ 4.88 μ_B for both cases which is close to the expected moment (4.90 μ_B) associated with Mn^{3+} ions. However, the μ_{eff} obtained forYMGO_O$_2$ and YMGO_AQ are ~ 4.02 μ_B and 3.39 μ_B respectively, which are smaller than 4.90 μ_B expected for Mn^{3+} ion, indicating Mn perhaps exists in mixed valence state of Mn^{3+} and Mn^{4+}. Skjærvø et al [243] have studied non-stoichiometric $YMnO_{3+\delta}$ and discussed the role of excess oxygen in term of partial conversion of Mn^{3+} ion to Mn^{4+} ion.

As the magnetic interaction strongly depends on the overlap of atomic orbitals, the average distances between Mn ions has been estimated from Rietveld-refinement as shown in table – 6.1. Figure 6.9 shows θ_{cw} values plotted against the average distance between Mn ions. While a large negative CW temperature (θ_{cw}) of – 589 K in YMO indicates a strong antiferromagnetic interaction between Mn moments, it decreases to – 331 K and – 408 K in YMGO_Ar and YMGO_vacu compounds (table – 6.2), indicating an increase in distance between Mn^{3+} ions as is clear from figure 6.9. Thus, θ_{cw} values obtained from CW fitting are in corroboration with Rietveld-refinement, for all the compounds.

A small temperature-independent contribution (χ_0) to the susceptibility has been observed in YMGO samples. The origin of χ_0 could lie with excess amount of oxygen accommodate in the crystal structure. We have also calculated magnetic frustration factor (f) for unsubstituted YMO, YMGO_Ar and YMGO_vacu compounds and tabulated in table – 6.2. It is evident from table – 6.2 that a large magnetic frustration factor of 11.6 has been observed in

YMGO_vacu compound, larger than that observed in unsubstituted YMO compound. However, YMGO_O_2 compound does not show such magnetic frustration. So, it is clear that, oxygen content in these compounds plays an important role in the magnetic interactions.

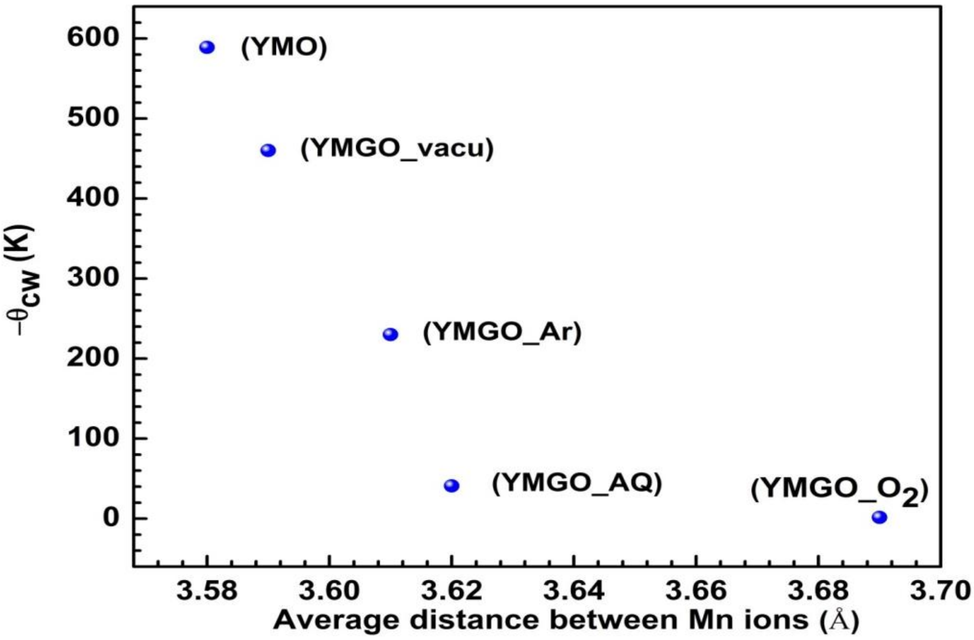

Figure 6.9: Curie-Weiss temperature obtained for polycrystalline YMO and YMGO compounds and Mn inter-atomic distances in respective compounds obtained from Rietveld-refinement.

6.3.2.2 Field-dependent magnetization

Figure 6.10 represents isothermal magnetization as a function of applied magnetic field (M-H). Measurements have been carried out on polycrystalline YMGO_AQ, YGMO_Ar, YMGO_vacu and YMGO_O_2 compounds at 5 K in the field span of ± 50 kOe. A linear increase in magnetization up to the highest applied field of 50 kOe without any hysteresis has been observed in YMGO_Ar, YMGO_vacu and YMGO_AQ compounds, indicating a typical antiferromagnetic behavior. However, a non-linear behavior and tendency of magnetization to saturate in high field region has been observed in YMGO_O_2 compound, as expected of a paramagnetic material. Its paramagnetic response has also been confirmed by CW fit to M-T data (see figure 6.7).

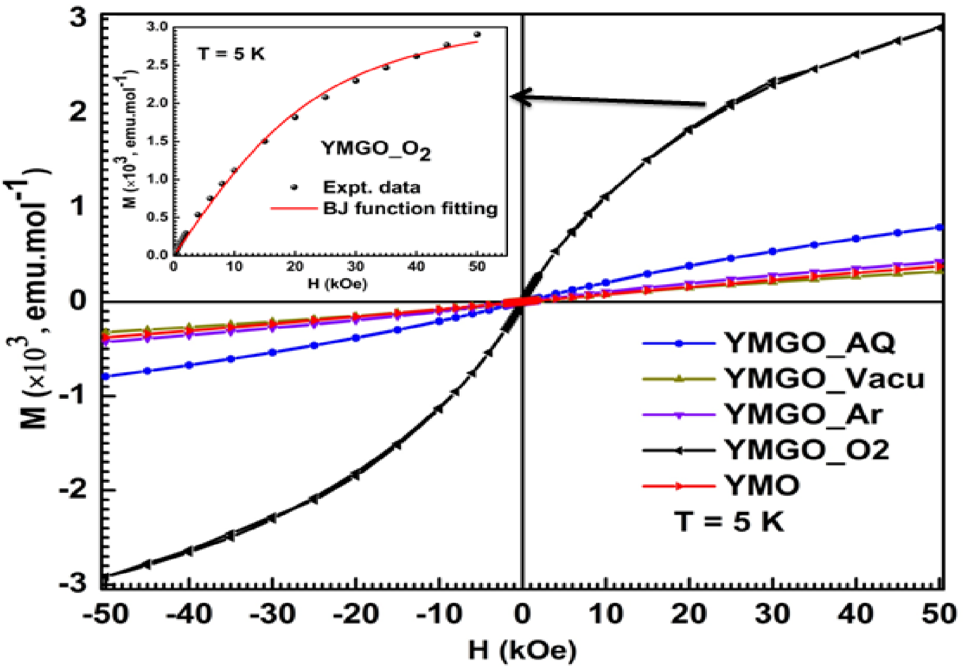

Figure 6.10: Isothermal magnetization as a function of applied magnetic field (M-H) measured on polycrystalline YMO and YMGO compounds at 5 K. Inset shows Brillouin function fitting to virgin magnetization data for YMGO_O$_2$.

The field dependent virgin magnetization data of YMGO_O$_2$ measured at 5 K has been analyzed by fitting to the Brillouin (BJ) function [146] shown below in equation – 6.3:

$$M = M_s\left[\frac{2J+1}{2J}Coth\left(\frac{2J+1}{2J}x\right) - \frac{1}{2J}Coth\left(\frac{x}{2J}\right)\right] \qquad (6.3)$$

where $M_s = NgJ\mu_B$ is the saturation magnetization associated with paramagnetic Mn moments, $x = {}^{gJ\mu_B H}/_{K_B T}$, K_B, N, J and g are the Boltzmann constant, number of Mn moments, angular momentum quantum number and Landé g-factor respectively. The shape of virgin magnetization curve depends strictly on J value whereas M_s depends on both J and N. A satisfactory fitting of virgin M-H data to BJ function gives J ~ 4.5 and g ~ 1.45, and N ~ 5.362×10^{22}. The N value obtained is one order of magnitude less than the expected value (4.035×10^{23}) and J value is should be zero for Mn^{3+}. The unphysical values of J and N

indicate that field-dependent magnetization deviates from paramagnetic behavior represented by BJ function, probably due to significant contribution to magnetization from excess oxygen.

6.4 Conclusion

Polycrystalline compounds of YMGO have been prepared following solid-state reaction method under different annealing atmospheres. Rietveld-refinement of their PXRD patterns confirms the formation of hexagonal crystal structure with ‘$P6_3cm$’ space group symmetry, along with the presence of a small amount (< 5%) of Mn free impurity phase $Y_3Ga_5O_{12}$ in all the compounds. Temperature-dependent magnetization shows an antiferromagnetic transition at T_N ~ 35 K for YMGO_Ar and YMGO_vacu. However, we have not observed such a magnetic transition in case of YMGO_AQ and YMGO_O_2. A μ_{eff} ~ 4.88 μ_B has been observed for YMGO_Ar and YMGO_vacu which is close to the expected moment (4.90 μ_B) associated with Mn^{3+} ($3d^4$). However, μ_{eff} of YMGO_O_2 indicates that Mn ions are perhaps in mixed valence state of Mn^{3+} and Mn^{4+}. At 5 K, a linear response of magnetization against field without any tendency of saturation has been observed upto the maximum applied field of 50 kOe for YMGO_AQ, YMGO_Ar and YMGO_vacu indicating an antiferromagnetic interaction in these compounds. However, a typical paramagnetic response of magnetization has been observed in case of YMGO_O_2. Assuming that oxygen content in YMGO compounds prepared under different annealing atmospheres would be different, the significant changes in structural and magnetic properties discussed above confirm that oxygen content plays an important role on physical properties of these compounds.

In the following chapter, we have described the appearance of ferromagnetism along with magnetoelectric coupling in (Gd, La) co-substituted polycrystalline $BiFeO_3$.

Chapter 7

Study of Magneto-electric Behaviour of Polycrystalline La and Gd co-substituted $BiFeO_3$

7.1 Introduction

Multiferroic materials exhibiting more than one ferroic order parameter in the same phase [152, 245] have attracted a noticeable attention in last few years due to their puzzling physical properties [246, 247, 233]. Besides, the rich fundamental physics behind the origin of confounded properties can lead to their utilization as electronic memory devices, switches, magnetic field sensors etc. [39, 248 - 250].

A fundamental requirement to produce localized magnetic moments in RMO_3 (R = Rare-earth cations, M = Transition-metal cations) is the presence of unpaired electron(s) in the outer *d* orbital of M atom. On the other hand, in such cases, the repulsive Coulomb interaction between M ions is stronger than any energy gain from chemical bond formation with oxygen and hence off centering of transition metal ions to lead to ferroelectricity is highly unlikely.

Consequently, the mutual exclusion of ferroelectricty and magnetism makes multiferroic materials scarce [46]. Nevertheless, there is one class of multiferroic materials which show magneto-electric (ME) coupling, i.e., magnetism in those materials can be controlled by external electric field and vice-versa [152, 46]. Most of the multiferroic materials available till now show ferroelectric Curie temperature (T_c) far above room temperature (RT) whereas magnetic ordering takes place far below RT, which limits their practical utility at RT.

$BiFeO_3$ is a potential candidate in RMO_3 family of single phase multiferroic materials with ferroelectric Curie temperature (T_c) ~ 1103 K [154] and anti-ferromagnetic N’eel temperature

(T_N) ~ 643 K [153]. It stabilizes in trigonal structure with '*R3c*' space group (SG no.161) [251, 155]. The ferroelectricity in this compound is associated with Bi $6s^2$lone pair of electrons [252], whereas weak magnetization associated with canted moments emanates from unpaired electrons of Fe^{3+} ion [253]. The spiral modulated spin structure (SMSS) of Fe^{3+} ions possesses an incommensurate long wavelength of 620 Å, due to which the macroscopic magnetization gets annulled [155] and the linear ME effects is not observed [248, 254]. Besides, the preparation of single phase $BiFeO_3$ is challenging due to the formation of highly stable impurity phases of Bi variants [92]. These drawbacks associated with $BiFeO_3$ impede the functional applications. In order to overcome these problems, several attempts have been made in termsof doping with rare-earth and/or transition metal ions at Bi and/or Fe sites [183, 255 - 265]. For example, Vikash Singh et al have discussed the appearance of weak-ferromagnetism on the basis of structural phase transition from Rhombohedral to Orthorhombic structure in Pr and Ti co-substituted $BiFeO_3$ [262], while Khomchenko et al have reported weak-ferromagnetism and multiple structural phase transformations, $R3c \rightarrow Pn21a \rightarrow Pnma$ in $Bi_{1-x}Gd_xFeO_3$ for different Gd concentrations [261]. Reetuet al have observed a reduced conductivity and enhancement in magnetization in La and Ti substituted $BiFeO_3$ [263] and a report from Rao et al mentions an improvement of magnetic and ferroelectric behaviour in polycrystalline Nd and Sc co-substituted $BiFeO_3$ [153]. Further, Palkaret al have shown the appearance of ferromagnetic ordering and variation of dielectric properties with magnetic field at room temperature in modified $BiFeO_3$ system [183] while Park et al have discussed the impact of Ho and Ni co-substitution on the structural and magnetic properties of $BiFeO_3$ [265]. Most of the previous studies show the appearance of weak ferromagnetism on substitution by transition element at Fe site. Despite a large spread of experimental studies on multiferroic materials, the reports on ferromagnetism, ferro-electricity and ME coupling at room temperature are extremely meagre, which motivated us to look for multiferroic materials with ME coupling at room temperature in variants of $BiFeO_3$ system.

In this chapter, we describe our studies on polycrystalline Gd and La co-substituted $BiFeO_3$ in terms of structural, magnetization, polarization and ME coupling measurements. We have used f-block element (Gd) to enhance magnetic properties and 10 atom% La was used to suppress the formation of impurity phases [183]. Our experimental observations show the appearance of ferromagnetism and ferroelectricity in $Bi_{0.85}Gd_{0.05}La_{0.1}FeO_3$ compound with ME coupling at room temperature. The detailed investigations of magnetic and electric properties of $Bi_{0.9-x}Gd_xLa_{0.1}FeO_3$ (x = 0.0, 0.05) have been discussed below.

7.2 Experimental details

Polycrystalline $BiFeO_3$ and $Bi_{0.9-x}Gd_xLa_{0.1}FeO_3$ (x = 0.00 and 0.05) have been prepared using the conventional solid-state reaction method. Stoichiometric amounts of high purity (99.99%) oxides of Bi_2O_3, Fe_2O_3, Gd_2O_3 and La_2O_3 have been mixed thoroughly and subsequently calcined in an alumina crucible at 723 K for 8 hours using a box-furnace. The calcined mixture was pelletized and sintered at 1083 K repeatedly, for 10 hours at a time, with intermediate grinding for homogenization. The pellets were ground into fine powder and used for further characterization and measurements.

Phase purity of the samples has been confirmed by X-ray diffraction (XRD) technique using "Rigaku Diffractometer" with Cu-K_α ($\lambda = 1.5406$ Å) radiation. The XRD measurements were carried out on polycrystalline $BiFeO_3$ variants in the 2θ range of 10° - 70° at room temperature (RT) and are shown in figure 7.1. The oxidation states of Y, Mn and Ga were measured by X-ray Photoelectron Spectroscopy (XPS) using MgK_α (1253.6 eV) X-ray source and a DESA-150 electron analyzer (M/s. Staib Instruments, Germany). The binding energy scale was calibrated with C-1s line at 284.8 eV. The analyser was operated at 40 eV pass energy and the chamber pressure during measurements was ~ 7 x 10^{-9} Torr. The XPS spectra were analysed using XPSPEAK41 software. Raman Spectra were recorded at room temperature using Jobin-Yvon HR-800 Evolution spectrometer with 532 nm laser and 600 rulings/mm grating, which gives a resolution of 1.5 cm^{-1} per pixel. Measurements of the magnetic moment as a function of temperature (T) and applied field (H) were performed using Superconducting Quantum Interference Device (SQUID) magnetometer (M/s. Quantum Design, model MPMS) in the temperature range 5 K– 300 K under applied dc magnetic fields up to ± 50 kOe. Zero field cooled (ZFC) and field cooled (FC) processes were used to measure the temperature dependence of magnetization under different dc magnetic fields. In ZFC measurement, the sample was cooled from room temperature down to 5 K in zero applied field and magnetization data was collected while the sample was being heated to room temperature in the presence of an external dc field. Thereupon the FC measurements were carried out while cooling the sample to the lowest temperature in the same external field. Isothermal magnetization measurements were carried out over a wide temperature range of 5 K to 300 K. The polarization and leakage current density were measured on circular pellet of thickness less than 1 mm using aixACCT's TF analyser 2000. Both side of pellets were coated with Electro Lube's conducting Ag paint and dried at room temperature. The ME coupling measurements were done using a homemade instrument described in chapter 2.

7.3 Results and discussion

7.3.1 X-ray diffraction

The crystal structure of polycrystalline $BiFeO_3$ and $Bi_{0.9-x}Gd_xLa_{0.1}FeO_3$ samples (x = 0.00 and 0.05) has been investigated using XRD patterns recorded at RT. All the observed peaks can be indexed to rhombohedral structure with '*R3c*' space group. We have not observed the impurity phase $Bi_2Fe_4O_9$reported by many others [153, 261 - 263, 266].

Table 7.1: Structural parameters obtained from Rietveld-refinement of XRD patterns of polycrystalline $BiFeO_3$ and $Bi_{0.9-x}Gd_xLa_{0.1}FeO_3$ (x = 0.00 and 0.05) compounds.

Parameter	Ref. [267]	$BiFeO_3$	$Bi_{0.9}La_{0.1}FeO_3$	$Bi_{0.85}Gd_{0.05}La_{0.1}FeO_3$
$a_{hexa} = b_{hexa}$ (Å)	5.5876(3)	5.5776(2)	5.5790(7)	5.5770(2)
c_{hexa} (Å)	13.867(1)	13.8667 (4)	13.822(2)	13.8331(7)
V (Å^3)	374.9(3)	373.59(2)	372.60(3)	372.59 (9)
Fe – O(1,2) (Å)	2.120(3),1.940(2)	2.1256(2),2.1053(3)	2.0272(2),2.0272(3)	2.0718(6),1.9828(5)
O1 – Fe – O2 (°)	167.2(6)	165.5(2)	166.6(5)	169.3(3)
χ^2	--	2.9	3.5	2.1

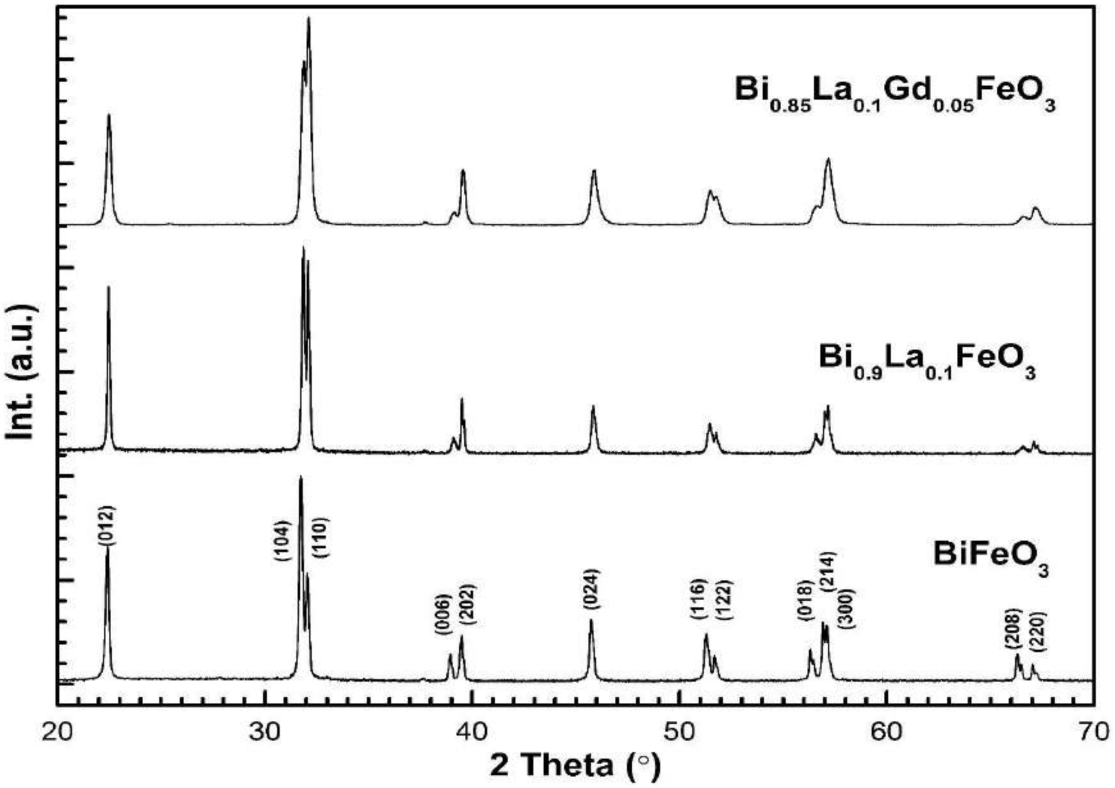

Figure 7.1: Powder X-ray diffraction pattern of polycrystalline $BiFeO_3$ and $Bi_{0.9-x}Gd_xLa_{0.1}FeO_3$ (x = 0.0, 0.05) recorded at room temperature (λ = 1.5406 Å). Peak indexing is associated with orthorhombic-structure of *R3c* space group.

Besides, no signature of starting materials like Bi_2O_3, Fe_2O_3, or extraneous products have been detected within the resolution of XRD measurement, indicating that the solid-state reaction was complete amongst precursor materials, clearly attesting to high quality of the samples. The XRD patterns have been analyzed using Fullprof [191, 111] software. Their refinement, shown in figure 7.2, was carried out considering'*R3c*' space group for all the cases and the reference is taken from ICSD data base with collection code 15299 [267]. A good agreement between observed and calculated patterns has been noted for all the compounds. The lattice parameters, bond lengths, bond angles and unit cell volume obtained from refinement have been tabulated in table – 7.1. It is clear that axis 'a' hardly changes whereas the axis 'c' decreases significantly upon Gd and La substitution, which can be

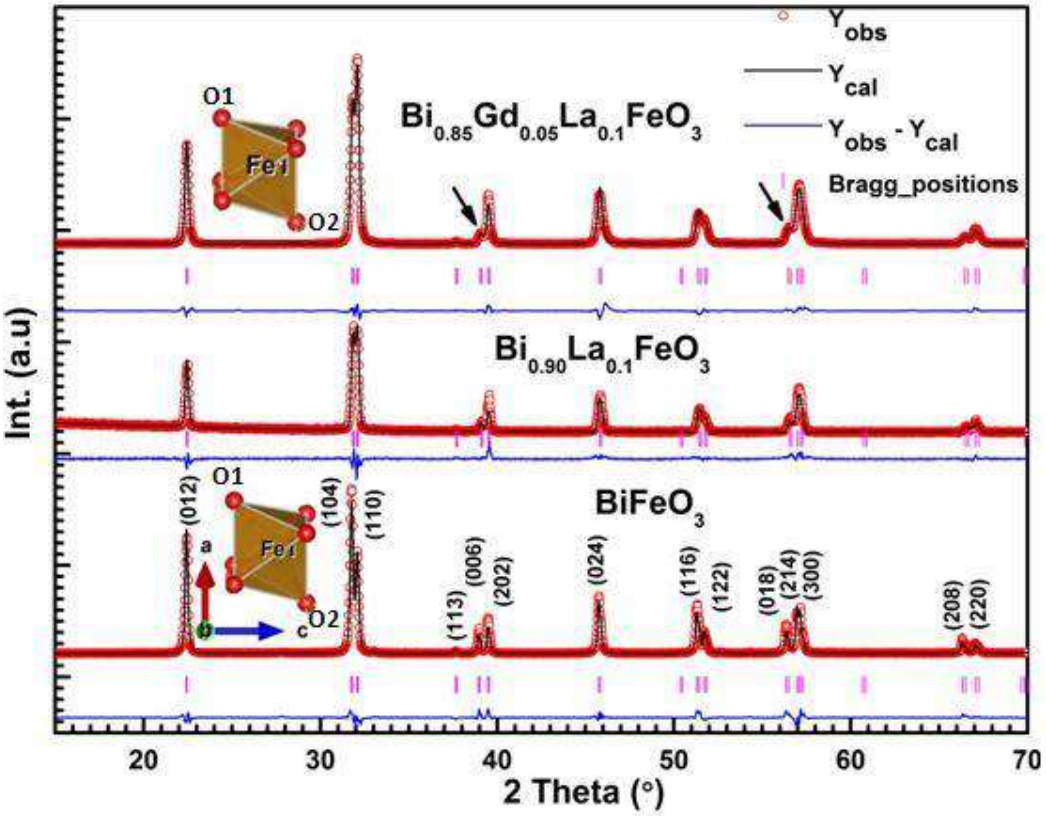

Figure 7.2: Rietveld-refinement of XRD patterns of polycrystalline $BiFeO_3$ and $Bi_{0.9-x}Gd_xLa_{0.1}FeO_3$ (x = 0.00 and 0.05) compounds recorded at ambient temperature. The arrows indicate (006) and (018) peaks. A visualization of FeO_6 octahedron obtained from refined data is also presented.

ascribed to the smaller ionic radii of Gd^{3+} and La^{3+} ions in comparison to Bi^{3+} ion. Besides, O1 – Fe – O2 angles and Fe – oxygen distances in FeO_6 octahedron (shown in figure 7.2) are noted to change with substitution. A careful observation of experimental XRD patterns reveals that the intensity of (006) and (018) peaks (shown by arrow marks in figure 7.2) diminishes, indicating that the rhombohedral distortion is reduced with substitution. A similar observation has been reported in La modified $BiFeO_3$ [256]. The orientation of FeO_6 octahedron viewed along ‘b’ axis drawn using Rietveld-refined XRD data has been shown in figure 7.2. Since Rietveld-refinement in the present case shows a good agreement between calculated and observed intensities for all the compounds using ‘*R3c*’ symmetry, we infer that atomic substitutions did not lead to phase transitions. However, Shan-Tao Zhang et al and many others have reported substitution induced structural phase transformations in polycrystalline $BiFeO_3$ [257, 268, 269]. A visualization of unit cell structure extracted from Rietveld-refinement has been shown in figure 7.3. The illustration was made using VESTA software [193].

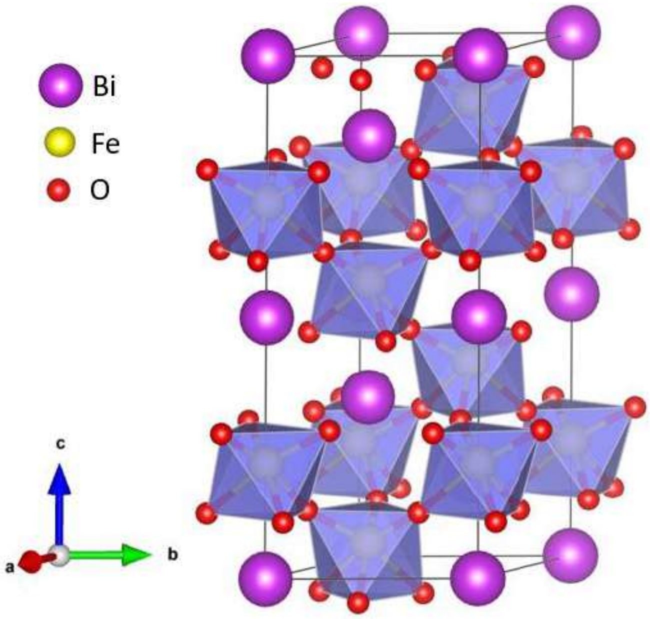

Figure 7.3: Schematic view of unit-cell of $BiFeO_3$ drawn using experimental crystallographic information file extracted from Rietveld-refinement.

7.3.2 X-ray photoemission spectroscopy

The presence of various elements and their oxidation states have been investigated using X-Ray Photoelectron Spectroscopy (XPS) studies. Figure 7.4 shows the elemental survey spectrum of $Bi_{0.85}Gd_{0.05}La_{0.1}FeO_3$. The binding energies of Bi $4f_{7/2}$ and Bi $4f_{5/2}$ in $BiFeO_3$ have been observed at 158.60 eV and 164.06 eV whereas spin-orbit doublets have been observed for Fe $3p_{3/2}$ and Fe $3p_{1/2}$ in the range 709.5 eV –711.7 eV and 723.2 eV – 725.3 eV respectively.

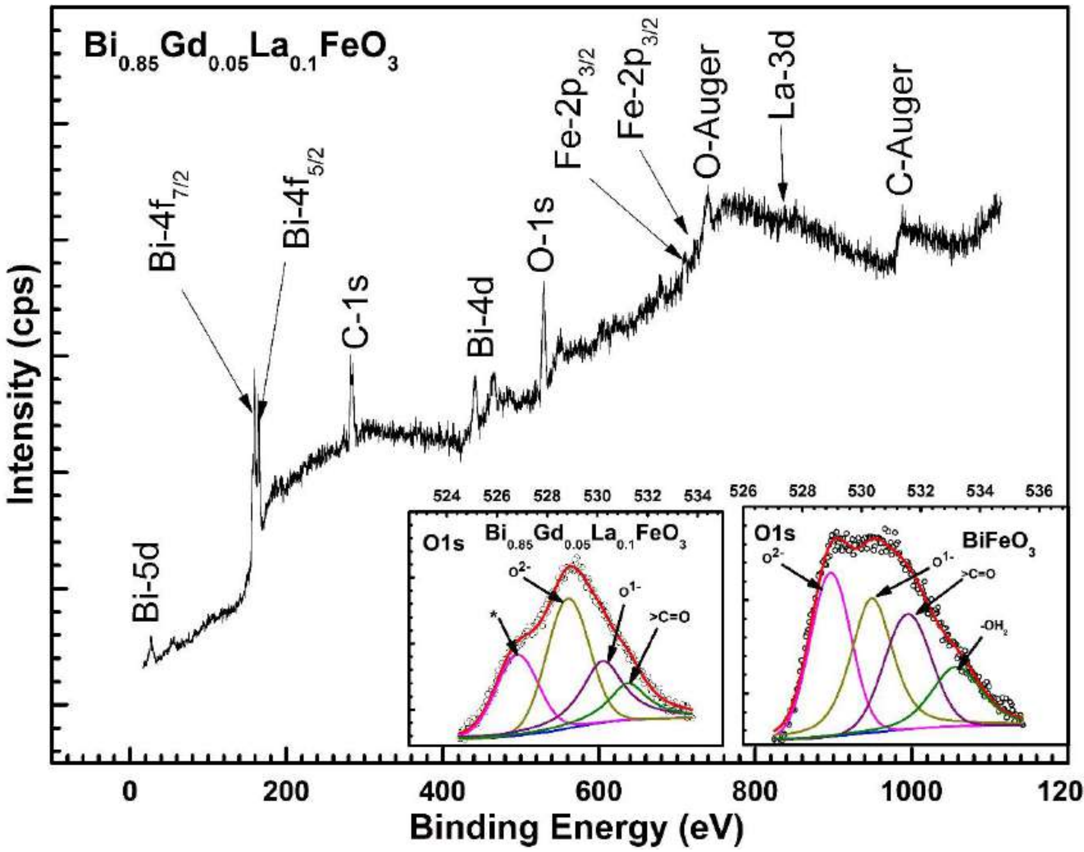

Figure 7.4: X-ray photoelectron spectroscopy survey spectrum of polycrystalline $Bi_{0.85}Gd_{0.05}La_{0.1}FeO_3$ recorded at room temperature. Insets show the O 1s spectra of $BiFeO_3$ and $Bi_{0.85}Gd_{0.05}La_{0.1}FeO_3$.

Similar binding energies of Bi 4f and Fe 3p electrons have been reported in the case of $Bi_{0.85}Gd_{0.05}La_{0.1}FeO_3$ compound and our finding agrees well with previously reported values [270]. A peak has been observed at ~ 283.56 eV due to C 1s as shown figure 7.4, which is expected and was used for energy calibration. Multiple Gassuian-Lorentzian fitting of O 1s spectrum of BiFeO$_3$results in peaks at 529.0 eV and 530.3 eV associated with O^{2-} and O^{1-} respectively, as shown in right inset of figure 7.4. The ratio of areas under the fitted curves associated with O^{2-} and O^{1-} is 0.97 which is close to 1. This indicates that the average valency of O is nearly -1.5, amounting to significant oxygen vacancies in BiFeO$_3$ sample. A similar observation has been made in other perovskite oxides like BaTiO$_3$ [271]. Two additional peaks observed at 531.5 eV and 533.0 eV are due to surface hydroxyl and absorbed water [272]. It should be noted that a peak is observed at ~ 526 eV while de-convoluting the O 1s spectra of Gd-doped samples, which is unrealistic because the lowest binding energy possible for oxygen is 528 eV [118, 273]. A similar observation was reported in DyBa$_2$Cu$_3$O$_{6+\delta}$ [274]. The binding energies of O^{2-} and O^{1-} in doped compounds are noted to be 529.0 eV and 530.2 eV and the ratio of their areas is 1.5, indicating an improvement in oxygen stoichiometry.

7.3.3 Magnetization studies

7.3.3.1 Temperature dependent magnetization

The zero-field cooled (ZFC) and field-cooled (FC) magnetization measurements as a function of temperature (T) of polycrystalline BiFeO$_3$ under a dc applied field of 100 Oe are shown in figure 7.5. The ZFC / FC magnetization of unsubstituted BiFeO$_3$ decreases with decreasing temperature down to ~ 100 K, as expected of an antiferromagnetic material. A bifurcation of ZFC and FC magnetization is seen below ~ 100 K and then an increase with decreasing temperature. The increase is sharper in case of FC magnetization, whereas ZFC magnetization increases at a slower rate. The Fe moments in BiFeO$_3$ undergo an anti-ferromagnetic transition below T$_N$(Fe^{3+}) ~ 643 K [153]. At ambient temperature, the magnetic structure associated with Fe^{3+} sub-lattice in BiFeO$_3$ can be represented by helical orientation along [110] direction [266, 275]. They couple antiferromagnetically between adjacent planes, which is the G-type antiferromagnetic arrangement and ferromagnetically within the pseudo-cubic (111) planes [36, 91, 276, 277]. Canting of anti-ferromagnetic sub-lattices gives raise to weak ferromagnetism, but helical arrangement of Fe^{3+} moments leads to annulment of macroscopic magnetization and also inhabits the observation of linear ME coupling [45]. Similar temperature dependence and tiny magnetization have been reported in nanocrystalline and single-crystal $BiFeO_3$ by Vijayanand et al [278] and Singh et al [279].

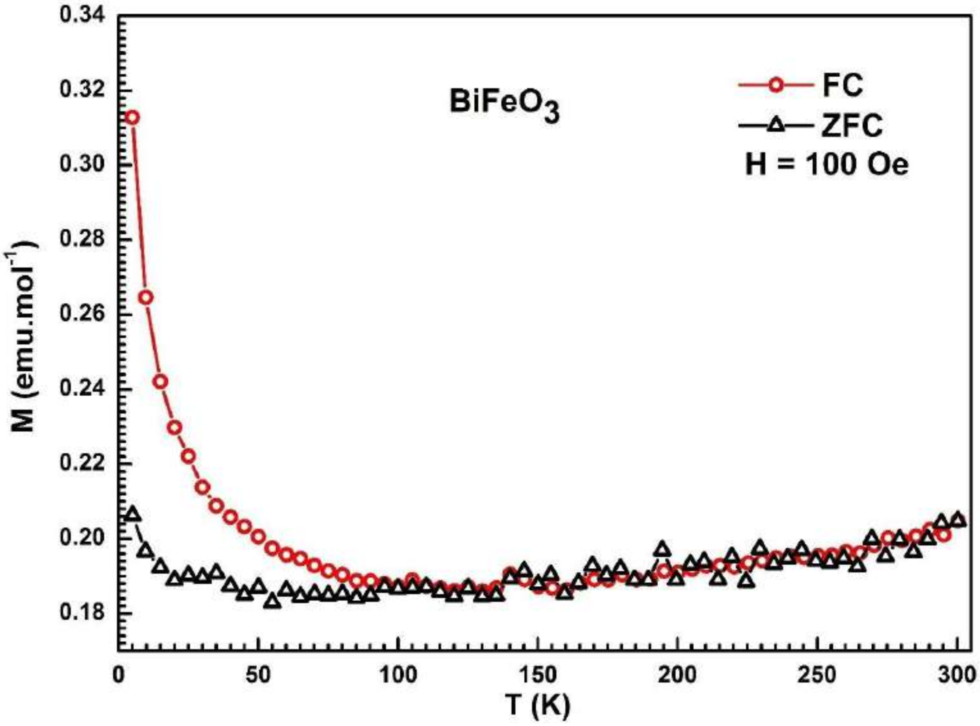

Figure 7.5: ZFC and FC magnetization as a function of temperature, M(T) of polycrystalline $BiFeO_3$ measured under a dc field of 100 Oe.

Figure 7.6 shows M-T of polycrystalline $Bi_{0.9}La_{0.1}FeO_3$ measured in the temperature range 5 K – 300 K under 100 Oe and 1000 Oe. An identical behaviour of magnetization with temperature has been noted in both the cases. Both the ZFC and FC magnetization decrease with decreasing temperature with an abrupt change at ~ 265 K. The anomaly

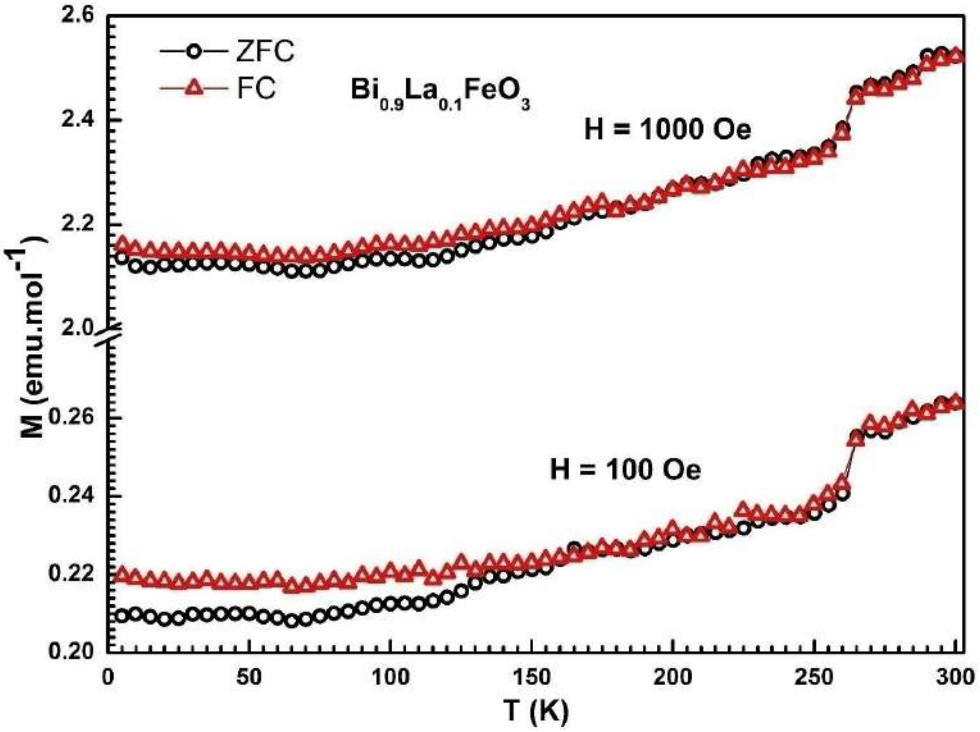

Figure 7.6: ZFC and FC magnetization as a function of temperature, M(T), of polycrystalline $Bi_{0.9}La_{0.1}FeO_3$ measured under dc fields of 100 Oe and 1000 Oe.

observed in M-T could be associated with a negligible amount of $Bi_2Fe_4O_9$ [280] present in the sample, not evident in its XRD pattern (see figure 7.1)

In order to enhance magnetization, we have studied Gd and La co-doped bismuth ferrite samples. Here, 10% La was used to supress the formation of impurity phases as noted by many others [261, 262, 266]. The temperature-dependent ZFC and FC magnetization for polycrystalline $Bi_{0.85}Gd_{0.05}La_{0.1}FeO_3$ has been shown in figure 7.7. The measurements have been carried out under fields of 100 Oe and 500 Oe. A significant enhancement in magnetization (~ 50 times that of polycrystalline $BiFeO_3$measured under 100 Oe) has been noted, probably due to the paramagnetic contribution of Gd^{3+} ions. The irreversibility between ZFC and FC magnetization at ~ 300 K indicates the presence of a magnetic ordering at ambient temperature, which could be associated with the destruction of helical arrangement of Fe moments. Besides, FC magnetization being lower than ZFC magnetization

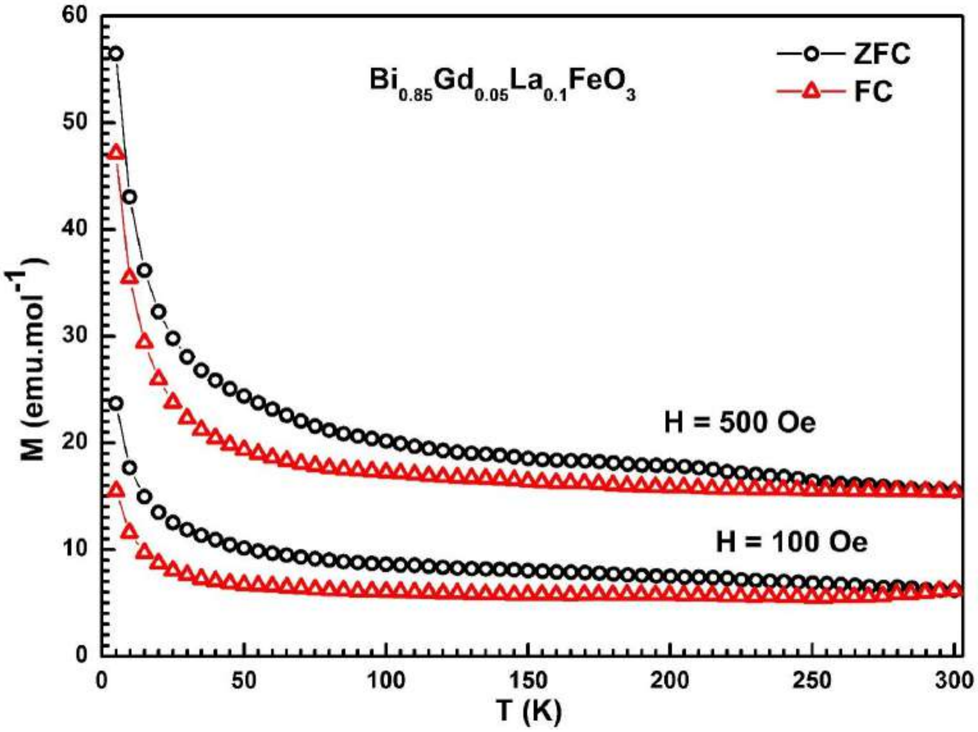

Figure 7.7: ZFC and FC magnetization as a function of temperature, M(T), of polycrystalline $Bi_{0.85}Gd_{0.05}La0_{.1}FeO_3$ measured under dc fields of 100 Oe and 500 Oe.

in both 100 Oe and 500 Oe measurements can be attributed to the destruction of the helical arrangement of Fe moments and the interplay of competitive magnetic interactions involving arrested Fe moments around Gd ions and the rest of the Fe moments aligned antiferromagnetically [281]. A similar trend of ZFC and FC magnetization is reported in nanocrystalline $NiFe_2O_4$ [282, 283].

7.3.3.2 Field dependent magnetization

Figure 7.8 represents the isothermal magnetization measurements as a function of applied field, M(H), carried out at room temperature on polycrystalline $BiFeO_3$ and $Bi_{0.9-x}Gd_xLa_{0.1}FeO_3$ (x = 0.00 and 0.05) upto a maximum applied field of ±50 kOe. A linear response (typical of an antiferromagnetic material) with an insignificant remnant magnetization (M_r ~ 0.12 emu.mol^{-1}) is observed for un-doped $BiFeO_3$, in line with literature

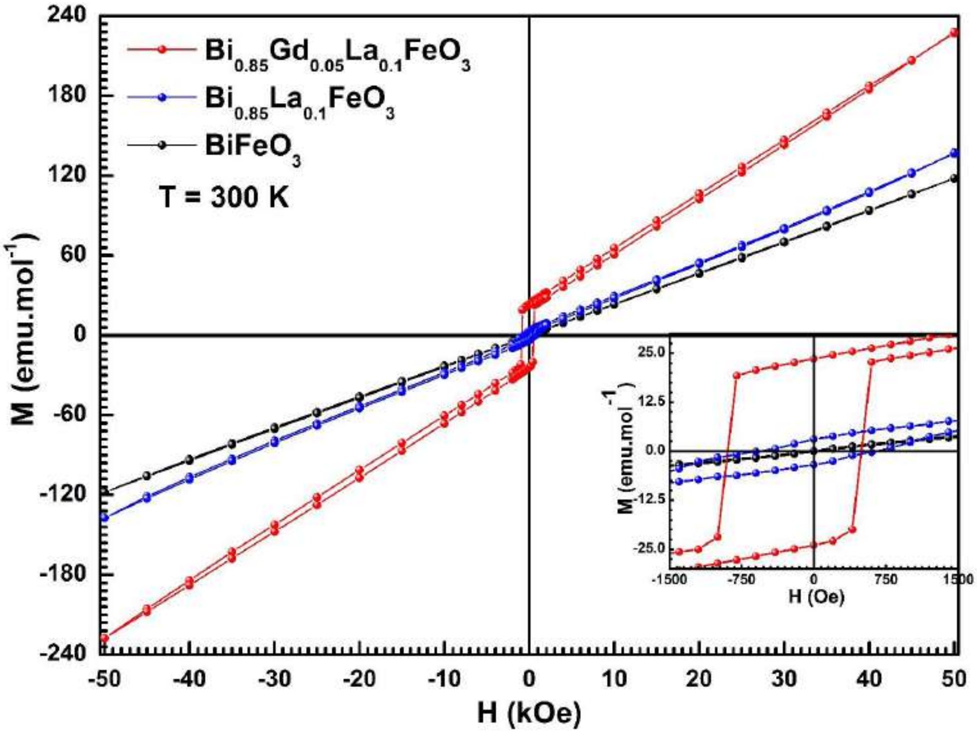

Figure 7.8: Field dependent magnetization M(H) curves of polycrystalline $BiFeO_3$ and $Bi_{0.9-x}Gd_xLa_{0.1}FeO_3$ (x = 0.00 and 0.05) measured at room temperature. Inset shows the magnetified view near zero field.

reports [256, 257], although a weak ferromagnetic behaviour is expected on account of Dzyaloshinskii-Moriya (DM) interaction [76, 77]. In case of $Bi_{0.9}La_{0.1}FeO_3$, a small hysteresis loop is seen near-zero field region along with M_r ~ 3 emu.mol^{-1} which may be due to $Bi_2Fe_4O_9$ impurity [280]. However, a large hysteresis with a significantly enhanced M_r value of ~ 23.6 emu.mol^{-1} has been noted in case of $Bi_{0.85}Gd_{0.05}La_{0.1}FeO_3$. The advent of a large M_r could be attributed to the destruction of helical structure of Fe^{3+} moments and their plausible freezing around Gd^{3+} ions.

A shift of hysteresis loop towards negative field axis has been observed confirming the presence of an exchange bias (EB) in $Bi_{0.85}Gd_{0.05}La_{0.1}FeO_3$. It also shows a high coercive field H_c of ~ 705 Oe, which is unlikely to originate from domain wall pinning since a typical coercive field for such a pinning is less than 300 Oe [284], but probably arises due to magnetic anisotropy. It is seen that a majority of multiferroic materials show EB effect at low temperatures (< 100 K) making them less useful to applications, while the existence of EB effect in $Bi_{0.85}Gd_{0.05}La_{0.1}FeO_3$ at room temperature could, in principle, lead to applications [285, 286].

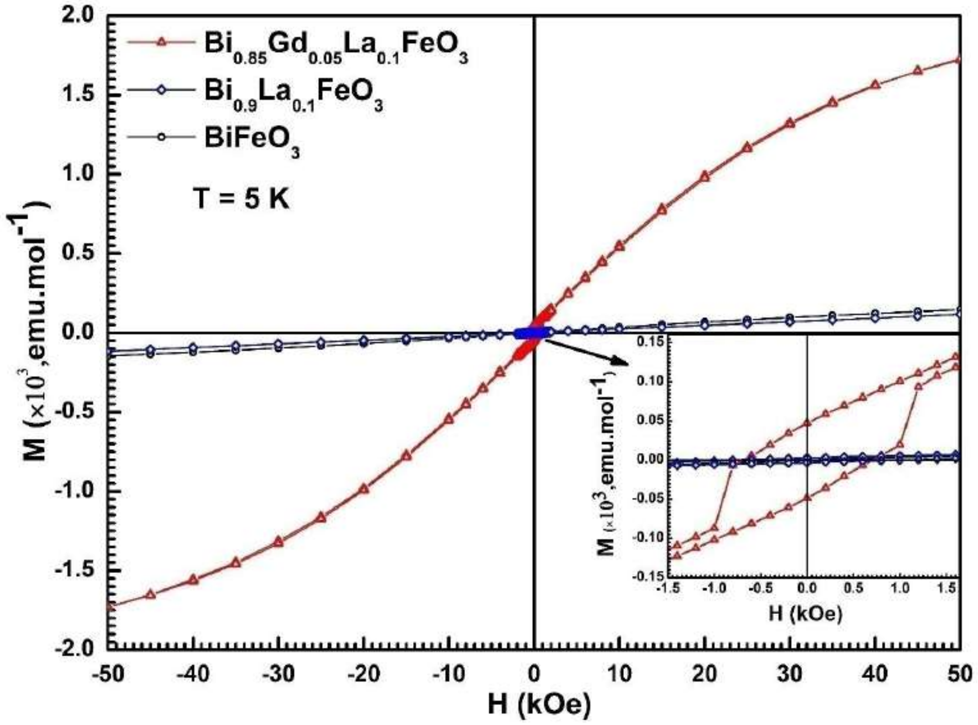

Figure 7.9: Field dependent magnetization, M(H), of polycrystalline $BiFeO_3$ and $Bi_{0.9-x}Gd_xLa_{0.1}FeO_3$ (x = 0.00 and 0.05) measured at 5 K. Inset shows the magnified view near zero field region.

Figure 7.9 presents the M-H curves recorded at 5 K for polycrystalline $BiFeO_3$ and $Bi_{0.9-x}Gd_xLa_{0.1}FeO_3$ (x = 0.00 and 0.05). A linear response of magnetization with applied magnetic field is observed for $BiFeO_3$ and $Bi_{0.9}La_{0.1}FeO_3$ indicating that their magnetic interactions are antiferromagnetic in nature. However, a non-linear response of magnetization noted in $Bi_{0.85}Gd_{0.05}La_{0.1}FeO_3$, with tendency to saturate in high field region, could be attributed to paramagnetic behaviour of Gd moments. A hysteresis loop seen near-zero field region in M(H) response of $Bi_{0.85}Gd_{0.05}La_{0.1}FeO_3$ is attributed to the ferromagnetic component arising from its Fe sub-lattice.

Assuming that the ferromagnetic component saturates in high field region (> 10 kOe), an attempt was made to fit the virgin magnetization data with Brillouin function as described below:

$$M = M_F + M_s \left[\frac{2J+1}{2J}\coth\left(\frac{2J+1}{2J}x\right) - \frac{1}{2J}\coth\left(\frac{x}{2J}\right)\right] \qquad (7.1)$$

where M_F is the field-independent contribution to magnetization due to canted Fe^{3+} sub-lattice which is assumed to saturate above 10 kOe, $x = gJ\mu_B H/K_B T$, and $M_s = NgJ\mu_B$ is the saturation magnetization due to paramagnetic Gd^{3+} moment, K_B is the Boltzmann constant, N is the number of Gd^{3+} moments per unit mass of the sample, J and g are the angular momentum quantum number and Landau factor (assumed to be 2; spin contribution alone).

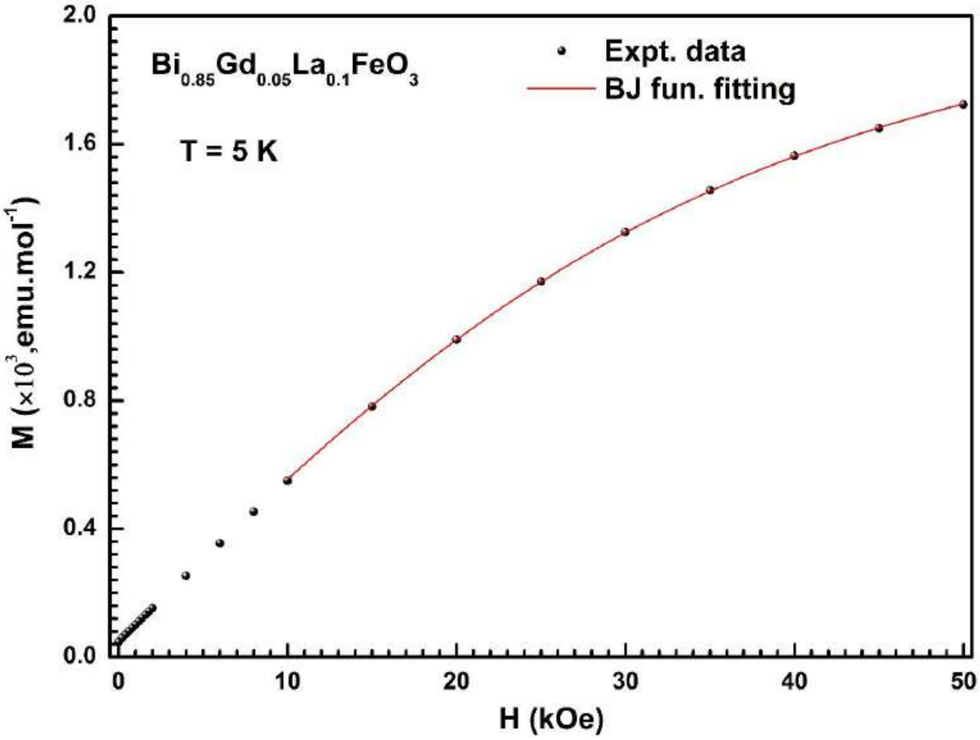

Figure 7.10: Brillouin function fitting to virgin magnetization curve for polycrystalline $Bi_{0.85}Gd_{0.05}La_{0.1}FeO_3$ measured at 5 K.

A satisfactory fitting (shown in figure 7.10) results in N ~ 6.25×10^{22}and J ~ 1.8which deviate significantly from the expected values of 3.012×10^{22} and 3.5 for Gd^{3+} spin. Also, M_F value obtained (~ 34.78 emu.mol^{-1}) is different from spontaneous magnetization of 47.42 emu.mol^{-1}. These values indicate that Gd moments do not follow Brillouin function and hence do not conform to a typical paramagnetic behaviour. This could possibly be due to magnetic interactions amongst Gd moments and with Fe sub-lattice.

7.3.4 Polarization vs Electric field (P-E) measurements

Being room temperature ferroelectric materials, we have studied polarization (P) of polycrystalline $BiFeO_3$ and $Bi_{0.85}Gd_{0.05}La_{0.1}FeO_3$ as a function of electric field (E) at ambient temperature. Polycrystalline samples of $BiFeO_3$ usually exhibit high electrical leakage due to oxygen vacancies, leading to difficulties in obtaining saturated polarization hysteresis loop [287 - 289].

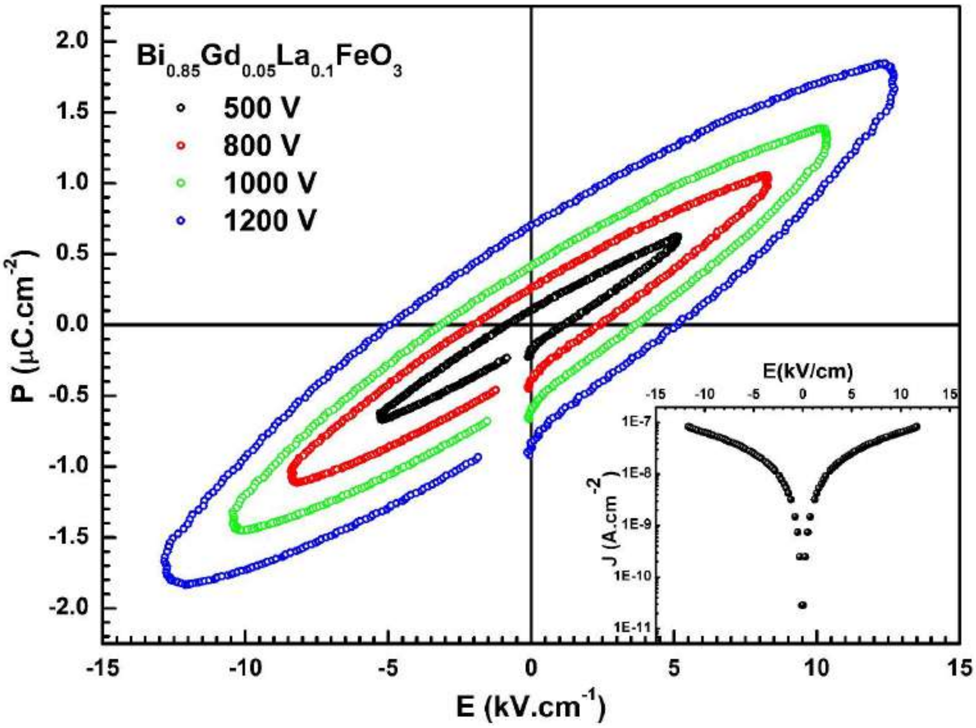

Figure 7.11: Polarization hysteresis (P - E) loops of polycrystalline $Bi_{0.85}Gd_{0.05}La_{0.1}FeO_3$ measured at room temperature at 400 Hz for four different maximum voltages (500, 800, 1000 and 1200 V). Inset shows the current density (J) vs electric field (E) plot of $Bi0._{85}Gd_{0.05}La_{0.1}FeO_3$ compound, demonstrating the enhancement of insulating property with Gd substitution.

However, Gd and La co-substitution makes $BiFeO_3$ more insulating and helps in P-E measurements. Figure 7.11 presents the P-E measurements on polycrystalline $Bi0_{.85}Gd_{0.05}La_{0.1}FeO_3$ performed at ambient temperature. It is evident that an unsaturated polarization has been observed in all the measurements, carried out for different maximum values of the applied electric field. We have observed a maximum polarization (P_m) of ~ 1.8 μC.cm^{-2} at an applied field of ~ 12.5 kV.cm^{-1}, with a remnant polarization (P_r) of ~ 0.7 μC.cm^{-2}. The possible ferroelectric behaviour in $Bi_{0.85}Gd_{0.05}La_{0.1}FeO_3$ could have arisen due to polar displacement of anion and cation sub-lattices relative to each other, and a rotation of the FeO_6octahedraas is evident from XRD pattern [290]. The density functional theory calculations suggest a similar plausible explanation of ferroelectricity in $BiFeO_3$ with '*R3c*' space group [91].

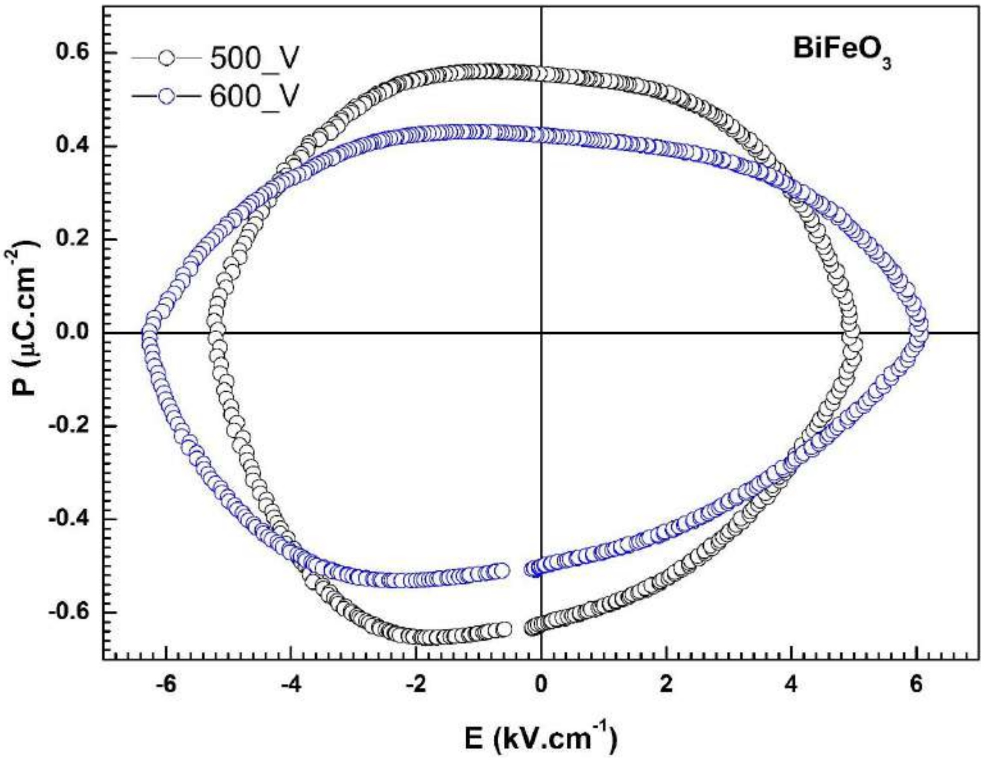

Figure 7.12: Polarization hysteresis (P - E) loop of polycrystalline $BiFeO_3$ measured at room temperature for maximum voltages of 500 V and 600 V.

The values of P_m and P_r obtained for $Bi_{0.85}Gd_{0.05}La_{0.1}FeO_3$ compound compare well with the values reported in the literature for single-phase $BiFeO_3$, namely, 8.9 µC.cm^{-2} and 4 µC.cm^{-2} respectively, for an applied field of 100 kV.cm^{-1} [291]. Non-linear response of polarization with the applied electric field and an increase in P_r with the maximum applied electric field suggest that a higher electric field is required to attain saturation of polarization in $Bi_{0.85}Gd_{0.05}La_{0.1}FeO_3$ compound. The variation of its current density (J) as a function of applied electric field (E) at room temperature is shown as the inset of figure 7.11. The J – E curve shows a symmetric behaviour under positive and negative electric fields.

A significantly less leakage current density and a large resistive behaviour of polycrystalline $Bi_{0.85}Gd_{0.05}La_{0.1}FeO_3$in comparison to unsubstituted $BiFeO_3$ [292, 293] can be attributed to a reduction in oxygen vacancies. Figure 7.12 shows the P-E loop carried out on $BiFeO_3$ for maximum applied voltages of 500 V and 600 V. the observed roundish hysteresis loop is due to a large leakage current which can overshadow the real contribution from reorientation of electrical dipoles [294].

7.3.5 Magnetoelectric coupling (ME) measurements

The coupling between electric and magnetic properties has been studied by measuring magnetic field induced voltage (MIV) across the samples (pellets of polycrystalline samples of thickness less than 1 mm). Figure 7.13 represents the differential MIV, ΔV_{ME} = V(H) -V(0) as a function of applied magnetic field in the range ± 11 kOe measured on a pellet of $Bi0_{.85}Gd_{0.05}La_{0.1}FeO_3$at ambient temperature, where V(H) is the voltage induced across the sample in the presence of H and V(0) is the voltage developed in the absence of H. It is clear from the figure 7.12 that a smooth and non-linear behaviour of ΔV_{ME} with the applied field has been observed. Similar behaviour of MIV has been observed in polycrystalline $BiFe_{1-x}Co_xO_3$ [133] and barium titanate (BTO)-nickel ferrite (NFO) core-shell structure [295]. As the MIV due to ME effect behaves like an odd function (changes polarity on changing field direction) the induced magnetoelectric voltage (V) in the presence of an external dc magnetic field (H) has been analyzed by fitting with the following equation 7.2,

$$V = E.d = \alpha H + \beta H^3 + \gamma H^5 + \delta H^7 + \ldots \qquad (7.2)$$

where the parameters α, β, γ, δ are 1st order, 3rd order, 5th order, and 7th order coupling coefficients and 'd' is the thickness of the sample (pellet).

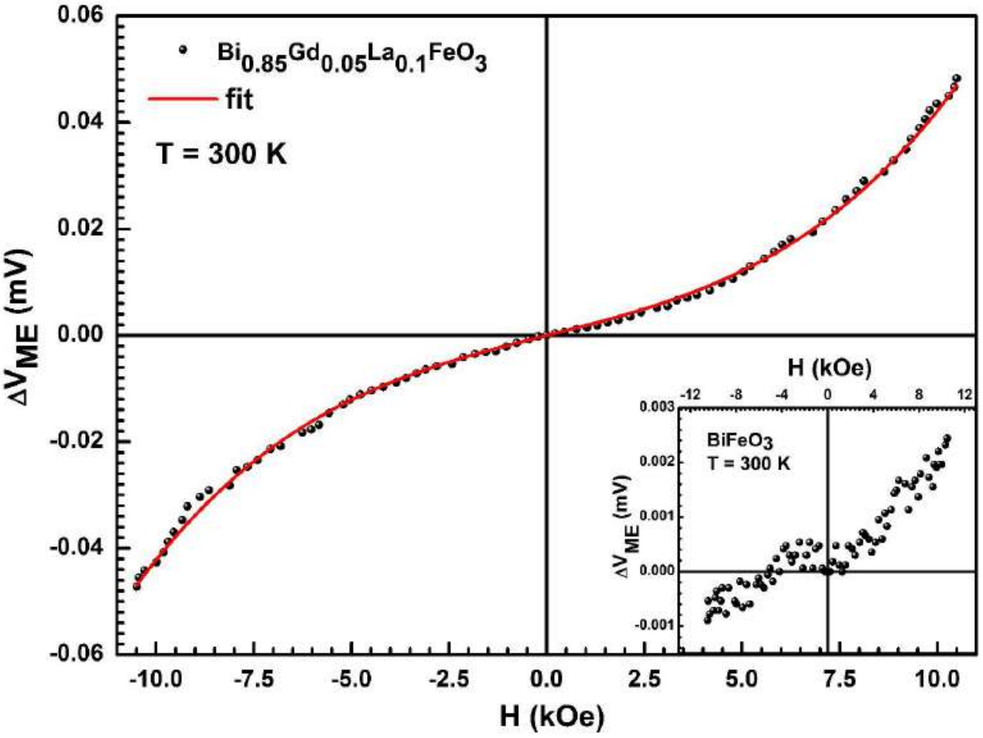

Figure 7.13: dc magnetic field (H) vs magneto-electric voltage (V_{ME}) measurement on polycrystalline $Bi_{0.85}Gd_{0.05}La_{0.1}FeO_3$ at room temperature. The inset shows the same for $BiFeO_3$.

A satisfactory fitting is obtained by using the expression up-to third-order coefficient. The linear ME coupling coefficient ($\frac{\alpha}{d}$) obtained for $Bi_{0.85}Gd_{0.05}La_{0.1}FeO_3$ is ~ 0.022 mV cm^{-1} kOe^{-1}which is smaller than the value reported in $BiFe_{1-x}Co_xO_3$compound [276]. The value of higher-order ME coefficients ($\frac{\beta}{d}$), and ($\frac{\gamma}{d}$)obtained from fitting are ~ 2.55×10^{-5} mV cm^{-1} $kOe^{-3}$and 1.32×10^{-8} mV cm^{-1} kOe^{-5} respectively. The coupling between voltage drop and the applied magnetic field can be understood in terms of oxygen octahedra rotation and polar displacement of cations and anions with respect to centro-symmetric position upon Gd and La co-substitution. The inset of figure 7.13 shows ΔV_{ME} vs H measured on unsubstituted $BiFeO_3$ compound. A scattered and small MIV (~ 10 times smaller than that of$Bi_{0.85}Gd_{0.05}La_{0.1}FeO_3$) is noted in case of $BiFeO_3$, probably due to high leakage current.

7.4 Conclusion

Polycrystalline $BiFeO_3$ and $Bi_{0.9-x}Gd_xLa_{0.1}FeO_3$ (x = 0.00 and 0.05) have been prepared using the solid-state reaction route. Rietveld refinement of room temperature XRD patterns confirms that the compounds crystallize in rhombohedral structure with '*R3c*' space group. The changes in XRD patterns on account of substitution could be associated with a distortion of their crystal structure induced by the rotation of FeO_6 oxygen octahedra, as elaborated in the structural analysis section. A small magnetization has been observed in unsubstituted $BiFeO_3$ which is reconciled in terms of annulment of macroscopic magnetization due to helical antiferromagnetic arrangement of Fe moments. In case of $Bi_{0.85}Gd_{0.05}La_{0.1}FeO_3$, irreversibility between ZFC and FC magnetization and lower FC magnetization in relation to ZFC magnetization have been observed, indicating the presence of magnetic anisotropy. Further, its field-dependent magnetization at room temperature reveals a ferromagnetic behaviour with a significantly enhanced M_r value of ~ 23.6 emu.mol^{-1}, along with the EB effect. The ferromagnetic behaviour has been explained on the basis of destruction of the helical arrangement of Fe moments associated with structural distortion affected by Gd and La co-substitution. P - E measurements on $Bi_{0.85}Gd_{0.05}La_{0.1}FeO_3$ at room temperature show ferroelectric behaviour along with ME coupling. The linear ME coupling coefficient $(\frac{\alpha}{d})$ obtained is ~ 0.022 mV cm^{-1} kOe^{-1}. Thus, ambient temperature ferromagnetism, ferroelectric behaviour and magneto-electric coupling are demonstrated in $Bi_{0.85}Gd_{0.05}La_{0.1}FeO_3$ compound, attesting its potential for device applications.

Chapter 8

Summary, Conclusions and Future Work

A summary of our investigations on polycrystalline $GdFeO_3$, Ga substituted $YMnO_3$ and ‘Gd,La’ co-substituted $BiFeO_3$ is provided below, along with our new findings. Also, scope for future work on the samples studied in this dissertation is mentioned at the end of the chapter.

8.1 Summary

- **Chapter 3:** Our DFT based GGA-PBE calculations suggest that canted G-AFM spin configuration of $GdFeO_3$ possesses lowest energy compared to other spin configurations. The spin structures of Fe^{3+} and Gd^{3+} in canted G-AFM configuration are (G_x, A_y, F_z) and G_x respectively. Canted Fe^{3+} moments lead to a small ferromagnetic component of 0.026 μ_B per Fe^{3+} ion, aligned along negative ‘c’ axis. Our computational results are in corroboration with experimental observations discussed in chapter 4.
- **Chapter 4:** The phase purity of polycrystalline $GdFeO_3$ synthesized using solid-state route has been confirmed by Rietveld refinement of room temperature XRD pattern. Temperature dependence of magnetization (M-T) measured under a dc field of 100 Oe reveals an AFM transition below ~ 2.8 K associated with Gd^{3+} moments, along with a bifurcation between ZFC and FC magnetization below ~ 200 K. The bifurcation could be associated with the interaction between Gd^{3+} and Fe^{3+} sub-lattices. ZFC and FC magnetization measured under a high field of 50 kOe follows Curie-Weiss (CW) law. The FC magnetization fitted to a modified CW law results in μ_{eff} ~ 7.96 μ_B which corresponds to Gd^{3+}spin moment (S = 7/2) and a weak ferromagnetic component (χ_0) from canted Fe^{3+} moments that saturates under a high field and becomes temperature independent. The said ferromagnetic component

corresponds to ~ 0.022 μ_B/ion, which corroborates well with the canted moment of 0.026 μ_B per Fe^{3+} ion estimated by computational studies (chapter 3). Further, the appearance of hysteresis in high field region of isothermal magnetization (M-H) measurements below Gd^{3+} transition temperature (~ 2.8 K) evidences a spin flop type metamagnetic transition of Gd^{3+} moments to ferromagnetic state from antiferromagnetic state (chapter 4). In addition, the presence of a loop in M-H measured at temperatures slightly above 2.8 K is ascribed to the short-range interaction between Gd^{3+} moments although long range interaction had vanished.

- **Chapter 5:** Rietveld-refinement of powder XRD patterns of polycrystalline $YMn_{1-x}Ga_xO_3$ (x 0.0, 0.03 and 0.06) confirms the formation of single phase hexagonal structures with 'P63cm' space group symmetry in all the compounds. Deconvolution of XPS spectra corresponding to Mn in unsubstituted $YMnO_3$ and $YMn_{0.97}Ga_{0.03}O_3$ compounds shows mixed valence states of Mn^{2+} and Mn^{3+} in the proportions 75 : 25 and 54 : 46 respectively. However, the spectrum for $YMn_{0.94}Ga_{0.06}O_3$ compound could be fitted well to Mn^{3+} state. These observations are supported by magnetization measurements. M-T measurement on $YMnO_3$ shows an antiferromagnetic transition at ~ 75 K associated with ordering of Mn^{3+} moments. This transition temperature gets lowered to ~ 65 K for $YMn_{0.94}Ga_{0.06}O_3$ compound. The μ_{eff} obtained is 5.53 μ_B for $YMnO_3$ which is close to the moment calculated considering the ionic proportion obtained from XPS analysis. Also, a similar analysis results in a satisfactory agreement for $YMn_{0.97}Ga_{0.03}O_3$ compound. Finally, μ_{eff} obtained for $YMn_{0.94}Ga_{0.06}O_3$ compound is 4.78 μ_B, which is close to the moment associated with Mn^{3+} ion, indicating that Mn valency in $YMn_{0.94}Ga_{0.06}O_3$ stabilizes at 3+. Magnetization studies indicate the presence of magnetic frustration in all the compounds. However, the frustration decreases with Ga substitution.

- **Chapter 6:** In this chapter, we have studied the effect of annealing atmosphere on magnetic frustration in $YMn_{66.67}Ga_{33.33}O_{3+\delta}$ (YMGO) prepared under different atmospheres. It has been observed that the samples prepared in high purity argon and vacuum exhibit an anti-ferromagnetic transition at ~ 35 K. However, such a transition was not observed in samples prepared in high purity oxygen or air. Modified CW fitting of M-T data results in μ_{eff} ~ 4.88 $\mu_B$for YMGO_Ar and YMGO_vacu which corresponds to spin moment associated with Mn^{3+} ion. The μ_{eff} obtained for YMGO_O_2 is ~ 4.02 μ_B, indicating that Mn ions perhaps exist in mixed valence state of Mn^{3+} and Mn^{4+}. Analysis of M-T data reveals the presence of magnetic frustration in YMGO_Ar and YMGO_vacu. However, a purely paramagnetic behavior is observed for YMGO_O_2 compound, indicating a significant impact of annealing atmosphere on magnetic frustration in YMGO system.
- **Chapter 7:** In this chapter, we have discussed the results of our magnetic, ferroelectric and magneto-electric studies on polycrystalline $BiFeO_3$ and $Bi_{0.9-x}Gd_xLa_{0.1}FeO_3$ (x = 0.00 and 0.05), synthesized using solid-state reaction method. Rietveld analysis of XRD patterns for all the compounds confirms the formation of single phases in Rhombohedral structure with 'R3c' space group. Field dependent magnetization measurements carried out on $Bi_{0.85}Gd_{0.05}La_{0.1}FeO_3$ at room temperature show a ferromagnetic behavior along with an underlying anti-ferromagnetic behavior. Also, a shift of hysteresis loop towards negative field axis is observed, indicating an exchange bias effect at room temperature. These observations could be explained in terms of exchange interactions amongst two separate magnetic entities, namely, ferromagnetic interaction within Fe moments arrested around Gd atoms and anti-ferromagnetic component due to the rest of Fe moments. Leakage current density measurements show an increase in insulating properties and a good ferroelectric

behavior in $Bi_{0.85}Gd_{0.05}La_{0.1}FeO_3$ compound. A non-linear dependency of magnetic and electric vectors is obtained from magneto-electric measurements.

8.2 Contribution of the thesis

The thesis provides a significant contribution, as detailed below, towards the understanding of various properties in the compounds studied herein.

- A systematic computational study of magnetic properties of $GdFeO_3$ reveals that the magnetic structures associated with Fe^{3+} and Gd^{3+} moments are (G_x, A_y, F_z) and G_x respectively, an inference supported by our experimental studies. Also, detailed isothermal magnetization studies indicated a possible metamagnetic transition of Gd^{3+} moments to ferromagnetic state on application of magnetic field. These observations are hitherto unreported (chapter 3 & 4).
- Detailed analysis of XPS and magnetization data indicates that Mn ions are in mixed valence state of Mn^{2+} and Mn^{3+} in unsubstituted $YMnO_3$. However, the Mn valency stabilizes in 3+ state upon Ga substitution in $YMn_{0.94}Ga_{0.06}O_3$. The magnetic frustration decreases with increasing Ga substitution. A correlation between XPS and magnetization data has been established which is hitherto unreported (chapter 5).
- Detailed structural and magnetization studies on polycrystalline $YMn_{66.67}Ga_{33.33}O_{3+\delta}$ synthesized under different atmospheres reveals that the magnetic frustration in these compounds strongly depends on oxygen stoichiometry (chapter 6).
- Magnetization versus magnetic field and polarization versus electric field measurements on polycrystalline $Bi_{0.85}Gd_{0.05}La_{0.1}FeO_3$ show the appearance of ferromagnetism and ferroelectricity respectively, at room temperature. Besides, an exchange bias effect and non-linear magneto-electric coupling at room

temperature are observed in this compound. These results should lead to practical applications.

8.3 Scope for future work

- Extensive studies have been reported in literature on $GdFeO_3$. However, there is no neutron diffraction study on this compound due to a large neutron absorption cross section of Gd (especially ^{157}Gd). One should try preparing this compound with other isotopes of Gd (preferably ^{160}Gd) with small neutron absorption cross section to investigate the ground state spin structure of Gd and Fe sub-lattices.
- Our studies on polycrystalline $YMn_{66.67}Ga_{33.33}O_{3+\delta}$ compounds prepared under different atmospheres showed that magnetic frustration in this system depends on its oxygen content. So, it is desirable to carry out a detailed study to find out the exact origin of magnetic frustration.
- It is found that $Bi_{0.85}Gd_{0.05}La_{0.1}FeO_3$ compound is a potential candidate for technological applications due to simultaneous existence of ferroelectricity and ferromagnetism along with magneto-electric coupling at room temperature. It is therefore desirable to study multiferroic properties of $Bi_{0.85}Gd_{0.05}La_{0.1}FeO_3$ thin-film form from device potential perspective.
- Ferromagnetic materials (such as Fe, Co, Gd etc.) are characterized by a strong positive exchange interaction between neighboring spins. Using this strong interaction effect, one can control the magnetic properties of any other compound placed close to ferromagnetic materials. So, one should study ferromagnetic/multiferroic thin-film hetero-structures to achieve colossal magneto-electric coupling at room temperature for device applications.

Chapter 8

Summary, Conclusions and Future Work

A summary of our investigations on polycrystalline $GdFeO_3$, Ga substituted $YMnO_3$ and 'Gd,La' co-substituted $BiFeO_3$ is provided below, along with our new findings. Also, scope for future work on the samples studied in this dissertation is mentioned at the end of the chapter.

8.1 Summary

- **Chapter 3:** Our DFT based GGA-PBE calculations suggest that canted G-AFM spin configuration of $GdFeO_3$ possesses lowest energy compared to other spin configurations. The spin structures of Fe^{3+} and Gd^{3+} in canted G-AFM configuration are (G_x, A_y, F_z) and G_x respectively. Canted Fe^{3+} moments lead to a small ferromagnetic component of 0.026 μ_B per Fe^{3+} ion, aligned along negative 'c' axis. Our computational results are in corroboration with experimental observations discussed in chapter 4.
- **Chapter 4:** The phase purity of polycrystalline $GdFeO_3$ synthesized using solid-state route has been confirmed by Rietveld refinement of room temperature XRD pattern. Temperature dependence of magnetization (M-T) measured under a dc field of 100 Oe reveals an AFM transition below ~ 2.8 K associated with Gd^{3+} moments, along with a bifurcation between ZFC and FC magnetization below ~ 200 K. The bifurcation could be associated with the interaction between Gd^{3+} and Fe^{3+} sub-lattices. ZFC and FC magnetization measured under a high field of 50 kOe follows Curie-Weiss (CW) law. The FC magnetization fitted to a modified CW law results in μ_{eff} ~ 7.96 μ_B which corresponds to Gd^{3+}spin moment (S = 7/2) and a weak ferromagnetic component (χ_0) from canted Fe^{3+} moments that saturates under a high field and becomes temperature independent. The said ferromagnetic component

corresponds to ~ 0.022 μ_B/ion, which corroborates well with the canted moment of 0.026 μ_B per Fe^{3+} ion estimated by computational studies (chapter 3). Further, the appearance of hysteresis in high field region of isothermal magnetization (M-H) measurements below Gd^{3+} transition temperature (~ 2.8 K) evidences a spin flop type metamagnetic transition of Gd^{3+} moments to ferromagnetic state from antiferromagnetic state (chapter 4). In addition, the presence of a loop in M-H measured at temperatures slightly above 2.8 K is ascribed to the short-range interaction between Gd^{3+} moments although long range interaction had vanished.

- **Chapter 5:** Rietveld-refinement of powder XRD patterns of polycrystalline $YMn_{1-x}Ga_xO_3$ (x 0.0, 0.03 and 0.06) confirms the formation of single phase hexagonal structures with 'P63cm' space group symmetry in all the compounds. Deconvolution of XPS spectra corresponding to Mn in unsubstituted $YMnO_3$ and $YMn_{0.97}Ga_{0.03}O_3$ compounds shows mixed valence states of Mn^{2+} and Mn^{3+} in the proportions 75 : 25 and 54 : 46 respectively. However, the spectrum for $YMn_{0.94}Ga_{0.06}O_3$ compound could be fitted well to Mn^{3+} state. These observations are supported by magnetization measurements. M-T measurement on $YMnO_3$ shows an antiferromagnetic transition at ~ 75 K associated with ordering of Mn^{3+} moments. This transition temperature gets lowered to ~ 65 K for $YMn_{0.94}Ga_{0.06}O_3$ compound. The μ_{eff} obtained is 5.53 μ_B for $YMnO_3$ which is close to the moment calculated considering the ionic proportion obtained from XPS analysis. Also, a similar analysis results in a satisfactory agreement for $YMn_{0.97}Ga_{0.03}O_3$ compound. Finally, μ_{eff} obtained for $YMn_{0.94}Ga_{0.06}O_3$ compound is 4.78 μ_B, which is close to the moment associated with Mn^{3+} ion, indicating that Mn valency in $YMn_{0.94}Ga_{0.06}O_3$ stabilizes at 3+. Magnetization studies indicate the presence of magnetic frustration in all the compounds. However, the frustration decreases with Ga substitution.

- **Chapter 6:** In this chapter, we have studied the effect of annealing atmosphere on magnetic frustration in $YMn_{66.67}Ga_{33.33}O_{3+\delta}$ (YMGO) prepared under different atmospheres. It has been observed that the samples prepared in high purity argon and vacuum exhibit an anti-ferromagnetic transition at ~ 35 K. However, such a transition was not observed in samples prepared in high purity oxygen or air. Modified CW fitting of M-T data results in μ_{eff} ~ 4.88 $\mu_B$for YMGO_Ar and YMGO_vacu which corresponds to spin moment associated with Mn^{3+} ion. The μ_{eff} obtained for YMGO_O_2 is ~ 4.02 μ_B, indicating that Mn ions perhaps exist in mixed valence state of Mn^{3+} and Mn^{4+}. Analysis of M-T data reveals the presence of magnetic frustration in YMGO_Ar and YMGO_vacu. However, a purely paramagnetic behavior is observed for YMGO_O_2 compound, indicating a significant impact of annealing atmosphere on magnetic frustration in YMGO system.
- **Chapter 7:** In this chapter, we have discussed the results of our magnetic, ferroelectric and magneto-electric studies on polycrystalline $BiFeO_3$ and $Bi_{0.9-x}Gd_xLa_{0.1}FeO_3$ (x = 0.00 and 0.05), synthesized using solid-state reaction method. Rietveld analysis of XRD patterns for all the compounds confirms the formation of single phases in Rhombohedral structure with ‘R3c’ space group. Field dependent magnetization measurements carried out on $Bi_{0.85}Gd_{0.05}La_{0.1}FeO_3$ at room temperature show a ferromagnetic behavior along with an underlying anti-ferromagnetic behavior. Also, a shift of hysteresis loop towards negative field axis is observed, indicating an exchange bias effect at room temperature. These observations could be explained in terms of exchange interactions amongst two separate magnetic entities, namely, ferromagnetic interaction within Fe moments arrested around Gd atoms and anti-ferromagnetic component due to the rest of Fe moments. Leakage current density measurements show an increase in insulating properties and a good ferroelectric

behavior in $Bi_{0.85}Gd_{0.05}La_{0.1}FeO_3$ compound. A non-linear dependency of magnetic and electric vectors is obtained from magneto-electric measurements.

8.2 Contribution of the thesis

The thesis provides a significant contribution, as detailed below, towards the understanding of various properties in the compounds studied herein.

- A systematic computational study of magnetic properties of $GdFeO_3$ reveals that the magnetic structures associated with Fe^{3+} and Gd^{3+} moments are (G_x, A_y, F_z) and G_x respectively, an inference supported by our experimental studies. Also, detailed isothermal magnetization studies indicated a possible metamagnetic transition of Gd^{3+} moments to ferromagnetic state on application of magnetic field. These observations are hitherto unreported (chapter 3 & 4).
- Detailed analysis of XPS and magnetization data indicates that Mn ions are in mixed valence state of Mn^{2+} and Mn^{3+} in unsubstituted $YMnO_3$. However, the Mn valency stabilizes in 3+ state upon Ga substitution in $YMn_{0.94}Ga_{0.06}O_3$. The magnetic frustration decreases with increasing Ga substitution. A correlation between XPS and magnetization data has been established which is hitherto unreported (chapter 5).
- Detailed structural and magnetization studies on polycrystalline $YMn_{66.67}Ga_{33.33}O_{3+\delta}$ synthesized under different atmospheres reveals that the magnetic frustration in these compounds strongly depends on oxygen stoichiometry (chapter 6).
- Magnetization versus magnetic field and polarization versus electric field measurements on polycrystalline $Bi_{0.85}Gd_{0.05}La_{0.1}FeO_3$ show the appearance of ferromagnetism and ferroelectricity respectively, at room temperature. Besides, an exchange bias effect and non-linear magneto-electric coupling at room

temperature are observed in this compound. These results should lead to practical applications.

8.3 Scope for future work

- Extensive studies have been reported in literature on $GdFeO_3$. However, there is no neutron diffraction study on this compound due to a large neutron absorption cross section of Gd (especially ^{157}Gd). One should try preparing this compound with other isotopes of Gd (preferably ^{160}Gd) with small neutron absorption cross section to investigate the ground state spin structure of Gd and Fe sub-lattices.
- Our studies on polycrystalline $YMn_{66.67}Ga_{33.33}O_{3+\delta}$ compounds prepared under different atmospheres showed that magnetic frustration in this system depends on its oxygen content. So, it is desirable to carry out a detailed study to find out the exact origin of magnetic frustration.
- It is found that $Bi_{0.85}Gd_{0.05}La_{0.1}FeO_3$ compound is a potential candidate for technological applications due to simultaneous existence of ferroelectricity and ferromagnetism along with magneto-electric coupling at room temperature. It is therefore desirable to study multiferroic properties of $Bi_{0.85}Gd_{0.05}La_{0.1}FeO_3$ thin-film form from device potential perspective.
- Ferromagnetic materials (such as Fe, Co, Gd etc.) are characterized by a strong positive exchange interaction between neighboring spins. Using this strong interaction effect, one can control the magnetic properties of any other compound placed close to ferromagnetic materials. So, one should study ferromagnetic/multiferroic thin-film hetero-structures to achieve colossal magneto-electric coupling at room temperature for device applications.

❖ Summary

A summary of our investigations on polycrystalline $GdFeO_3$, Ga substituted $YMnO_3$ and 'Gd,La' co-substituted $BiFeO_3$ is provided below, along with our new findings.

- **Chapter 3:** Our DFT based GGA-PBE calculations suggest that canted G-AFM spin configuration of $GdFeO_3$ possesses lowest energy compared to other spin configurations. The spin structures of Fe^{3+} and Gd^{3+} in canted G-AFM configuration are (G_x, A_y, F_z) and G_x respectively. Canted Fe^{3+} moments lead to a small ferromagnetic component of 0.026 μ_B per Fe^{3+} ion, aligned along negative 'c' axis. Our computational results are in corroboration with experimental observations discussed in chapter 4.
- **Chapter 4:** The phase purity of polycrystalline $GdFeO_3$ synthesized using solid-state route has been confirmed by Rietveld refinement of room temperature XRD pattern. Temperature dependence of magnetization (M-T) measured under a dc field of 100 Oe reveals an AFM transition below ~ 2.8 K associated with Gd^{3+} moments, along with a bifurcation between ZFC and FC magnetization below ~ 200 K. The bifurcation could be associated with the interaction between Gd^{3+} and Fe^{3+} sub-lattices. ZFC and FC magnetization measured under a high field of 50 kOe follows Curie-Weiss (CW) law. The FC magnetization fitted to a modified CW law results in μ_{eff} ~ 7.96 μ_B which corresponds to Gd^{3+}spin moment (S = 7/2) and a weak ferromagnetic component (χ_0) from canted Fe^{3+} moments that saturates under a high field and becomes temperature independent. The said ferromagnetic component corresponds to ~ 0.022 μ_B/ion, which corroborates well with the canted moment of 0.026 μ_B per Fe^{3+} ion estimated by computational studies (chapter 3). Further, the appearance of hysteresis in

highfield region of isothermal magnetization (M-H) measurements below Gd^{3+} transition temperature (~ 2.8 K) evidences a spin flop type metamagnetic transition of Gd^{3+} moments to ferromagnetic state from antiferromagnetic state (chapter 4). In addition, the presence of a loop in M-H measured at temperatures slightly above 2.8 K is ascribed to the short-range interaction between Gd^{3+} moments although long range interaction had vanished.

- **Chapter 5:** Rietveld-refinement of powder XRD patterns of polycrystalline $YMn_{1-x}Ga_xO_3$ (x 0.0, 0.03 and 0.06) confirms the formation of single phase hexagonal structures with 'P63cm' space group symmetry in all the compounds. Deconvolution of XPS spectra corresponding to Mn in unsubstituted $YMnO_3$ and $YMn_{0.97}Ga_{0.03}O_3$ compounds shows mixed valence states of Mn^{2+} and Mn^{3+} in the proportions 75 : 25 and 54 : 46 respectively. However, the spectrum for $YMn_{0.94}Ga_{0.06}O_3$ compound could be fitted well to Mn^{3+} state. These observations are supported by magnetization measurements. M-T measurement on $YMnO_3$ shows an antiferromagnetic transition at ~ 75 K associated with ordering of Mn^{3+} moments. This transition temperature gets lowered to ~ 65 K for $YMn_{0.94}Ga_{0.06}O_3$ compound. The μ_{eff} obtained is 5.53 μ_B for $YMnO_3$ which is close to the moment calculated considering the ionic proportion obtained from XPS analysis. Also, a similar analysis results in a satisfactory agreement for $YMn_{0.97}Ga_{0.03}O_3$ compound. Finally, μ_{eff} obtained for $YMn_{0.94}Ga_{0.06}O_3$ compound is 4.78 μ_B, which is close to the moment associated with Mn^{3+} ion, indicating that Mn valency in $YMn_{0.94}Ga_{0.06}O_3$ stabilizes at 3+. Magnetization studies indicate the presence of magnetic frustration in all the compounds. However, the frustration decreases with Ga substitution.

- **Chapter 6:** In this chapter, we have studied the effect of annealing atmosphere on magnetic frustration in $YMn_{66.67}Ga_{33.33}O_{3+\delta}$ (YMGO) prepared under different atmospheres. It has been observed that the samples prepared in high purity argon and vacuum exhibit an anti-ferromagnetic transition at ~ 35 K. However, such a transition was not observed in samples prepared in high purity oxygen or air. Modified CW fitting of M-T data results in μ_{eff} ~ 4.88 μ_B for YMGO_Ar and YMGO_vacu which correspond to spin moment associated with Mn^{3+} ion. The μ_{eff} obtained for $YMGO\_O_2$ is ~ 4.02 μ_B, indicating that Mn ions perhaps exist in mixed valence state of Mn^{3+} and Mn^{4+}. Analysis of M-T data reveals the presence of magnetic frustration in YMGO_Ar and YMGO_vacu. However, a purely paramagnetic behavior is observed for $YMGO\_O_2$ compound, indicating a significant impact of annealing atmosphere on magnetic frustration in YMGO system.
- **Chapter 7:** In this chapter, we have discussed the results of our magnetic, ferroelectric and magneto-electric studies on polycrystalline $BiFeO_3$ and $Bi_{0.9-x}Gd_xLa_{0.1}FeO_3$ (x = 0.00 and 0.05), synthesized using solid-state reaction method. Rietveld analysis of XRD patterns for all the compounds confirms the formation of single phases in Rhombohedral structure with 'R3c' space group. Field dependent magnetization measurements carried out on $Bi_{0.85}Gd_{0.05}La_{0.1}FeO_3$ at room temperature show a ferromagnetic behavior along with an underlying anti-ferromagnetic behavior. Also, a shift of hysteresis loop towards negative field axis is observed, indicating an exchange bias effect at room temperature. These observations could be explained in terms of exchange interactions amongst two separate magnetic entities, namely, ferromagnetic interaction within Fe moments arrested around Gd atoms and anti-ferromagnetic component due to the rest of Fe moments.

Leakage current density measurements show an increase in insulating properties and a good ferroelectric behavior in $Bi_{0.85}Gd_{0.05}La_{0.1}FeO_3$ compound. A non-linear dependency of magnetic and electric vectors is obtained from magneto-electric measurements.

❖ Contribution of the thesis

The thesis provides a significant contribution, as detailed below, towards the understanding of various properties in the compounds studied herein.

- A systematic computational study of magnetic properties of $GdFeO_3$ reveals that the magnetic structures associated with Fe^{3+} and Gd^{3+} moments are (G_x, A_y, F_z) and G_x respectively, an inference supported by our experimental studies. Also, detailed isothermal magnetization studies indicated a possible metamagnetic transition of Gd^{3+} moments to ferromagnetic state on application of magnetic field. These observations are hitherto unreported (chapter 3 & 4).
- Detailed analysis of XPS and magnetization data indicates that Mn ions are in mixed valence state of Mn^{2+} and Mn^{3+} in unsubstituted $YMnO_3$. However, the Mn valency stabilizes in 3+ state upon Ga substitution in $YMn_{0.94}Ga_{0.06}O_3$. The magnetic frustration decreases with increasing Ga substitution. A correlation between XPS and magnetization data has been established which is hitherto unreported (chapter 5).
- Detailed structural and magnetization studies on polycrystalline $YMn_{66.67}Ga_{33.33}O_{3+\delta}$ synthesized under different atmospheres reveals that the magnetic frustration in these compounds strongly depends on oxygen stoichiometry (chapter 6).
- Magnetization versus magnetic field and polarization versus electric field measurements on polycrystalline $Bi_{0.85}Gd_{0.05}La_{0.1}FeO_3$ show the appearance of ferromagnetism and ferroelectricity respectively, at room temperature. Besides, an

exchange bias effect and non-linear magneto-electric coupling at room temperature are observed in this compound. These results should lead to practical applications.

List of Publications arising from the thesis

Journal

---

1. “Valence fluctuation and magnetic frustration in Ga substituted $YMnO_3$”, **Pralay Paul**, A.K. Rajarajan, A.K. Debnath, Rekha Rao and T.V. Chandrasekhar Rao, J. Magn. Magn. Mater. 503 (2020) 166617 (1 – 6).

2. "Ground State Spin Structure of $GdFeO_3$: A Computational and Experimental study", **Pralay Paul**, P.S. Ghosh, A.K. Rajarajan, P. D. Babu and T.V. Chandrasekhar Rao, J. Magn. Magn. Mater. 518 (2021) 167407 (1 - 7).

Conferences

---

1. “Structural and magnetic properties of $YMn_{1-x}Ga_xO_3$”, **Pralay Paul**, A.K. Rajarajan, C. L. Prajapat, A.K. Debnath and T.V. Chandrasekhar Rao, AIP Conference Proceedings 2265 (2020) 030505 (1 - 4).

2. “Low temperature magnetic properties of $GdFeO_3$”, **Pralay Paul**, C. L. Prajapat, A. K. Rajarajan, and T. V. Chandrasekhar Rao, AIP Conference Proceedings, 1942 (2018) 130029 (1 - 3).

3. “Theoretical and experimental study of multiferroic $BiFeO_3$”, **Pralay Paul**, Tuhin Kumar Maji, Krishna Kanhaiya Tiwari, Balaji Mandal, A. K. Rajarajan, Ranu Bhatt, Debjani Karmakar, and T. V. C. Rao, AIP Conference Proceedings, 1832 (2017) 130058 (1 - 3).

Others

---

1. “Magnetic and transport properties of inverse Heusler compound Cr_2CoAl” Amrita Datta, Mantu Modak, **Pralay Paul**, Manju Mishra Patidar, T. V. Chandrasekhar Rao, V Ganesan, Sangam Banerjee, J. Magn. Magn. Mater. 521 (2021) 167522 (1 - 8).

Communicated

1. "Plausible Multiferroic and Magneto-electric Behaviour of Polycrystalline $Bi_{0.85}Gd_{0.05}La_{0.1}FeO_3$ at Room Temperature", **Pralay Paul**, A.K. Rajarajan, S. Kuila, A.K. Debnath, B.P Mandal and T.V. Chandrasekhar Rao. (under review).

1. “Metamagnetic Transition in polycrystalline $GdFeO_3$”, **Pralay Paul**, A. K. Rajarajan, P. D. Babau and T. V. Chandrasekhar Rao. (under review).

Presentation in national and international conferences

1. **Pralay Paul**, et al., Theoretical and Experimental study of Multiferroic BiFeO3, 61st DAE – Solid State Physics Symposium, 26th – 30th December 2016, KIIT University, Bhubaneswar, Odisha, India.

2. **Pralay Paul,** et al., Low Temperature Magnetic Properties of GdFeO3, 62ndDAE – Solid State Physics Symposium, 26th – 30th December 2017, DAE Convention Centre, Anushaktinagar, Mumbai, India.

3. **Pralay Paul,** et al., Plausible Room Temperature Ferromagnetism in Bi0.9-xGdxLa0.1FeO3, International Conference on Magnetic Materials and Applications (ICMAGMA - 2018), 9th – 13th December, 2018, NISER-Bhubaneswar, Jatni, Odisha, India.

4. **Pralay Paul,** et al., On Magnetic Transition in GdFeO3, Materials and Technologies for Energy Conversion and Storage (M-TECS - 2018), 26th Sept. – 29th Sept. 2018, Bhabha Atomic Research Centre, Mumbai, India.

5. Pralay Paul, et al., Effect of Ga Doping on Magnetic Properties of h-YMnO3, 63rd DAE – Solid State Physics Symposium, 18th – 22nd December 2018, Guru Jambheshwar University of Science and Technology (GJUS&T), Hisar, Haryana, India.

6. **Pralay Paul,** et al., Structural and Magnetic Properties of YMn1-x GaxO3, 64th DAE – Solid State Physics Symposium, 18th – 22nd December 2019, Indian Institute of Technology Jodhpur, Jodhpur, Rajasthan, India.

7. **Pralay Paul,** et al., A study on valence fluctuation in Ga substituted YMnO3, The International Magnetics Conference (INTERMAG 2020), 4th – 8th May, 2020, Montreal, Canada (Paper was accepted for oral presentation but conference got cancelled on account of COVID-19).

Pralay Paul
(PRALAY PAUL)
Name & Signature of the student

Thesis Highlights

Name of the Student: PRALAY PAUL

Name of the CI/OCC: BARC, Mumbai **Enrolment No.:** PHYS01201604026

Thesis Title: Structural and Magnetization Studies on Selected Multiferroic Oxides

Discipline: Physical Sciences **Sub-Area of Discipline:** Multiferroic Materials

Date of viva voce: 15/05/2021

This thesis makes a significant contribution to the understanding of various properties of multiferroic oxides investigated, as detailed below. Apart from providing an additional insight into the electronic interactions, the findings of this thesis have implications for practical use of some of the materials.

A systematic computational study of magnetic properties of $GdFeO_3$ reveals that the spin configurations associated with Fe^{3+} and Gd^{3+} moments are (G_x, A_y, F_z) and G_x respectively, an inference supported by our experimental studies. Also, detailed isothermal magnetization studies indicated a possible metamagnetic transition of Gd^{3+} moments to ferromagnetic state on application of magnetic field. These observations are hitherto unreported.

Detailed analysis of XPS and magnetization data of $YMnO_3$ indicates that Mn ions exist in a mixed-valence state of Mn^{2+} and Mn^{3+}. However, the Mn valency stabilizes in 3+ state upon Ga substitution in $YMn_{0.94}Ga_{0.06}O_3$. The magnetic frustration decreases with increasing Ga substitution. A correlation between XPS and magnetization data has been established which is hitherto unreported. Detailed structural and magnetization studies on polycrystalline $YMn_{66.67}Ga_{33.33}O_{3+\delta}$ synthesized under different atmospheres reveal that the magnetic frustration in these compounds strongly depends on oxygen stoichiometry (chapter 6).

Magnetization versus magnetic field and polarization versus electric field measurements on polycrystalline $Bi_{0.85}Gd_{0.05}La_{0.1}FeO_3$ show the appearance of ferromagnetism and ferroelectricity, respectively, at room temperature. Besides, an exchange bias effect and non-linear magneto-electric coupling at room temperature is observed in this compound. These results should lead to practical applications.

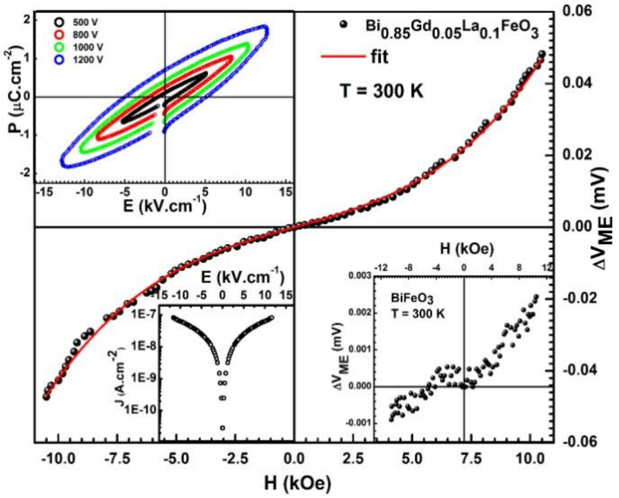

Figure: Magneto-electric voltage (V_{ME}) vs dc magnetic field (H) measurement on polycrystalline $Bi_{0.85}Gd_{0.05}La_{0.1}FeO_3$ at room temperature. Right-lower inset shows the same for $BiFeO_3$.Upper and lower left insets show Polarization hysteresis (P - E) loops and the current density (J) vs electric field (E) of polycrystalline $Bi_{0.85}Gd_{0.05}La_{0.1}FeO_3$ measured at room temperature.